Journal of Materials Chemistry C

ROYAL SOCIETY OF CHEMISTRY

REVIEW

View Article Online
View Journal | View Issue

Cite this: J. Mater. Chem. C, 2024, 12, 2317

Bifacial dye-sensitized solar cells for indoor and outdoor renewable energy-based application

Jessica Barichello, *[ab] Paolo Mariani,[b] Luigi Vesce, [b] Donatella Spadaro,[a] Ilaria Citro,[a] Fabio Matteocci, [b] Antonino Bartolotta,[a] Aldo Di Carlo [bc] and Giuseppe Calogero *[a]

Received 6th September 2023,
Accepted 20th December 2023

DOI: 10.1039/d3tc03220e

rsc.li/materials-c

Bifacial solar cells (BFSCs) offer a way to boost electrical power generation for each unit area compared to traditional monofacial cells without a significant increase in production costs. These cells are designed to absorb sunlight from both front and rear sides, making them more efficient in converting light into electricity while exploiting the reflected solar radiation. The third-generation PV solar cells are widely known for the flexibility and the colour tunability allowing them to be designed as BFSCs. This article focuses on semi-transparent bifacial dye sensitized solar cells (BFDSCs), which stand out for their low production cost, for the possibility of being environmentally friendly and for the excellent conversion efficiency even in diffused light conditions, balancing both efficiency and transparency for a variety of applications. Their semi-transparent nature and the adaptability to different sunlight angles make BFDSCs ideal for both indoor and outdoor environments. This review highlights the newest breakthroughs in DSSC and provides an overview of the latest research on innovative electrodes, electrolytes, and dyes. Moreover, the review delves into current and potential uses of BFDSCs in areas such as agriculture, building integration, and smart devices.

1. Introduction

Over the past few decades, the rising demand for energy, coupled with the diminishing fossil resources and the imperative to reduce annual CO_2 emissions, has driven a shift towards renewable and eco-friendly energy sources. Solar energy stands out as a universally accessible, clean, and cost-effective resource for all of humanity. Using non-fossil fuel sources, such as solar energy, provides an economically viable solution to combat climate change. The sun delivers approximately 13.6 TW of carbon-free energy to the Earth every hour, which exceeds the annual energy consumption of the entire human population, estimated at around 13 TW h.[1] Harvesting just a tiny fraction of this enormous energy amount could be sufficient to satisfy the entire global energy demand.[2] In this context, renewable solar photovoltaics (PV), as one model to convert solar energy directly into electricity, will play a key role in decarbonizing our energy production in the coming decades.

To address this challenge, PV technologies have experienced rapid growth: from 2005 to 2019, global PV production surged from approximately 4 TW h to ~681 TW h.[3] In 2019, around 11% of global primary energy (encompassing electricity, transport, and heating) came from renewable technologies.[4] Furthermore, the International Energy Agency (IEA) predicts that renewables account for almost 40% of global electricity output in 2027, making up for declining shares of coal, natural gas and nuclear.[5]

To date, silicon-based solar cells are still the dominant technology in the PV market with power conversion efficiencies (PCE) up to 26.6%.[6] Comparable results have been achieved by a second generation of single- and multi-junction thin films solar cells (*e.g.*, cadmium telluride (CdTe)), gallium arsenide (GaAs), cadmium telluride/cadmium selenide (CdTe/CdS), copper indium gallium selenide (CIGS, *etc.*),[7] although more expensive due to their manufacturing and material costs. In all instances, the PCE values of single junction solar cell technologies remain still below the 33%, according to the Shockley–Queisser limit,[8] and significant efforts have been made to approach this limit. In the quest to find cheap and eco-friendly solar energy conversion solutions, some interesting and unconventional approaches have been explored.

Novel materials synthesis, as well as efficient device architectures with minimal environmental impact, have been developed by numerous research groups. Among the various alternative approaches, dye-sensitized solar cells (DSSCs), due to their inexpensive/non-toxic starting materials, easy fabrication process,

[a] CNR-IPCF, Viale F. Stagno D'Alcontres 37, 98158 Messina, Italy. E-mail: jessica.barichello@uniroma2.it, giuseppe.calogero@cnr.it
[b] CHOSE—Centre for Hybrid and Organic Solar Energy, Department of Electronic Engineering, University of Rome "Tor Vergata", 00133 Roma, Italy
[c] ISM-CNR, Istituto di Struttura della Materia, Consiglio Nazionale delle Ricerche, Via del Fosso del Cavaliere 100, 00133, 8 Roma, Italy

and significant aesthetic value, have been identified as one of the most competitive PV technologies for indoor applications and the Internet of Things (IoT).[9]

Mimicking the fundamental pathways of natural photosynthesis (*i.e.*, light harvesting, charge separation and catalysis effects), by synergistically combining a molecular system with nanoparticles, DSSCs, belonging to the 3rd PV generation, offer a fresh perspective compared to inorganic p–n junction solar cells, stand out in terms of cheapness, light manipulation and long-term stability. Furthermore, in contrast to conventional solar cells (SCs), DSSCs maintain good PCE under different light conditions and, more interestingly, they can be designed to be flexible and colorless or with a colorful appearance. These attributes make them appealing for architectural integration in both residential and commercial buildings[10] (known as building-integrated photovoltaics: BIPV) and portable applications, showing great potential in the realm of IoT, encompassing smart homes, healthcare, transportation, and much more (see Fig. 1).

Additionally, beyond their capability to meet energy demands, a particular choice of dye enables the proper filtering of incident solar radiation, making DSSCs ideal for agrivoltaic applications. Agrivoltaics refers to the dual use of land for solar photovoltaic power generation and agriculture. This approach presents a promising solution to minimize the competition between PV power generation and agricultural activities. Agrivoltaics can assist farmers in lowering their energy expenses and carbon footprint while enhancing their energy independence.[11]

Since the first paper of Grätzel and co-workers,[12] the progress in the field of DSSCs has been accompanied by impressive advancement in the PCE, passing from ~7.12% up to ~14%,[13,14] surpassing amorphous silicon.[15,16] With common and commercial red and orange dyes, DSSCs have reached an average visible transmittance (AVT) of 20–30%,[17] while an outstanding AVT higher than 60%,[18] has been reported using a select dye system which absorbs in the UV and near-IR region. However, though significant breakthroughs have been obtained and years of thriving growth can be expected, the need to improve the cell's PCE beyond 20% is of critical importance for the scale-up industrial applications of this technology.

In view of this, with the goal of increasing the quantity of light harvesting, and hence the PCE value, several approaches like complementary dyes combination, either as a dye cocktail or arranged in multiple dye layers, the use of functionalized organic dye molecules in a rigid panchromatic structure,[19] as well as strategies to enhance the optical path of incident light, *via* porous back-scattering films or submicron particles of high refractive index, have been considered.[20,21] Strong interest has also been paid to the development of tandem-DSSCs (T-DSSCs) configuration,[22] an alternative option to increase the device

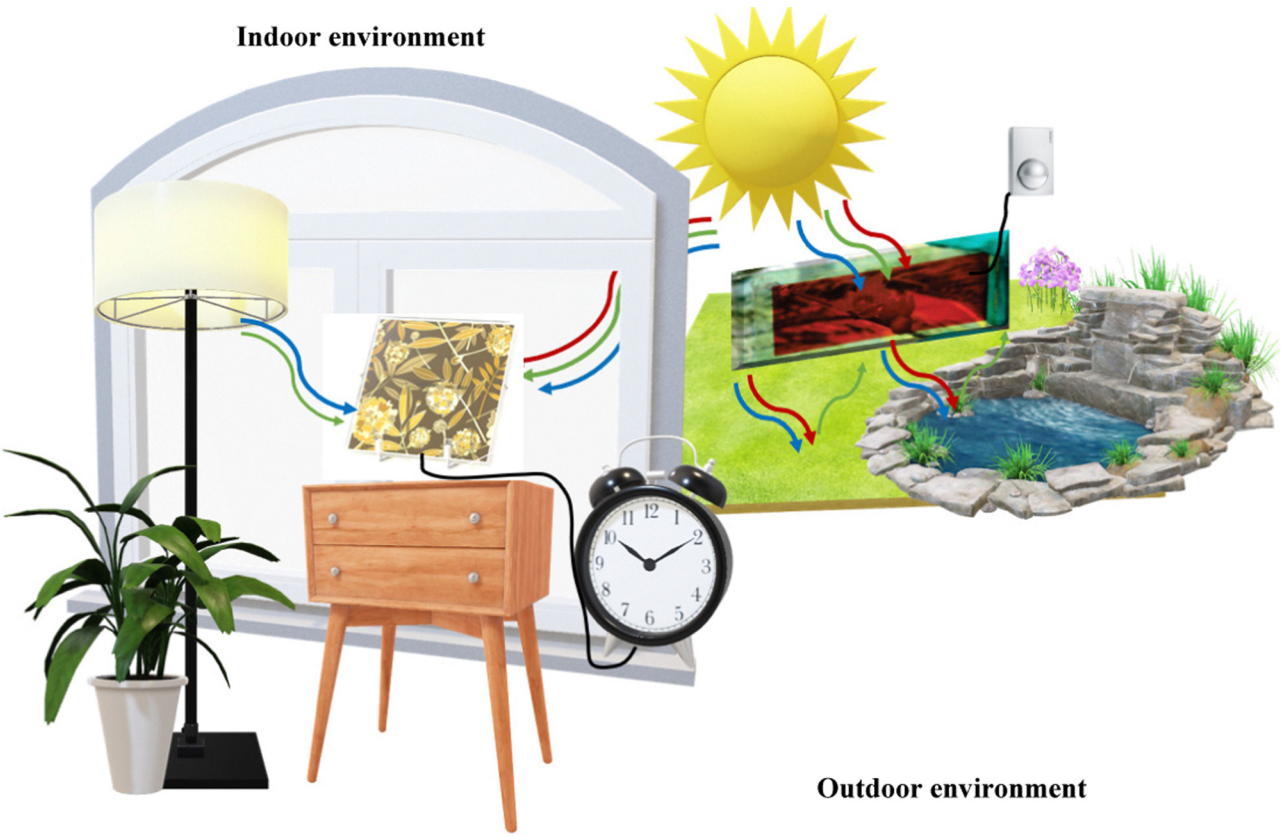

Fig. 1 A Hana Ankara lamp (modified image from https://www.sony.com/ja/pressroom/pict_data/images/sonota/200812_Hana-Akari_1.jpg) that powers a small electronic device absorbing light from the front and rear side in an indoor environment while a BFDSC (modified image from ref. 35) is powering a movment sensor in an outdoor environment.

efficiency beyond the thermodynamic limit of single junction. However, although great steps have been made, actual results are still not so satisfactory.[23] In the expectation to optimize solar cell architecture by using ecological criteria, the recent past has seen the rediscovered of bifacial solar cells (BFSCs) concept. A technology whose emergence can be traced back to a patent by Hiroshi in 1966[24] and following scientific reports by Luque, Cueva *et al.*[25,26] which, demonstrated significant higher electrical power production in BFSCs with respect to their monofacial counterpart. However, notwithstanding these premises, this technology was long ignored, except for some niche applications.[27] Bifacial technology gained new attention by academic and PV communities from 2009, especially when companies (like Yingli Solar, PVG Solutions Inc., Sanyo) began to commercialize bifacial modules based on crystalline silicon (c-Si) bifacial structures[28–30] (*e.g.*, PERC: passivated emitter rear contact; PERL: passivated emitter rear locally diffused; PERT: passivated emitter rear totally diffused; *etc.*[31]). Bifacial technology is perceived to be the most suitable choice for next-generation solar farms, thanks to its increased energy yield and low levelized cost of energy (LCOE[32]). The International Technology Roadmap for Photovoltaic (ITRPV) forecasts that bifacial solar cells are projected to hold over 80% of the global market share by 2032.[33]

In contrast to monofacial counterpart, which only collect photons reaching the device's front side, BFSCs capture photons from both the front and rear sides of the cell, allowing a better utilize of diffuse sky radiation and reflected light from surroundings (albedo), also offering the opportunity to lower the area-related costs. The additional rear side irradiance, as well as the device deployment (*e.g.*, orientation, tilt angle, *etc.*) and their synergic effects, generating a greater number of charge-carriers promotes a short-circuit current density enhancement and thus of overall PCE. The semi-transparent DSSC technology indeed is an ideal candidate to be applied as BFSC however, the nature and opaqueness of electrolytes and/or counter electrode (CE) can create dramatic losses in the cell performance during backside illumination owing to screening and reflecting effects. As a result, the number of photons which reach the dye molecules, for the front illumination is greater with respect to that of the back side which, implies a quite low response of rear efficiency in relation to the front efficiency (bifaciality factor, BFF[34]), both being subject to the same irradiance. The engineering of transparent and cost-effective materials and components to fulfil high transmittance requirements, has been a constant mission to open transformative opportunities in BFDSCs field.

In 2011, $BFDSC_S$ with transparent polyaniline CE and PCE values of 6.54% and 4.26% for front- and rear-side illumination, respectively, and BFF $\approx$ 65% were reported by Tai *et al.*[35] Duan *et al.*[36] reported optically transparent CEs based on binary-alloy metal selenides M–Se (M = Co, Ni, Cu, Fe, Ru). Irrespective to the M–Se alloy, their fabricated BFDSCs showed front and rear conversion efficiencies significantly higher than those obtained using CE based on the most widely utilized platinum. Miranda-Munoz and co-workers,[37] enhanced the PCE of BFDSCs by 25% and 33% in front- and rear-illumination, respectively, compared to an equivalent standard cell, by random dispersion of scattering particles in the nanostructured TiO_2 photoanode. By judicious choice of electrolyte, CE, and photoanode, Venkatesan *et al.*,[38] reported BFDSCs exhibiting PCE values as high as 20.65% and 17.31% under front-and rear-illumination, respectively, in indoor condition.

Currently, amorphous and crystalline silicon dominates the photovoltaic market. However, even in bifacial form, Si-based PV retains its intrinsic opacity properties, which make it unsuitable for BIPV or indoor applications.[39] In addition, unlike DSSC technology, silicon is very sensitive to the angle of incidence of light radiation.[40,41] Third-generation PV technologies, such as organic photovoltaic (OPV), DSSC, and perovskite solar cells (PSCs), in a bifacial configuration offer several advantages for flexible, lightweight, and semi-transparent applications.[27] Recent PSCs have reached record efficiencies of over 26%.[16] This technology can also achieve high light transmittance and coloured-semitransparency, making PSCs suitable for indoor and BIPV applications.[42] PSCs can also be fabricated in a bifacial configuration without the need for additional material, and they are not as sensitive to the angle of incidence of light as silicon solar cells. However, the main challenge to the commercialization of PSCs is their stability.[43] Perovskites are sensitive to moisture and light, which can degrade their performance over time. In OPV field, Burgués-Ceballos *et al.*[44] explore the optimal trade-off between average AVT and PCE for various semi-transparent PV applications. While some OPV cells can achieve PCE and AVT values exceeding 5% and 40%, respectively, suitable for applications like skylights, PV windows, and smart windows, OPV solar modules still lack a satisfactory balance between these parameters.[45] Despite the plethora of papers detailing with the advances made in DSSCs technological applications and designs, to our best knowledge, there are no published reviews focused on specific materials capable to emphasize/improve the bifacial feature in terms of PCE and transparency.[27,46,47] Here we present an update overview of current efforts in the advancement of this transitioning technology, highlighting the optical properties of each device component to reach the best compromise between BFF and overall PCE, also discussing the optimum indoor/outdoor conditions. Paragraph number 2 focus on the working system of the DSSC technology, the main figures of merit (FoM) in BFDSCs and the albedo's effect in order to facilitate the discussion and understanding of subsequent sections. The associated properties and issues correlated to the device's main components are given and critically discussed in Sections 3.1–3.5. The use of this captivating technology as potential contender in the BIPV, as well as in the IoT and in Agrivoltaic field is presented in Section 4. Section 5 is devoted to the new trend in combining multiple types of devices into one unit, in order to enhance and/or diversified function of the integrated device. In this framework we are going to deal with the promises offered by the DSSC/DSSC and DSSC/Perovskite tandem devices. Finally, in Section 6 the challenges and outlook in BFDSCs field are featured on the basis of current development.

2. Operating principles of a DSSC and a BFDSC

In this paragraph, we delve into the operating principle of a DSSC cell by exploring its primary components and the suppression effects that arise. We introduce the most commonly used figures of merit in the literature that emphasize transparency. Subsequently, we analyse the albedo effect, which is crucial for the operation of bifacial PV devices.

2.1 Components and working system of a DSSC

A DSSC consists of three main components sandwiched between two conductive sheet glasses (Fig. 2):

- A mesoporous semiconductor layer, typically composed of TiO_2, serves as the working electrode (WE) upon which the dye is anchored.
- A liquid, gel, or solid electrolyte with a redox couple, commonly composed of iodide/triiodide ions.
- A catalyst layer, usually made of platinum. This layer is the counter electrode (CE).

Upon encountering the anchored dye on the semiconductor, photons initiate the generation of electron–hole pairs within the dye molecule. These photo-excited electrons (eqn (1)), occupying energy levels higher than the conduction band (CB) edge of TiO_2, swiftly transition into the TiO_2's CB. This process, characterized by a typical time constant k of approximately 10^{-12} seconds under one sun illumination (irradiation power of 100 mW cm^{-2}, temperature of 25 °C, and spectral intensity distribution of the light source matching the AM 1.5 global standard solar spectrum),[48] occurs rapidly (eqn (2)).[49]

Due to the photo-induced charge carrier transfer from the dye to the semiconductor oxide, the electronic density in TiO_2 increases giving rise to an electrochemical potential difference (DV) between TiO_2 and the electrolyte. The regeneration of oxidized dye molecules is achieved through electron transfer from the electrolyte mediator. The cathode catalyzes the reduction of I_3^- (eqn (4)). Thus, in this circumstance, the entire cycle is regenerative.[49]

$$\text{Dye} + h\nu \rightarrow \text{dye}^* \text{ light absorption (excitation)} \quad (1)$$

$$\text{Dye}^* + TiO_2 \rightarrow \text{dye}^+ + e_{CB}^- (TiO_2) \text{ electron injection } (k \approx 10^{-12} \text{ s}) \quad (2)$$

$$2\text{Dye}^+ + 3I^- \rightarrow 2\text{dye} + I_3^- \text{ dye regeneration } (k \approx 10^{-6} \text{ s}) \quad (3)$$

$$I_3^- + 2e^-_{\text{catalyst}} \rightarrow 3I^- \text{ electrolyte regeneration (reduction)} \quad (4)$$

The decay of the excited dye to the ground state and the "recapture" of injected electrons in the semiconductor CB by the oxidized dye or by the electrolyte species are undesirable processes that limit the electron transfer at the photoanode (eqn (5)–(7)).

$$\text{Dye}^* \rightarrow \text{dye decay of the dye excited state } (k \approx 10^{-10} \text{ s}) \quad (5)$$

$$\text{Dye}^+ + e_{CB}^- (TiO_2) \rightarrow \text{dye} + TiO_2 \text{ recombination (back reaction, } k \approx 10^{-4} \text{ s}) \quad (6)$$

$$I_3^- + 2e^-_{CB} (TiO_2) \rightarrow 3I^- + TiO_2 \text{ electron capture from mediator (dark current, } k \approx 10^{-2} \text{ s}) \quad (7)$$

Therefore, optimizing DSSCs necessitates ensuring that the electron injection (eqn (2)) and dye regeneration processes mediated by the electron donor (eqn (3)) are faster than the decay (radiative or non-radiative) of dye* (eqn (5)) and the back reaction between the injected electron and the oxidized dye (eqn (6)), respectively. In particular, the "dark current" is considered as the main loss mechanism for a DSSC.[50] Finally, the "efficient" regeneration of the charge mediator at the CE (eqn (4)) is fundamental; otherwise the device PCE could be limited. A deep knowledge and understanding of the electron-transfer kinetics is the key for identifying optimal materials of

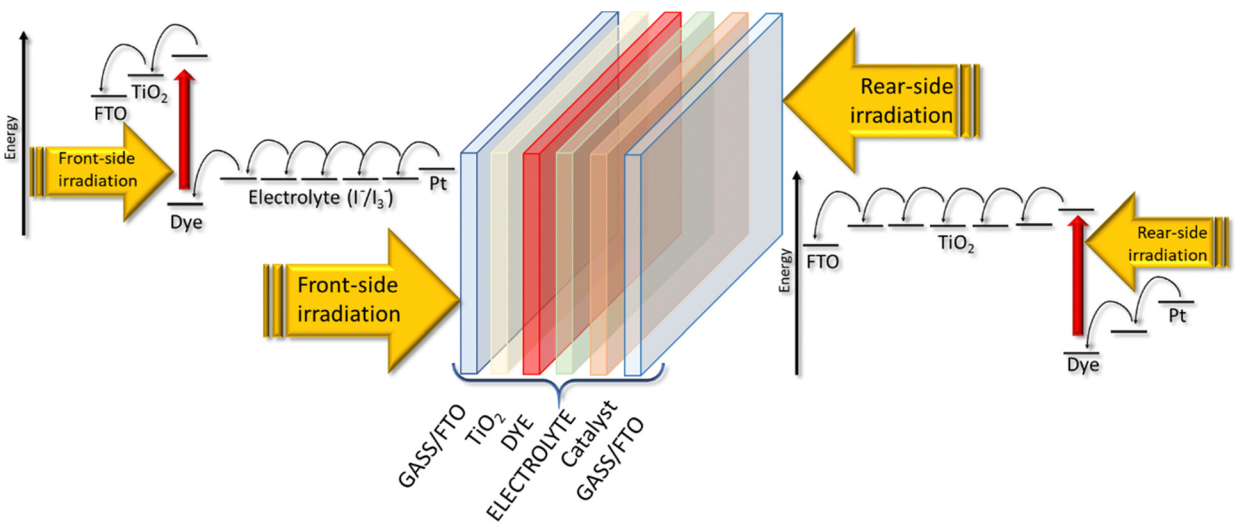

Fig. 2 Electron's motion in a BFDSC when irradiated from front and rear side (modified image from ref. 53).

the structure–function relationship of DSSCs. Extensive studies on the electron injection mechanism have been performed by numerous research groups.[51,52]

The PV figure of merit are explained below:

– I_{SC} (A) (short circuit current): represents the peak current produced when the cell is in a short-circuited state. J_{SC} (A m^{-2}) is the short circuit current density.

– V_{OC} (V) (open circuit voltage): denotes the highest voltage when the circuit is open.

– *I*–*V* curve (or current–voltage characteristic) is the relationship, between the current (*I*) through a circuit (or device) and the corresponding voltage (*V*) across it. Typically, is represented as a graph where *V* is the abscissa and *I* the ordinate. In this graph, when $I = 0$ then *V* is equal to V_{OC} and when $V = 0$ then *I* is equal to I_{SC}. Within the graph, two coordinates can be identified: I_{MPP} (or I_{MAX}) and V_{MPP} (or V_{MAX}), the current and the voltage at maximum power point, respectively.[49]

– FF (fill factor): $P_{MPP}/I_{SC}{\cdot}V_{OC}$, where P_{MPP} (or P_{MAX}) is the available power in correspondence of the maximum power point (in detail, P_{MPP} is equal to the product $I_{MPP}{\cdot}V_{MPP}$). Closer is the value of P_{MPP} with respect the product $I_{SC}{\cdot}V_{OC}$, more efficient – in terms of electric power generated – is the device.

– PCE (power conversion efficiency): is defined as the ratio between P_{OUT} and P_{IN}, where P_{OUT} is equal to the product $J_{SC}{\cdot}V_{OC}{\cdot}$FF and P_{IN} is the incident light, which corresponds to 1000 W m^{-2}, also known as 1 Sun (AM 1.5G condition). PCE is the most widely used figure of merit in the PV scientific community.

In BFDSC, the front PCE is the obtained photoconversion efficiency when the photoelectrode side is illuminated. The rear PCE is when the cell is illuminated from the side of the counter electrode. As matter of fact, being the front side the one that collects sunlight by direct incidence, results $PCE_{front} \geq PCE_{rear}$.

In Fig. 2, all the components of a DSSC are shown schematically, and the movement of electrons when light reaches both sides of the device is presented.[53] The thickness of the TiO_2 layer determines the amount of incident light absorbed, regardless of the illumination side. When light passes through a thin-thick dye-sensitized porous TiO_2 layer, 50% of the incident light is absorbed in accordance with the Beer–Lambert law.[54] This means that photo-excitation in the porous TiO_2 electrode primarily occurs near the side exposed to light. During front-side irradiation, the electron path within the TiO_2 conduction band is shorter, while the hole paths in the electrolyte, which extend from the reduced dye to the platinum counter electrode, are longer compared to rear-side irradiation. This effect can minimize the disparity between conversion efficiencies for front- and rear-side irradiation, leading to improved performance and cost-effectiveness for large scale solar power generation systems. Optimizing the thickness of the porous TiO_2 layer is crucial for enhancing DSSC performance. The photovoltaic characteristics demonstrate substantial variation depending on the thickness of the porous TiO_2. A pioneering study[53] revealed a linear decrease in open-circuit photovoltage (V_{OC}) with increasing TiO_2 film thickness. Under front-side irradiation, a 2.4 μm-thick dye-sensitized porous TiO_2 layer can absorb 50% of the incident light, creating a dye-excited region on the FTO side and a non-excited region on the electrolyte side. In open-circuit conditions, electrons injected from the dye into the TiO_2 layer spread uniformly from the FTO side to the electrolyte side within the porous TiO_2 layer.[55] Consequently, increasing the thickness results in a larger non-excited area, further lowering the V_{OC} upon averaging the electron density in the non-excited region.

2.2 Enhancing BFDSC: a figure of merit approach

Figures of merit (FoMs) provide meaningful metrics to assess the performance of different solar devices for a specific application. In the case of BFDSCs, appropriate FoMs are needed to assess the influence of bifacial illumination and quantify the additional irradiance on the cell's rear side. Unlike their monofacial counterparts, there is not yet a universally accepted standard in the PV community for characterizing the performance of BFDSCs.

Table 1 provides a summary of key FoMs that underscore the bifaciality feature in DSSC technology. These metrics provide meaningful tools to assess the capabilities of various BFDSCs designs and materials choices.

In this section, we will provide a description of the most widely used metrics in the DSSC literature such as BFF, AVT, LUE, and CRI. The other metrics mentioned, CCT[56] and TED[57]

Table 1 Summary of key FoMs and their descriptions

FoMs	Description
BFF	Bifaciality factor. Ratio of rear PCE to front PCE at equal irradiance. Range 0–100%.
AVT	Average visible transmittance on the whole visible spectra from 380 to 780 nm. Range 0–100%.
LUE	Light utilization efficiency. Trade off relationship between AVT and PCE.
CRI	Colour rendering index. 0–100 scale. Quantitively description of how accurately the colour of a given object is rendered.
CCT	Correlated colour temperature. Degrees Kelvin (K). It allows to understand of whether the colour is neutral, bluish white or reddish white.
TED	Transparency, efficiency, diffused light efficiency. Geometric mean of transparency, efficiency and diffused light.

will not be discussed here, as they are rarely present in the DSSC field at the moment and therefore outside the scope of this review. We provide the relevant references in case the reader wishes to delve deeper.

The ''bifaciality factor'', BFF (%)[58] defined as the ratio between the rear and front efficiencies at the same irradiance (eqn (8)), have been used by several academic researchers:

$$\mathrm{BFF} = [(\mathrm{PCE_{rear}}/\mathrm{PCE_{front}})] \times 100 \quad (8)$$

with BFF (%) values varying in the 0–100 range. Increasing BFF, the solar panel is more efficient at capturing light from both its front and rear, leading to a reduced difference in PCE between the two sides.

The opportunity to integrate DSSCs in BIPV, IoT, and greenhouses necessitates not only maximizing visible light harvesting for effective power generation but also ensuring visual comfort through suitable average visible transmittance (AVT) and a high color rendering index (CRI). Therefore, the aesthetic quality of BFDSCs is often quantified using these two main FoMs. Usually, the SCs transparency is estimated by AVT features in the 380–780 nm visible wavelength range, where the human eye is sensitive. In this framework, AVT becomes a critical FoM to assess the transparency level of BFDSCs. AVT value (%) is based on the integration of the device's transmission spectrum, the light source's spectrum and the spectral response of human eyes (photopic response) according to the following:[59,60]

$$\mathrm{AVT} = \frac{\int_{380}^{780} S_{\mathrm{AM1.5}}\mathrm{Tr}(\lambda)\cdot P(\lambda)\cdot \mathrm{d}\lambda}{\int_{380}^{780} S_{\mathrm{AM1.5}} P(\lambda)\cdot \mathrm{d}\lambda} \quad (9)$$

being, λ the wavelength, $S_{\mathrm{AM1.5}}(\lambda)$ the photon flux under AM 1.5G condition, Tr the transmittance and $P(\lambda)$ the photopic response of the human eye. The minimum acceptable glazing transmittance is between 25% and 38%.[61]

Traverse *et al.*[62] proposed a revolutionary FoM, named light utilization efficiency and defined as the product of AVT and PCE. The LUE (= AVT·PCE) provides a metric for comparing, on the same scale, high-performance transparent photovoltaics without neglecting efficiency in favour of transparency and *vice versa*.

Spectral quality FoMs assess the color rendering fidelity of transmitted or reflected light compared to natural daylight. This aesthetic performance is especially important for architectural integration.

On the other hand, the color rendering index (CRI) is a further essential FoM, particularly in BIPV, where it is the most aesthetic criteria used to quantifies the accuracy of a light sources to reproduce faithfully the color of a given object. However, since the color is a perception, impossible to measure, CRI is evaluated on the comparison with a natural or standard light source.[63] In other words, the CRI indicates quantitatively the color rendering ability by comparing the color of an object seen under a generic lighting with the color seen under a reference illumination source. Sunlight, which accurately renders the colors of objects, serves as a benchmark for all light sources. The CRI value ranges from 0 to 100. For glazing applications, a CRI of 80 or higher is typically considered acceptable, while a CRI above 90 is regarded as optimal.[64] CRI value is calculated within an evolution of functions as an average score on eight different test colour samples.[56]

2.3 Albedo's effect

In real-world scenarios, the bifacial property of the device is utilized to harness rear irradiance, also known as the albedo effect. This effect stems from the reflection of sunlight off nearby surfaces, such as the ground or buildings, which can significantly enhance the power output of bifacial solar panels. The albedo effect is particularly pronounced in environments with high reflectivity, such as deserts or areas with snow cover[58] (Fig. 3a). Fig. 3a shows the spectral reflectivity data for the chosen surface materials (grass, tree, snow, white marble, white dune and asphalt) obtained from the Ecostress Spectral Library provided by the NASA Jet Propulsion Laboratory.[65] Measuring albedo involves the use of an albedometer, a specialized instrument that captures the reflected and incident radiation. The calculation of albedo incorporates various parameters, including the azimuth angle, the zenith angle, in addition, the radiance in watts per square meter and steradian, which includes direct and diffuse components. For a more in-depth understanding of the albedo calculation formula, refer to this ref. 27.

The effectiveness of utilizing the bifacial feature for different PV technologies is primarily determined by their respective absorption spectra. DSSC can absorb across the entire visible spectrum and into the near-infrared region, depending on the chosen dye. Perovskite solar cells (PSCs) operate similarly, with their band gap adjusted to enhance absorption in specific regions of the spectrum.[66]

Amorphous silicon absorbs primarily in the shorter wavelengths of the visible spectrum, while crystalline silicon absorbs in the longer wavelengths and into the near-infrared region.

Analysis of albedo reflectance values has demonstrated that snow tends to exhibit a bias toward reflecting shorter wavelengths, particularly ultraviolet (UV) light. This preferential reflection of UV light favors hydrogenated amorphous silicon (a-Si:H) PV cells over other PV material technologies due to the energy gap values of the semiconductor. Conversely, paints tend to reflect preferentially within specific spectral ranges depending on their color, highlighting the strong situational dependence of PV technologies. These findings suggest the potential for categorizing bifacial PV module technologies based on their compatibility with diverse geographic, climatic, and ground characteristics, enabling the optimization of PV systems for specific micro-environments.[27,67] In this research work focused on solid-state DSSC, Hwang *et al.* simulated various rear reflectance (albedo) conditions and realized a cell tester for *J–V* characterization of bifacial cells.[68] The synergistic effects of irradiation from both sides result in improved sunlight utilization and enhanced PCE (Fig. 3b). When the device is measured simultaneously from both sides, thereby harnessing the Albedo effect, a remarkable increase in PCE is observed, reaching a maximum PCE of 10.4% compared to 7.9% and 3.9% achieved from the front and rear side, respectively. The bifacial cell tester is composed of a vertical sample holder that

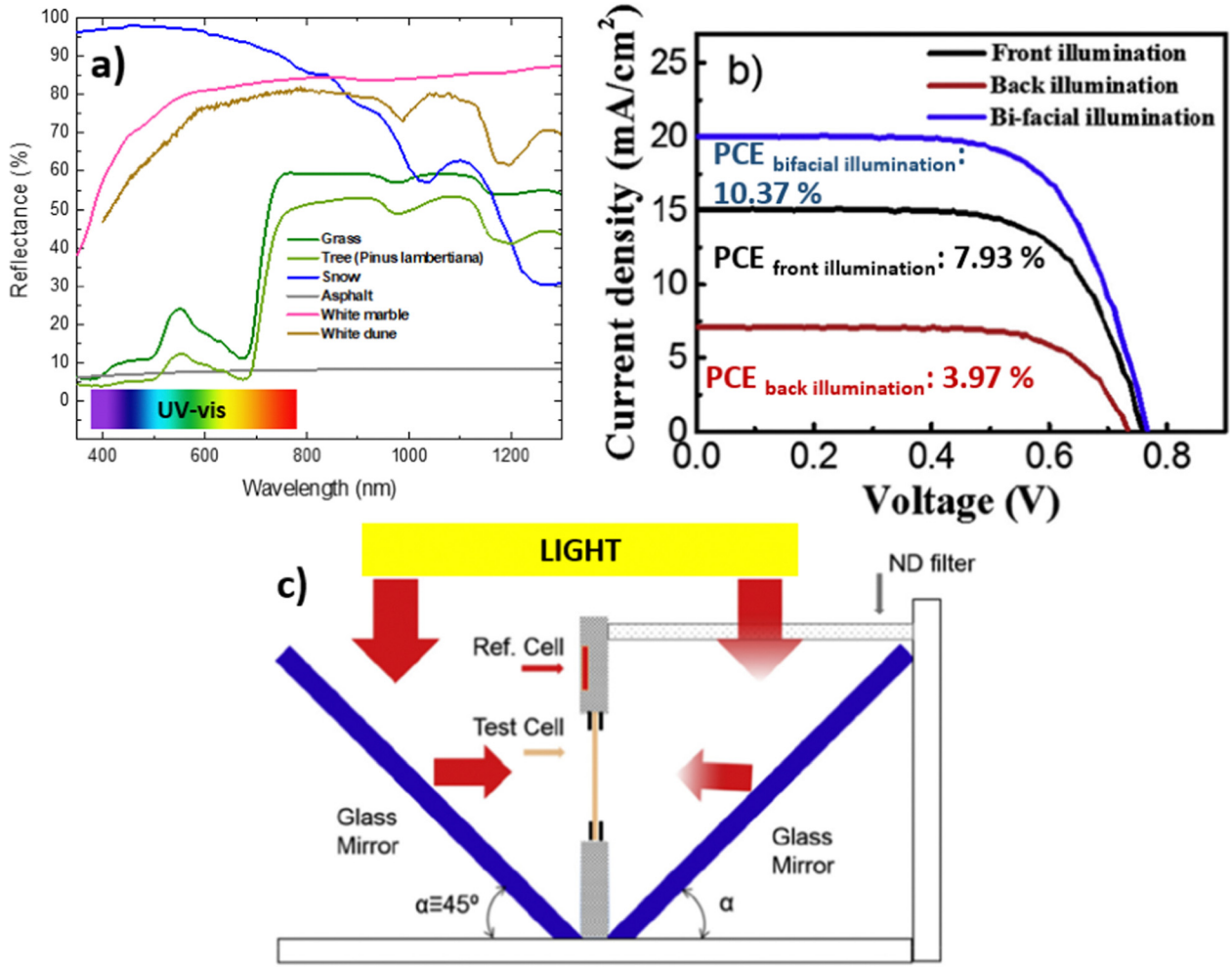

Fig. 3 (a) Reflectance data for different surface materials downloaded from Ecostress Spectral Library provided by the NASA Jet Propulsion Laboratory.[65] (b) *J*–*V* curves of a solid state BFDSC device by a back illumination, front illumination and bi-facial illumination (modified from ref. 68). (c) Schematic illustration of the light-splitting design in the bifacial cell tester, with simulated sunlight irradiating on both sides of the cell (modified image from ref. 68).

stands perpendicular to the base plate (Fig. 3c). Two mirror glasses are positioned symmetrically at a 45° angle to the sample holder. The sample holder includes means for contact with the photovoltaic cell on both sides, a reference cell for determining the irradiance after reflection on the mirror, and clamps to support the cell itself. To reduce the light irradiance on the rear side, various neutral density (ND) filters can be placed in front of the mirrors.

A recent paper,[69] focusing on bifacial PSCs, provides compelling evidence of the correlation between PCE and Albedo. The study meticulously demonstrates how the PCE trend consistently rises in response to increasing Albedo values.[69]

3. Bifacial components

In DSSCs, a liquid, gel, or solid electrolyte containing the redox couple fills the space between the two electrodes or active layer (WE and CE). Each part significantly influences the cell transparency. There is considerable interest in optimizing the transparency of the entire device, as well as the way in which the various parts of the DSSC correlate with each other. This section aims to provide a comprehensive overview of the optical properties of each individual component of DSSCs (CE, electrolyte, and WE) in order to exploit the bifaciality feature. We have reviewed recent advancements in engineering electrolytes and redox couples that exhibit exceptional transparency across visible wavelengths. This is aimed at minimizing light filtering and absorption. Ensuring high transparency for each component is crucial for enhancing rear-side illumination and the overall performance of bifacial devices.

3.1 Transparent conductive oxide (TCO)

The working electrode (WE) or counter electrode (CE) of a DSSC consist of a transparent conductive oxide (TCO) glass with a deposited semiconductor layer on the first and a deposited catalyser on the second. TCO are widely utilized as transparent electrodes in optoelectronic devices to fabricate flat panel displays such as smartphones, light emitting diodes and thin film

solar cells.[70] By doping intrinsically or extrinsically simple oxides, the electronic properties of a metal are obtained maintaining the transparency.[71] Fluorine-doped tin oxide (FTO) and indium tin oxide (ITO) are the most utilized semiconductor-based ternary compounds[49] in thin-film solar cell of the third generation. ITO is widely exploited in DSSC but also in PSC[42] as TCO or top electrode due to the capacity to produce high visible light transmittance (85%), low electrical resistivity (10 Ω), and good adhesion strength to various substrates. However, several drawbacks are discouraging its application since indium is a critical raw material. In terms of average abundance, indium is a scarce element in the Earth's crust and from a geopolitical point of view, China possess most of the indium reserves and its supply risk has become a major concern in the global market.[72] Furthermore, indium suffers of high prices, a demanding process, toxicity potential and sensitivity to both acid and basic environments.[80] On the other hand, FTO that is still the reference and the most utilized TCO, possess a higher work function than ITO (4.9 eV *vs.* 4.8 eV for ITO), an improved thermal stability, mechanical and chemical durability, less toxicity, and low price if compared to previously mentioned ITO.[73] Several TC materials have been proposed as electrode including carbon-based nanomaterials (carbon nanotubes and graphene).[74–77] However, not only the PCE values are mediocre, but also the sheet resistance does not meet the requirements for PV applications (R_S = 10 Ω and T = 90%).

3.2 Counter-electrodes for bifacial application

The counter-electrode (CE) plays a crucial role in determining the bifaciality and photovoltaic performance of DSSCs. An ideal CE should exhibit high electrical conductivity, electrocatalytic activity, long-term stability, and optical transparency. However, simultaneously optimizing all these properties is challenging. Pt (platinum) is a commonly used catalyst for DSSCs.[78] However, it is a costly and rare metal with limited resistance to corrosion from electrolyte redox solutions. This has motivated exploration of alternative cost-effective CE materials with bifacial capabilities, including conducting polymers,[79] carbon-based materials,[80–82] inorganic compounds, and their composites (Fig. 4).

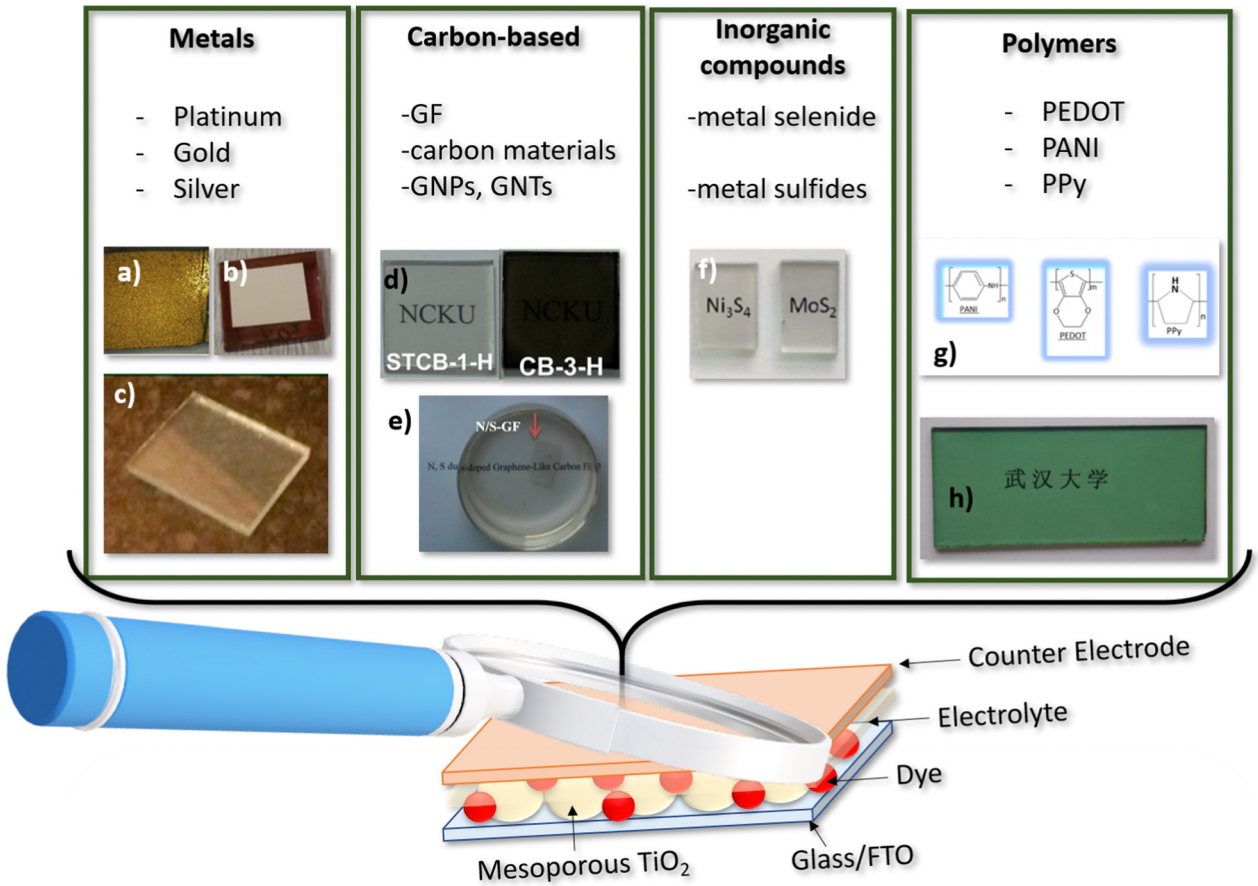

Fig. 4 Counter electrode categories from left to right: metals; carbon based compound; inorganic metal compounds and polymers. (a) Gold counter electrode reproduced and adapted from ref. 85, under Creative Commons BY-4.0 license; (b) silver counter electrode reproduced and adapted from ref. 87, under Creative Commons BY-4.0 license; (c) platinum counter electrode reproduced and adapted from ref. 93, under Creative Commons BY-4.0 license; (d) semitransparent carbon based electrodes reproduced from ref. 97 with permission from the Royal Society of Chemistry; (e) graphene films counter electrode reproduced and adapted with permission from ref. 106 Copyright © 2015 Elsevier B.V. All rights reserved; (f) metal sulfides counter electrode reproduced and adapted from ref. 112 copyright © 2015 Published by Elsevier Ltd; (g) PANI, PEDOT and Ppy molecules; (h) PANI counter electrode Reprinted (adapted) with permission from ref. 35 Copyright {2011} American Chemical Society.

In DSSC ambient, the CE collects the photogenerated electrons from the external circuit and reduces the redox species that function as mediators in the sensitizer's regeneration after electron injection, which appreciably impacts the PCE. In addition to the properties already mentioned, an ideal bifacial CE must have Tr ≈ 80% at $\lambda \approx 550$ nm, sheet resistance (R_S) < 20 Ω and charge transfer resistance (R_{CT}) in the range 2–3 Ω cm^2.[83] It is well recognized that in DSSCs, the charge carriers transport from the WE to CE is hindered by multiple resistances; R_S and R_{CT} being those strongly enslaved to the CE. R_S significantly governs the FF losses: at smaller R_S corresponds higher FF, resulting in higher PCE. In other words, a lower R_S indicates a higher conductivity of the catalytic CEs. On the other hand, R_{CT} reflects the charge transfer dynamic on the CE surface during a photoactivated process and, in this regard, smaller R_{CT} indicates better charge-transfer ability, faster diffusion process and lower photogenerated carrier recombination, meaning enhanced catalytic activity. R_{CT} can be explained in terms of exchange current density (J_0), as assessed by the following: $R_{CT} = (R{\cdot}T/n{\cdot}F{\cdot}J_0)$, where R, T, n, and F are the gas constant, temperature, number of electrons transferred in the elementary electrode reaction ($n = 2$) and the Faradays constant, respectively.[84]

Unfortunately, the simultaneous fulfilment of all the above requirements is almost unreachable. In the following paragraphs, a full description of the counter electrode advancement of each category, metals, carbon-based, inorganic compounds and polymers, are presented.

3.2.1 Metal CEs. Several metals such as gold,[85,86] silver[87–89] and palladium,[90,91] may be utilized as CE in DSSC but platinum[92] is the most widely utilized (Fig. 4a–c). Gold, despite its high cost, reduces transmittance significantly when used as nanoparticles, as highlighted by Gullace *et al.*[85] Silver, on the other hand, is too chemically reactive, making it unsuitable as a catalyst due to its reactive electronic structure.

Among metals, platinum demonstrates the highest catalytic activity,[93] towards I_3^- reduction, stability in I^-/I_3^- electrolytes,[94] and printability on rigid/flexible substrates. Pt CEs have enabled PCEs over 11% with I^-/I_3^- redox shuttles.[95] However, Pt may lack transparency and it is expensive. One effective strategy to balance conductivity and transmittance is the use of ultra-thin sputtered Pt layers. Venkatesan *et al.*[38] fabricated BFDSCs with Pt thicknesses varying from 0.55 nm to 12.1 nm on FTO glass substrates using magnetron sputtering deposition. The extremely thin 0.5 nm Pt CE achieved an impressive AVT of 76% in the visible range along with front and rear PCEs of 20.65% and 17.31%, respectively, under 200 lux indoor lighting (Table 2). This corresponded to a very high 84% BFF, among the best for state-of-the-art BFDSC systems.

The enhanced transparency enabled more rear-side light harvesting while the continuous ultra-thin Pt layer provided sufficient conductivity and electrocatalytic activity. Another synthesis route is photofabrication of Pt CEs by UV irradiation of hexachloroplatinic acid ($H_2PtCl_6{\cdot}6H_2O$) solutions deposited on rigid or flexible substrates. Popoola *et al.*[96] adopted this approach to produce flexible Pt CEs with better 400–700 nm transmittance than reference ITO/PET and FTO/glass substrates. BFDSCs with the photo-fabricated CEs achieved front and rear PCEs of 7.29% and 5.85% (Table 2), along with 78–86% BFF under simulated solar illumination. In contrast, thermally processed Pt CEs showed only 2.71% rear PCE, illustrating the strong impact of synthesis method on bifacial performance.

3.2.2 Carbon-based CEs. Carbon[97] nanomaterials (Fig. 4d and e), such as graphene and carbon nanotubes, offer high electrical conductivity, electrochemical activity, mechanical stability, and high specific surface area (SSA), serving as sustainable alternatives to the scarce Pt CEs. However, achieving a balance between conductivity and transparency remains a challenge for bifacial applications. Relatively thick carbon layers (greater than 10 μm) are generally required to ensure sufficient conductivity, but this compromises optical transmittance and reduces light penetration to the rear photoelectrode.

The initial exploration of graphene-based materials (*e.g.*, graphene nanotubes (GNTs), graphene nanoplatelets (GNPs), functionalized graphene sheets (FGSs), *etc.*) as transparent CEs

Table 2 Summary of some promising semi-transparent CE and their PV performances with WE, electrolyte and dye details

	CE	WE	Electrolyte	Dye	PCE MAX (%)	BFF (%)	Ref.	Year
Metals CE	0.55 nm Pt (200 lux)	TiO_2 (ML 8 μm)	Co(II)/Co(III), TBP, $LiClO_4$	Y123	20.65	84	38	2019
	Pt	TiO_2/SiO_2 (16 μm/3 μm)	I_2, PMII, GuSCN, MB	Z907Na	6.54	91	53	2008
	Pt	TiO_2 (ML)	LiI, I_2	N719	7.29	80	96	2018
Carbon-base	S-GF	TiO_2 (10 μm ML/2 μm SL)	I_2, LiI, TBP, GuSCN, BMII	N719	3.86	83	105	2015
CE	N-GFs	TiO_2 (ML 12 μm)	I_2, Lii, GuSCN, BMII, TBP in ACN	N719	3.12	83	106	2015
	$Cu_{2-x}Se$@N-doped Carbon	—	—	N719	7.61	76	109	2020
Inorganic	CQDs-CoSe	TiO_2 (ML)	NaI, KI, LiI, I_2, TBP	N719	8.54	76	115	2018
compound	Ru–Se alloy	TiO_2 (ML 10 μm)	—	N719	8.72	68	118	2018
	PR-MoS_2	TiO_2 (14 μm ML/3 μm SL)	GuSCN, PMII, I_2,TBP in ACN:VN (85 : 15)	N719	8.77	55	124	2020
Polymers	MoS_2/PEDOT	TiO_2 (ML)	LiI, I_2, TBP, GuSCN, BMII	N719	7	68	132	2020
	Pedot 90 nm (2000 lux)	TiO_2 (ML 4 μm/SL	—	Y123	26	88	134	2022
	Pedot 90 nm (200 lux)	3.5 μm/ML 4 μm)			24.16	93		
	PANI	TiO_2 (ML)	PMII, LiI, I_2, GuSCN, TBP	N3	6.54	65	35	2011
	PEDOT	TiO_2 (ML 6 μm)	$Co(bpy)_3(PF_6)_2$, $Co(bpy)_3(PF_6)_3$, $LiClO_4$, TBP	Y123	8.65	85	133	2018

in DSSC environments can be traced back to the work of Hong *et al.*[98] Subsequent research has shown that combining two distinct carbon materials, such as carbon nanotubes (CNTs) and graphene, can enhance the electrochemical activity of the CE.[99,100] CEs based on micron-thick graphene films have exhibited charge transfer resistances (R_{CT}) comparable to those of Pt-based CEs, with values potentially less than 1 Ω cm^2 for the reduction of I_3^-.[101] Kaven *et al.*,[102] while studying the electrochemical performance of graphene-based CEs in DSSCs using Cu(II/I) based electrolytes, reported remarkable catalytic activity, comparable to electrodeposited PEDOT catalysts and superior to Pt catalysts. When graphene-based CEs were incorporated into advanced DSSC configurations, PCE values as high as 14.7% were achieved,[13] surpassing the previous PCE record of 13%.[103]

Bu and his team[104] demonstrated the potential of transparent carbon-based CEs in the BFDSCs domain. Employing a straightforward and cost-effective "*in situ* carbonization" method and carefully adjusting the precursor's concentration/composition, they fabricated carbon-based CEs with excellent optical transmittance across the 400–800 nm wavelength range. These CEs also exhibited acceptable conductivity (R_S = 4.14 Ω) and catalytic activity towards I_3^- reduction (R_{CT} = 12.5 Ω cm^2). Their BFDSCs achieved PCE values of 5.04% and 6.07% under rear- and front-side illumination, respectively, with a BFF of 83%.

In 2015, Xu *et al.*[105] introduced chemical vapour deposition (CVD)-derived doped Graphene Films (GFs) as promising transparent CEs for BFDSCs (Fig. 4e). Specifically, they fabricated nitrogen-doped (N-GF), sulfur-doped (S-GF), and dual-doped nitrogen/sulfur (N/S-GF) films on FTO substrates using the CVD method. These doped GFs were used as CEs in DSSCs with an I^-/I_3^- redox couple and N719 sensitizer. The prepared doped GFs exhibited excellent AVT in the 350–1000 nm range, with optical transmittance values at 550 nm of 87.96%, 84.93%, and 87.05% for S-GF, N-GF, and N/S-GF, respectively. DSSCs with these CEs displayed front and rear PCE values of 3.86%, 3.74%, 4.22% and 3.19%, 3.07%, 3.45%, respectively, leading to BFF values of 83%, 82%, and 82% for S-GF, N-GF, and N/S-GF. Although the doped GFs exhibited higher R_{CT} values compared to the Pt-CE (R_{CT} = 2.70 Ω cm^2), they all demonstrated significant electrocatalytic activity at the electrode/electrolyte interface. The R_{CT} values were 2.85 Ω cm^2, 5.30 Ω cm^2, and 25.83 Ω cm^2 for N/S-GFs, N-GFs, and S-GFs, respectively.

Yang *et al.*,[106] utilized N-GFs, grown by CVD method, as transparent CEs in BFDSCs (Table 2). Their experimental results proved superior charge transfer at the graphene/electrolyte interface compared to untreated graphene, reflecting better electro-catalytic activity. It is well recognized that, electrical conductivity as well as catalytic activity are affected and often enhanced by nitrogen atom introduction into the graphene hexagonal lattice, giving rise to additional electron/ion pair as well as structural deformation *via* local strains.[107,108] The BFDSCs based on N-GFs as CEs exhibited better thermal stability together with higher transparency and BFF (83%) compared to Pt-CE (58%) and PCE value ~3 times higher than the devise using pristine graphene CE.

In 2020 Ou[109] *et al.*, with the aim to realize transparent high-performance and low-cost Pt-free CEs, realized a Co^{2+}/Co^{3+} mediated BFDSCs with carbon nanosheets as CE. Co^{2+}/Co^{3+} redox mediator is lighter in colour compared to I^-/I_3^- redox shuttles and exhibits weaker absorption in the 390–480 nm λ range. Co-mediated BFDSCs, using synthesized $Cu_{2-x}Se$@N-doped carbon nanosheets CEs, reached PCE values of 7.61% and 5.82% under front and rear irradiation (Table 2), respectively. The obtained PCE values were comparable to those of standard Pt based device. The resulting excellent PCE_{rear} value has been attributed to the weak absorption of the Co^{2+}/Co^{3+} electrolyte, as well as to the high optical transparency of the $Cu_{2-x}Se$@N-doped carbon nanosheets and its outstanding catalytic ability (R_{CT} = 4.4 Ω cm^2) to reduce Co^{3+} ions. The large SSA[110] and the uniform dispersion of $Cu_{2-x}Se$ nanoparticles provides numerous catalytic sites for Co^{3+} reduction, offering the desired superior electrocatalytic ability.

3.2.3 Inorganic compounds. Cost-effective inorganic metal compounds such as chalcogenides, nitrides, and carbides have also shown great promise as sustainable alternative catalyst for CE. Binary transition metal selenides are of particular interest due to their high optical transparency, favourable electrocatalytic activity, and relatively straightforward synthesis[111] (Fig. 4f). In 2014, Duan and colleagues[112] investigated optical and electrocatalytic properties of transparent CEs based on binary-alloy transition-metal selenides M–Se (M = Co, Ni, Cu, Fe, Ru). The transition nature of metals and their partially filled *d* orbitals, allows to the M–Se alloy, to receive electrons to form coordinated intermediates, a primary requisite for robust CEs. On the other hand, alloys have been recognized as a class of catalysts with significant higher selectivity and electrocatalyst activity compared to their single-metal counterparts.[113] An enhanced catalytic activity is a further critical need in determining effective CEs for DSSC applications. By a mild solution-based strategy,[36] transparent CEs based on the aforesaid M–Se alloys have been prepared, and their optical and catalytic features were compared with those of a Pt reference CE. X-ray diffraction and transmission Electron microscopy (TEM), revealed in the Me–S a distorted crystalline lattice, with many active sites for I_3^- adsorption and rapid reduction reaction ($I_3^- \rightarrow I^-$). In addition, high AVT (>70%) in the Visible and near-IR regions (400–1000 nm λ range), crucial for light penetration and dye excitation on the rear irradiation, was also observed. Moreover, electrochemical impedance spectroscopy (EIS) measurements corroborated the cyclic voltammetry (CV) results, demonstrating the high catalytic activity of M–Se alloys in the reduction of I_3^- ions. The obtained R_{CT} values were: 2.77 Ω cm^2, 2.84 Ω cm^2, 2.96 Ω cm^2, 4.90 Ω cm^2 and 5.44 Ω cm^2 for $Ru_{0.33}Se$, $Co_{0.75}Se$, $Ni_{0.85}Se$, FeSe, $Cu_{0.50}Se$, respectively (7.23 Ω cm^2 for the standard Pt-based CE). The assembled BFDSCs (M–Se catalyst on FTO substrate, N719 dye, I^-/I_3^- electrolyte couple) exhibited PCEs ranging from 8.30% to 9.22% for front irradiation and from 4.63% to 5.90% for rear irradiation, better results than those of Pt-based devices.[36]

With a focus on electron density enrichment at CE surface, in order to enhance its catalytic performances without sacrificing the transparency, Duan and co-workers[114] developed an

arrangement of tandem carbon quantum dots (CQDs) structure with CoSe to produce transparent CEs for BFDSCs. The excellent ability of CQDs to photo-generate electrons upon excitation from 350 nm to visible light enables their applications in photocatalysis. Additionally, their capability to act as electron mediators enhances the photocatalytic activity of other photocatalyst.[115] Due to these unique properties the manufactured CQDs-CEs showed in visible-light region optical transparency as high as ~70%. The assembled BFDSCs exhibited superior catalytic activity of the CQDs-CE and achieved PCE values of 8.54% and 6.55% for front and rear illumination, respectively, outperforming BFDSCs utilizing CoSe-based CEs (Table 2).

A quite similar strategy was also proposed by Zhang *et al.*[116] who reported BFDSCs with transparent sulphur-doped carbon quantum dots (S-CQDs)/metal selenide CEs. By a mild solution route and electrodeposition onto transparent metal selenide, CEs were prepared for high-performance BFDSCs applications. A well distribution of S-CQDs favoured light harvesting as well as fast electron transport from S-CQDs to catalyst, elevated the catalytic activity upon rear illumination testifying high electron concentration at CE surface. Using standard Pt-based CE, the DSSC yields a BFF of 56% while, by integrating S-CQDs with Pt CE, the final light-inducing S-CQDs/Pt tailored bifacial device increments the BFF to 62%. The maximized front and rear efficiencies are 9.15% and 6.26% for b-SC with Pt-free SCQDs/RuSe CE, respectively. The rear efficiency of 6.26% reported here[116] is in a very high level among state-of-the-art bifacial DSSC platforms. High PCEs and catalytic behavior of a Pt-free CE has been reported in DSSCs employing Ru–Se based CEs (RuSe, Ru_2Se, $RuSe_2$, $RuSe_3$), optimized by tuning *via* electrodeposition both stoichiometric Ru/Se ratio and bilayer number.[117] R_{CT} values of 7.53, 1.68, 8.61 and 41.02 Ω cm^2 for Ru_2Se, RuSe, $RuSe_2$ and $RuSe_3$ electrodes, respectively, revealed impressive catalytic activity of Ru–Se based CE. Lower R_{CT} implies lower resistance during charge diffusion processes and faster catalytic kinetics.[118] The superior catalytic activity of Ru–Se CE toward I_3^- reduction, and its high transmittance (> 0%) produced, in the corresponding BFDSC, PCEs of 8.72% and 5.9% with a BFF ~ 68% (Table 2). Liu *et al.*[119] synthesized *via* hydrothermal method, CEs based on ternary $(CoM)_{0.85}Se$ (M = Ni, Ru, Fe) alloys. The constructed CEs showed good AVT, reaching 80% for $(CoNi)_{0.85}Se$ based CE, which was benefit for the light harvesting from device rear side. All DSSCs based on the manufactured CEs, showed impressive PCEs for both front and rear sides, higher compared to the reference DSSC based on Pt-CE (PCE_{front} 6.72%, PCE_{rear} 3.16%). In details, DSSCs based on $(CoNi)_{0.85}Se$, $(CoRu)_{0.85}Se$, $(CoFe)_{0.85}Se$ alloy CEs displayed PCE_{front} of 9.16%, 8.09%, 7.58% and PCE_{rear} of 3.86%, 3.31%, 3.51%, respectively. Quasi-solid-state BFDSCs utilizing $CoSe_2$ nanorods (approximate lengths and widths of 70–500 nm and 20–60 nm, respectively) as CEs and polyvinylidene fluoride (PVDF) as quasi-solid-state electrolyte, have been proposed by Xia et coworkers[120] to improve PCE and long-term stability. PVDF and $CoSe_2$ were chosen owing to the good chemical stability and excellent optical transparency and flexibility of the former,[121] and high electrocatalytic ability for I_3^- reduction of the latter.[122] $CoSe_2$ based CE showed a remarkably lower R_S value (2.84 Ω) compared to Pt based CE (4.35 Ω), testifying its smaller bulk resistance, higher conductivity and easier electron transfer capability. Also, the R_{CT} value (2.54 Ω cm^2), representing the CE/electrolyte interface charge transfer velocity, was smaller than that of the Pt based CE (3.07 Ω cm^2), demonstrating superior electrocatalytic reduction activity.

The resulting BFDSCs reached the PCE values for the front and rear irradiation of 8.02% and 4.22%, respectively (BFF = 50%). In addition, the $CoSe_2$ based CE exhibited rapid photocurrent response and long-term photovoltaic stability.

DSSC-based on highly transparent MoS_2 based CEs, directly electrodeposited on FTO glass substrates *via* potential-reversal (PR) deposition mode, have been proposed by Chang *et al.*[123] The assembled CEs showed good transparence (~80%) and power/weight ratio together with high electrocatalytic activity, mainly attributed to a removal of Mo excess by implementing anodic bias as well as to the high surface area of the uniform thin layer. The assembled with PR-MoS_2 based CE reached satisfactory PCEs of 8.77% and 4.82% (BFF = 55%), rather equivalent with those of Pt reference device (9.01% and 5.67%) (Table 2).

3.2.4 Conducting polymers. Conducting polymers are organic polymers that can transport electrons through their conjugated chains. They can have either semiconductor or metallic behaviour.

Conducting polymers like PANI, PEDOT and PPy (Fig. 4g) have attracted great interest as Pt-free CEs owing to their facile synthesis, good conductivity, tunable morphology, and potential transparency.[124,125] However, their catalytic activity is generally lower than Pt, so they are often combined with other nanomaterials. Polyaniline (PANI), poly(3,4-ethylenedioxythiophene) (PEDOT) and polypyrrole (PPy) are among the most intensively studied conducting polymers for DSSC applications.

Aniline type conducting polymers included several analogous. Discovered over 150 years ago, PANI have attract more and more interest in the PV community in the past 50 years, owing their outstanding properties which could benefit the advancement of BFDSCs, offering appreciable PCEs from both rear- and front-side of the device. In addition, PANI can be synthesized in various porose nanostructure with different morphologies and high SSA, improving the catalytic activity.[126]

In 2011,[35] transparent PANI based CEs was synthesized by "*in situ*" polymerization of aniline monomers on FTO glass substrate (Fig. 4h). The grains of PANI films appeared homogeneous and smooth, with grains size of ~250 nm, composed of smaller granules with diameters of ~20 nm and cauliflowerlike-shaped. This kind of morphology, allowing high SSA, supported the favourable PANI's catalytic activity. Moreover, the PANI's thin film showed excellent transparency in the 450–750 nm λ range with a maximum transmittance of ~74% at ~510 nm and PCE of ~4.26% illuminated from rear (BFF ~65%). Later Wu and colleagues,[127] using modified PANI with 4-aminothiophenol (4-ATP/PANI), as transparent electrocatalytic CE for BFDSCs, reporting PCE values of 6.70% and 4.15% (BFF of 62%), and 8.35% from both-sides. 4-ATP was used to diminish the unfavourable PANI/FTO interfacial resistance and accelerate the charge transport between them. The device high PCE, was attributed to

fine microporous structure, high transmittance, good electrocatalytic activity to I_3^- reduction, low charge transfer resistance on electrolyte/electrode interface of the 4-ATP/PANI based CE. In the design of CEs, various chemical dopants including SO_4^{2-}, ClO_4^-, BF_4^-, Cl^- p-toluenesulfonate (TsO), *etc.*,[128] have been incorporate or embed with PANI polymer chain in order to improve the PCE of PANI BFDSCs. As an example, SO_4^{2-} doped PANI film exhibited porous morphology, higher reduction current for the I_3^- reduction and lower R_{CT} (1.3 Ω cm^2) than the Pt based CE (2.3 Ω cm^2).[129]

PEDOT is a further frequently used conducting polymer suitable for large scale and cost-effective productions with excellent transparency and conductivity (300–500 S cm^{-1}),[130] much higher than that of various counterparts (*e.g.*, PANI, polypirrole (PPy), polythiophene, *etc.*). However, its catalytic activity remains lower compared to that of Pt based CE or other metals-based CEs. Therefore, other catalytic materials have been combined with PEDOT to better utilize its superior properties in BFDSCs development. Xu *et al.*[131] reported highly transparent PEDOT:PSS films (78% ≤ Tr ≤ 83.5% at ∼550 nm), prepared by spin coating and treatment with small amount of additives (iodine, IOD, DMSO and PEG200-) for CE's catalysts use in BFDSCs configurations.

The constructed BFDSCs, reached PCEs ranging from 4.36% to 5.29% and from 2.36% to 2.62% for front and rear illumination, respectively, and BFF varying from 45 to 55%, depending on the transmittances of the modified PEDOT:PSS films. The PCE values of the modified PEDOT:PSS films has been attribute to a high surface roughness, responsible of an enhanced catalytic activity. Moreover, the BFDSCs with the modified PEDOT:PSS films showed comparable PCE_{front} to that of conventional Pt based DSSCs, but higher PCE_{rear} than the latter (1.66%). Xu *et al.*[132] for the first time, synthesized transparent organic/inorganic hybrid composite films MoS_2/PEDOT with the aim to merge the conductivity and electrocatalytic ability of the two components. Nanosized MoS_2 synthesized by hydrothermal method were deposited onto an FTO glass substrate by spin-coating. Then, on the top of the obtained MoS_2 layer, PEDOT film was electrochemically polymerized to form the composite MoS_2/PEDOT CEs. MoS_2 as transition-metal compound, exhibits excellent conductivity and catalytic properties, moreover, it improves the continuity of the PEDOT film and reduces the pores at PEDOT film surface, improving the conductivity of the PEDOT/MoS_2 composite film. BFDSCs using MoS_2/PEDOT composite CE exhibited PCE_{front} of ∼7% and PCE_{rear}∼ of 4.82% (BFF ∼ 70%) (Table 2) together a good transmittance (∼70%) at ∼510 nm. Finally, the measured R_S (5.26 Ω), proved the excellent conductivity and catalytic properties of the composite CEs.

In 2018, Kang *et al.*[133] preparing DSSCs consisting of PEDOT based CE, $Co(bpy)_3^{3+/2+}$electrolyte and Y123 dye, reached PCE_{rear} higher of ∼82% compared to that of reference Pt based CE under front-illumination. The constructed device achieved the remarkable PCE values of ∼8.65% and ∼7.48% with a BFF of ∼85%.

PEDOT CEs for indoor applications, synthesized *via* electrochemical deposition onto FTO glass, have been recently proposed by Venkatesan *et al.*[134] By optimizing amount, polymerization time and thickness (90 nm) of the PEDOT layers, the prepare CEs showed higher Tr (∼70%), ion diffusivity (4.34×10^{-9} cm^{-2} s^{-1}) and ionic conductivity (5.41×10^{-5} S cm^{-1}), as well as low R_{CT} (2.38 Ω cm^2) at the CE/electrolyte interface than those of the reference cell (Pt-based CEs). Front and rear PCEs of 24.16% and 22.45%, respectively, (BFF = 93%) were obtained for DSSC using the CE with 90 nm thickness PEDOT layer, under light illumination of 200 lux (Table 2).

Polypyrrole PPy, is another class of conducting polymers that has attracted interests in DSSC technology. Produced by the pyrolysis of tetrahydropyrrole gives rise to highly conductive materials. Differently by their doped film which are blue or black, the pristine PPy films appear yellow but darken in air due to oxidation. In DSSCs ambient, the main issues of PPy CEs are correlated to their high R_{CT}, and no good enough conductivity,[124] which in turn are correlated to the morphology as well as to the synthesis procedure. In this framework, chemical dopants, incorporate or embed with PPy polymer chain, to enhance the PPy conjugation are often used.[135,136] Wu *et al.*,[137] first reported the use of PPy as CE materials in DSSCs in 2008. Bu *et al.*[138] prepared CEs for BFDSCs, by *in situ* polymerization of PPy monomer on FTO glass substrate. The BFDSCs based on these CEs showed PCEs of 5.74% and 3.06% front- and rear-side illumination, respectively, improving those of a reference Pt-based DSSCs.

The opto-electrochemical features of PPy films displayed a transmittance that gradually increases with decreasing the monomer concentration *vs.* a J_{SC} which follows the reverse behaviour, and R_{CT} (2.46 Ω cm^2) comparable to that of Pt (2.53 Ω cm^2), proving an adequate catalytic activity, thanks to PPy films SSA and porous structure.

Wang *et al.*[139] study showed that FeS_2 nanocrystal (NC) ink is a promising, cost-effective alternative. It exhibits excellent electrochemical catalytic activity and stability in reducing triiodide to iodide. Recently, Yao and co-workers,[140] combined pyrrole with MoS_2 by a reflux method and next "*in situ*" polymerization, to make highly transparent PPy-MoS_2 based CEs.

By comparing the as prepared CEs with those without MoS_2 addition, a larger maximum bifacial PCE of ∼9.48% under both-side irradiation was observed.

MoS_2 is characterized by high transparency and large SSA which provides a large number of I_3^- reduction active sites and favours electron transfer as well as excellent catalytic properties.[141]

In addition, the covalent bonds between N and Mo atoms, allows to control the grow of PPy onto the MoS_2 surfaces as well as the CE transparency. Moreover, PPy and MoS_2 as electron donors and electron acceptors, respectively can form a conductive matrix by antibonding interactions $Mo_{d\pi}/N_{p\pi}$ which increases the electron delocalization and the PPy conductivity. The higher optical transmittance (∼70% in visible region) and the best PCE_{front} and PCE_{rear}, were obtained employing PPy-4 wt%MoS_2 complex CE. Fig. 5 aims to gather the best proposed counter-electrodes in the literature in terms of transmittance and BFF obtained values. In Table 2, we report a summary of promising semi-transparent CE and their PV performance with all detailed information regarding WE, dye and electrolyte.

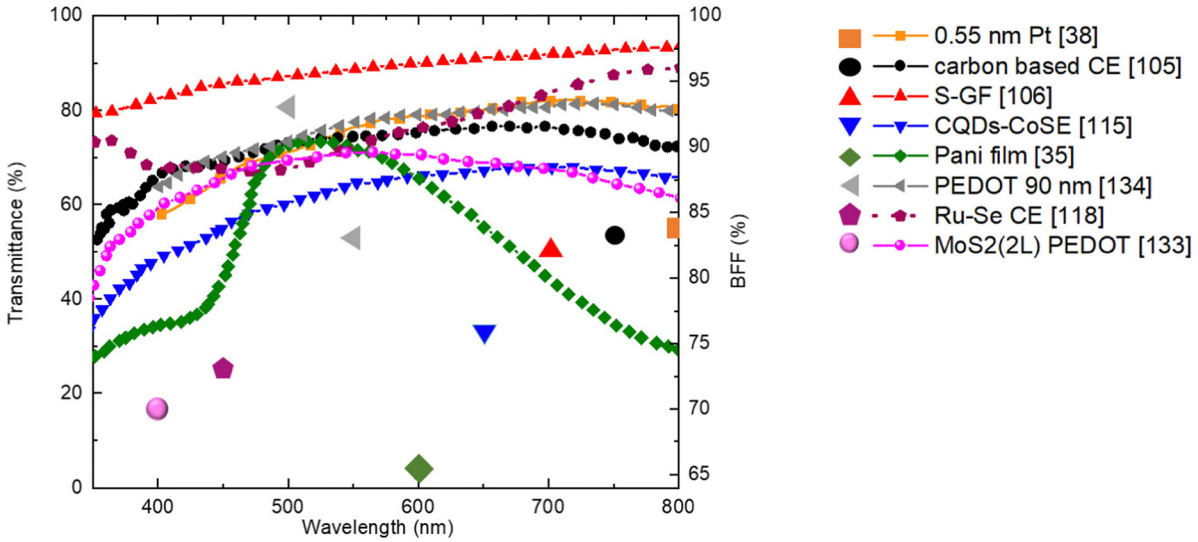

Fig. 5 Transmittance (right *Y* axis) and BFF (left *Y* axis) of semi-transparent CEs which gave the best performance in terms of PCE and BFF (>65%).

3.3 Transparent electrolyte

In the quest for sustainable energy solutions, electrochemical systems, and photovoltaics, particularly DSSCs, have been focal points of scientific exploration. A critical component in DSSCs is the electrolyte, which facilitates redox reactions, regenerates the oxidized dye, and maintains charge neutrality by transferring electrons to the counter electrode. The performance of DSSCs is closely related to the viscosity, dielectric properties and conductivity of the electrolyte, which determine the rate and quantity of charge transfer. Adjusting the proportion of electrolytes, particularly the concentrations of redox couple, can significantly impact the performance of DSSCs. For instance, increasing the concentration of the reducing specie from 0.1 to 0.8 mol L^{-1} can effectively improve the J_{SC} and consequently the PCE of the cell. However, the V_{OC} remains almost unchanged with variations in concentration of redox couple.[142] The iodide/triiodide (I^-/I_3^-) redox couples, or iodine-based electrolytes (IBEs), are frequently used due to their favourable kinetics and high carrier collection efficiencies, despite drawbacks such as low redox potential, corrosive tendencies, and competitive blue light absorption.[143] Indeed, the transmittance spectrum of IBEs typically shows UV-Visible absorption ranging from 300–500 nm, contingent upon solvent composition and solution concentration. Yet, this attribute might sometimes compromise the PCE of BFDSCs during rear illumination. This is due to potential obstruction of optical penetration and light absorption by the IBE. Functioning like a filter, the IBE may obstruct the blue-green light region while enabling the transmission of red light. Despite this, these impediments can be effectively addressed through astute optimization strategies.[144] These strategies are expected to include enhanced optical transparency at ideal conductive concentrations, superior physical and chemical attributes such as solubility, non-volatility, and thermal stability, and advancements in cumulative PCE and BFF under rear illumination. To address these challenges, there has long been a growing interest among researchers to investigate transition metal complexes as promising alternatives for redox mediators.[145]

The liquid electrolyte (LE) such as IBE, presents some problems for long term stability and device sealing in addition to those mentioned above. The use of solid state[146](SSE) or quasi solid[68] electrolytes (QSSE) is encouraged to overcome these limits also in BFDSCs. The development of DSSC using polymer-based electrolytes, for example, such as a gel gives rise to a quasi-solid-state DSSC, and the use of a pure polymer electrolyte (without solvent), gives a solid-state DSSC.[147] Electrolytes based on both organic solvents and ionic liquids can be gelated, polymerized, or dispersed with polymeric materials. Both types of liquids have been used as starting materials, and the inclusion of gelating or polymeric agents transforms the electrolyte into a quasi-solid electrolyte.[148] Typically, these quasi-solid electrolytes show conversion efficiencies that are lower than that of the liquid redox electrolyte. This effect can be attributed to limitations in the mobility of the redox couple components in QSSE. Another strategy for the development of solid-state devices involves the use of transition metal complexes as an alternative redox mediator to the iodine–iodide couple. These complexes offer elevated redox potentials, corrosion resistance, and could be modified by change the ligands to find a solution to the blue light absorption issue of I^-/I_3^- couples, which could lead to notable efficiency improvements in DSSCs.[149] In particular, some transition-metal complexes such as Co^{3+}/Co^{2+} (complex) and Cu^{2+}/Cu^{+} (complex) have been employed and investigated as redox shuttles in DSSC electrolytes.[150,151] The optical redox properties of these complexes are pivotal for enhancing the PCE in BFDSCs. Given the bifacial configuration of BFDSCs, the incorporation of materials with superior transparency is crucial to ensure effective light propagation to the photoactive layer from both directions. Some of these transition metal complexes, because of their

lower light absorbance, can play an essential role in BFDSCs as highly transparent electrolytes. Furthermore, they offer significant advantages in aesthetic and integrated applications such as BIPV, urban-street PV applications, automotive industry, and more, where light management and the transmission/absorption properties under rear-light illumination are crucial.[152,153] Cobalt polypyridine salts are noteworthy for their high electrocatalytic activity towards the reduction of triiodide, making them attractive candidates for DSSCs. Equally, copper polypyridine salts present similar electrocatalytic capacities, thereby underlining their increasing importance in DSSC research and application.[145] The design and optimization of cobalt and copper polypyridine complexes are guided by the principles of ligand field theory. This theory elucidates the manner in which interactions between the metal ion and surrounding ligands affect the energy levels of the metal ion's d orbitals, in turn influencing the chemical and physical properties of the complex. These cobalt and copper polypyridine complexes have been the focus of extensive research over recent years, considering their promising applications as electrolytes in DSSCs. These complexes have different absorption spectra, which can be attributed to the different electronic configurations and relative energy levels of the two ions.

In the case of cobalt polypyridine complexes, the cobalt ion Co^{+2} has a d^7 electronic configuration, when the ligand field is weak, it has five electrons in the t_{2g} orbitals and two electrons in the e_g orbitals resulting in a high-spin configuration. Beside when the ligand field is strong, only one electron occupies the e_g orbitals, resulting in a low-spin configuration as reported in Fig. 6. A notable drawback of Co complexes is the slow mass transport and substantial reorganization between d^7 (high-spin) and d^6 (low-spin) states, which confines the V_{OC} to a maximum of 1 V. In the case of copper polypyridine complexes, the copper ion has a d^9 electronic configuration, which means that it has one electron in the t_{2g} orbitals and two electrons in the eg orbitals. The remaining six electrons can occupy either the t_{2g} or the e_g orbitals, again depending on the ligand field strength. When the ligand field is weak, the six electrons occupy the eg orbitals, resulting in a high-spin configuration. However, when the ligand field is strong, the six electrons occupy the t_{2g} orbitals, resulting in a low-spin configuration. The difference in the electronic configuration and relative energy levels of the d orbitals of cobalt and copper ions can be explained by the ligand field strength of the surrounding polypyridine ligands. The stronger ligand field of the polypyridine ligands in cobalt polypyridine complexes results in a larger energy separation between the t_{2g} and eg orbitals of the cobalt ion, which leads to a stronger MLCT band in the absorption spectrum. On the other hand, the weaker ligand field of the polypyridine ligands in copper polypyridine complexes results in a smaller energy separation between the t_{2g} and e_g orbitals of the copper ion, which leads to a weaker MLCT band in the absorption spectrum. In conclusion, the application of ligand field theory to cobalt and copper polypyridine complexes provides insights into the electronic structure and properties of these complexes. Here we report some of the important history of these two families of ions salts culminated in the production of remarkably efficient DSSCs, as evidenced by the selection of some DSSCs with PCE $\geq$ 12%[144] featured in Table 3.

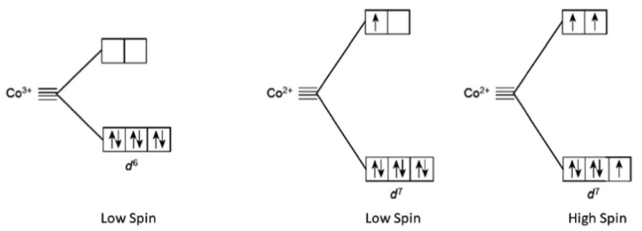

Fig. 6 High spin and low spin cobalt ions configuration for Co^{2+} and Co^{3+} in presence of field ligand.

Table 3 The main outstanding photovoltaic performances of DSSCs by using some redox electrolytes: IBEs, Co^{3+}/Co^{2+} and Cu^{2+}/Cu^{+} redox shuttles under standard AM 1.5G (100 mW cm^{-2}) illumination are summarized

EL	DYE	PCE (%)	Ref.	Year
$Cu(tmby)_2^{+/2+}$, LiTSFI, CEMI	SL9/SL10	15.2	169	2022
I_2, LiI, TBP	Y123	12.7	145	2022
$Cu(tmby)_2^{+/2+}$, LiTSFI, MBI	MS5/XY1b	13.5	14	2021
$Co(bpy)_3^{2+/3+}$, LiTSFI, TBP	SGT-149/SGT-021	14.2	168	2020
$Cu(tmby)_2^{2+/3+}$, LiTSFI, NMB	R7/Y123	12.7	167	2020
$Cu(tmby)_2^{2+/3+}$, LiTSFI, MBI	XY1b/Y123	13.1	166	2018
$Co(bpy)_3^{2+/3+}$, $LiClO_4$, TBP	SGT-021-HCA4	12.0	150	2017
$Co(phen)_3^{2+/3+}$, $LiClO_4$	ADEKA-1/LEG4	14.3	13	2015
$Co(phen)_3^{2+/3+}$, $LiClO_4$	ADEKA-1/SFD-5	12.8	160	2015
$Co(bpy)_3^{2+/3+}$	GY50	12.7	159	2014
$Co(bpy)_3^{2+/3+}$, LiTSFI, TBP	SM371	12.0	103	2014

3.3.1 Cobalt redox complexes. Grätzel and his team pioneered one of the first studies on cobalt redox complexes, revealing the charge-transfer kinetics of a unique single-electron redox pair. This study focused on $Co^{III}(dbbip)_2^{3+}/Co^{II}(dbbip)_2^{2+}$ within N-719 sensitized DSSCs.[154] In 2002 Bignozzi and his team presented non-iodine DSSCs that utilize a range of Co(II) and Co(III) complexes featuring substituted bipyridine ligands.[155] Several years ago, Feldt and colleagues developed high-performing cobalt-based mediators for DSSCs, surpassing the efficiency of those with iodide-free electrolytes.[156] In their pursuit of enhancing DSSC performance, they ingeniously combined a cobalt polypyridine complex with an organic sensitizer. This amalgamation allowed a comprehensive examination of various organic sensitizers and cobalt polypyridine redox mediators' effects on DSSCs' efficiency and the underlying transport and recombination mechanisms.

By adeptly coordinating the properties of the dye and cobalt redox mediator, they successfully circumvented constraints introduced by recombination and mass-transport. The researchers adopted organic dyes D29 and D35, which possess greater extinction coefficients than conventional ruthenium sensitizers. This allowed for the incorporation of thinner TiO_2 films.[157]

They introduced insulating butoxyl chains onto the dye, a strategy that curtailed recombination and permitted the utilization of redox pairs with superior diffusion coefficients and optimally suited redox potential. This strategic approach resulted in enhanced photocurrent and photovoltage. Crucially, the team minimized the recombination and mass transport issues typically

associated with the electrolyte by expertly adjusting the steric bulk of both the dye and the redox mediator.

They examined a series of cobalt complexes featuring distinct redox potentials as one-electron outer-sphere redox mediators in DSSCs. Cobalt complexes, including $[Co(bpy)_3]^{3+/2+}$, $[Co(dmb)_3]^{3+/2+}$, $[Co(dtb)_3]^{3+/2+}$, and $[Co(phen)_3]^{3+/2+}$ demonstrated standard redox potentials of 0.56, 0.43, 0.43, and 0.62 V, respectively, all utilizing hexafluorophosphate (PF_6^-) as the counterion. Theoretically, the V_{OC} value of the devices should increase along with the cobalt complexes' redox potential. However, an optimal V_{OC} and J_{SC} were achieved from the $[Co(bpy)_3]^{3+/2+}$ redox couple due to the optimal driving force for dye regeneration, diminished mass transport restriction attributable to the less bulky $[Cu(bpy)^3]$ complexes, and recombination reduction due to the inclusion of steric bulk in the D35 dye.[156] Overall, among investigated dyes the D–π–A structure-based Zn–porphyrin sensitizer emerges as a promising dye for cobalt complex redox electrolytes, illustrating the potential to achieve remarkable efficiencies. The cobalt complex $[Co(bpy)_3]^{3+}/^{2+}(B(CN)_4)^{-3}/^{2}$ exhibits a standard redox potential of 0.57 V (*vs.* NHE) and is composed by a bidentate ligand, 2,2′-bipyridine (bpy), and tetracyanoborate $(B(CN)_4)^-$ as the counterion. Employing this redox couple and the donor–π-bridge–acceptor (D–π–A) structured Zn porphyrin dye YD2-o-C8 with the addition of an organic dye has been achieved the efficiency to 12.5% under simulated 1-sun (AM 1.5G) illumination.[158] The dye YD2-o-C8, complete with octyloxy groups, allows slower recombination of the injected electron in TiO_2 with $Co^{3+}(bpy)_3$ and absorbs light across the entire visible range. Employing the D–π–A structured Zn–porphyrin SGT-021 dye and cobalt complex redox shuttle $[Co(bpy)_3]^{3+/2+}(B(CN)_4)^{-3/2}$, Kang *et al.* achieved a 12.1% efficiency under 1-sun illumination.[150] Yella *et al.* with $Co(bpy)_3^{2+/3+}$ and GY50 achieved a PCE of 12.7%.[159]

Mathew and co-workers achieve a PCE of 12% and 13% with $Co(bpy)_3^{2+/3+}$ and SM371 and SM315 respectively[103] Kakiage *et al* with $Co(Cl\text{-}phen)_3^{2+/3+}$ and ADEKA-1 achieved a PCE of 12.5%[13] while co-sensiting with SFD5 and employing $Co(phen)_3^{2+/3+}$ measured a PCE of 12.8%.[160] Finally combining ADEKA-1/LEG4 and $Co(phen)_3^{2+/3+}$ found a PCE of 14.3%[13] (Table 3).

3.3.2 Copper redox complexes. Since 1995 copper salts have been considered as potential replacements for the I^-/I_3^- redox pair in DSSCs. Indeed copper is nontoxic, abundant in the Earth, and comparatively cheaper than Cobalt. CuI and CuSCN salts as redox solid mediator has been pioneered studied by Tennakone[161] and Kumara.[162,163]

Cong *et al.*[164] discovered that the device using the $[Cu(bpye)_2]^{2+/+}$ redox shuttle resulted in higher power conversion efficiency (PCE) and open-circuit voltage (V_{OC}) than Cobalt redox electrolytes. This outcome was primarily due to the $[Cu(bpye)_2]^{2+/+}$ complex's more positive redox potential (approximately 0.59 V). The $[Co(bpy)_3]^{3+/2+}$ redox pair, while useful, posed a challenge in terms of mass transport that could possibly be addressed by altering the ligand of the Co complex to bpye. Pradhan *et al.*,[165] through their research using various redox electrolytes, found that the $[Cu(dmb)]^{2+/+}$ redox shuttle presented less mass transport issues, better diffusion, and required a relatively low driving force (around 0.1 V) for efficient dye regeneration when compared to the $[Co(bpy)_3]^{3+/2+}$ redox shuttles. Recently, studies have shown promising results with the use of copper complexes in combination with additives to improve the stability and performance of copper-based DSSCs.[145]

Cao and his team[166] achieved remarkable performance by enhancing the light-harvesting efficiency through co-sensitization of two D–π–A structured organic dyes, namely Y123 and XY1b, combined with the co-adsorbent CDCA. Notably, they also achieved a high fill factor (0.79) for copper electrolytes, attributable to improved mass transport brought about by a high concentration of the redox pair and the absence of $TiCl_4$ post-treatment. Their unique direct contact device design allowed the redox shuttle to diffuse through TiO_2 nanopores, significantly reducing the Warburg resistance by shortening the diffusion path.

In 2020, Ren's team documented a DSSC boasting an efficiency of 12.7% by leveraging the $[Cu(tmby)_2]^{2+/+}$ redox electrolyte in conjunction with co-sensitized organic blue dye R7 and Y123 dye.[167] Subsequently, in 2021, Zhang and his colleagues utilized the $[Cu(tmby)_2]^{2+/+}$ redox mediator in conjunction with the D–π–A structure-based organic dye MS5.[14]

Owing to the higher positive redox potential of the $[Cu(tmby)]^{2+}/[Cu(tmby)]^{+}$ complexes (approximately 0.87 V *versus* NHE), several high-efficiency porphyrin dyes such as SGT-021 ($E_{HOMO} \approx 0.82$ V),[150] SM315[103] ($E_{HOMO} \approx 0.89$ V) and some organic dyes including SGT-149 ($E_{HOMO} \approx 0.84$ V)[168] cannot be investigated with this Cu redox shuttle because of the insufficient driving force for dye regeneration, in particular with SGT-149, a hexyloxy-phenyl substituted fluorenyl derivative, was demonstrated high PCEs of 11.7% with a $[Co(bpy)_3]^{2+/3+}$ redox electrolyte. Moreover, co-sensitization of SGT-149 with SGT-021 porphyrin dye, achieved through a simple "cocktail" method, yielded an outstanding PCE of 14.2% with the same cobalt-based electrolyte.

Recently, the use of a Cu complex, the $[Cu(tmby)_2]^{2+}/[Cu(tmby)_2]^{+}$ redox shuttle, has been reported to achieve a power conversion efficiency (PCE) of 15.2% under 1-sun illumination with V_{OC} over 1 V in DSSCs.[169] While this redox shuttle significantly enhanced V_{OC}, further improvement in the J_{SC} is challenging. This difficulty arises due to the competition between Cu complex absorption and the need for a dye with a higher positive HOMO level in the visible light spectrum, which restricts complete utilization of the entire visible light range. For the future there is a need for research to identify an appropriate redox shuttle with a redox potential ranging between 0.45 and 0.65 V, or alternatively, to modify a ligand to adjust the redox potential of Cu complexes, enabling the use of most porphyrin and organic dyes.

Concluding, the prevailing role of iodine as the redox mediator in DSSCs is being increasingly challenged. The drive for enhanced stability and cost-effectiveness has spurred considerable research efforts towards iodine-free redox couples. Transition metal complexes, notably copper and cobalt-based couples, have emerged as compelling alternatives, demonstrating favourable electrochemical attributes and resilience.

The efficiency of DSSCs hinges significantly on redox kinetics, or the speed at which electron transfers occur within the redox pair. Thus, a thorough understanding and optimization of these

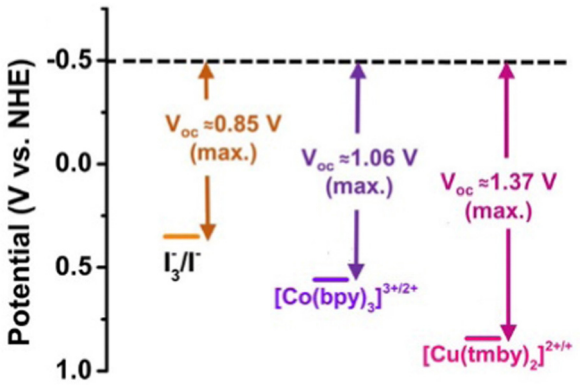

Fig. 7 Potential of for I_3^-/I^-, $[Co(bpy)]^{3+/2+}$and $[Cu(tmby)_2]^{2+/+}$ and maximum V_{OC} limit.

dynamics remains integral to enhancing DSSC performance. In Fig. 7 are reported the potential diagram for I_3^-/I^-, $[Co(bpy)]^{3+/2+}$ and $[Cu(tmby)_2]^{2+/+}$.

Concurrent with the rise of bifacial DSSCs is the promising exploration into iodine-free redox pairs, a research direction showing great potential to boost stability and reduce the overall expense of DSSCs. Copper and cobalt-based redox couples, showcasing both advantageous electrochemical characteristics and robustness, are promising contenders to replace iodine. In Table 3, we summarize the main outstanding PV performances of DSSC reporting the utilized dye and electrolyte.

3.4 Working electrode (WE)

After 30 years of study, the most efficient utilized wide band gap semiconductor in a DSSC WE is TiO_2,[170] in anatase phase, with nanocrystalline nanoparticles at high porosity. Titanium oxide is white, insoluble in water and, as a dye, finds a wide range of application in paintings, sun-creme, food colouring. Early investigations focused on the optimization of the TiO_2 layer in terms of particle sizes, film porosity, $TiCl_4$ treatment,[53] thickness, doping[171,172] and introduction of a reflecting layer with the aim of scattering light (SL).[53] However, some properties of TiO_2 are not ideal.[173] With a band gap of 3.2 eV, TiO_2 anatase absorbs to wavelengths below 390 nm, generating highly reactive holes that can induce destructive oxidation reactions with organic components of DSSCs. To counteract these detrimental effects and ensure long-term stability under full sunlight exposure, UV filters are commonly employed in DSSC device studies. Additionally, incorporating an ultrathin layer of Al_2O_3 or MgO can effectively minimize the photocatalytic action of TiO_2.[174]

Employing a mesoporous semiconductor with a wider bandgap offers distinct benefits. SnO_2, with a bandgap of 3.6 eV, absorbs less UV light from the solar spectrum compared to TiO_2. While SnO_2 has been successfully implemented in DSSCs, its conduction band lies approximately 0.5 V more positive than that of TiO_2, hindering its performance due to reduced voltage output. Coating SnO_2 with an ultrathin metal oxide layer, such as ZnO, Al_2O_3, or MgO, significantly enhances the voltage output.[174,175] ZnO has been extensively investigated as a nanostructured electrode in DSSC devices, with a wide range of morphologies explored.[176] Despite purported advantages in electron transport properties, ZnO has not demonstrated superior performance compared to traditional mesoporous TiO_2 electrodes. This is attributed to electron transport not being a limiting factor for DSSCs under operational conditions (at the maximum power point).[173] While other metal oxides can serve as mesoporous electrodes in DSSC devices, their performance generally lags behind that of TiO_2 counterparts.

In BFDSCs, that absorb light from both front and rear sides, additional factors must be considered in TiO_2 photoanode design to maintain transparency while ensuring adequate electron transport.

The TiO_2 film thickness is a critical component that impacts DSSC parameters. An increase in TiO_2 thickness results in a loss of internal resistances at the TiO_2/dye/electrolyte interface; consequently, the electron lifetime enhances, leading to improved electron diffusion and transport, and therefore overall PCE growth. On the contrary, exceeding TiO_2 thickness causes electronic recombination that negatively interferes with DSSC performance. The TiO_2 paste contains mostly 15–20 nm nanoparticles, and a precise formulation is needed when high PCE and transmittance are required. With a few microns of semiconductor layer, 75–80% light transmittance is attained in the visible spectrum.[177] In an early work of Tagliaferri *et al.*,[177] it is evident how the TiO_2 thickness and the immersion time impacts in the colour tonality therefore on the transmittance of the photoanode (Fig. 8a). However, when the TiO_2 thickness and the dye loading increase, light transmission decreases, according to Lambert–Beer law, whilst the efficiency of the corresponding cells rises. On the other hand, a strong dependence on the dye type was observed.

Dyes with absorption peaks shifted with respect to the eye sensitivity factor of the photopic view's observer (eye responsivity) can perform better in term of transparency *vs.* efficiency. Larger TiO_2 nanoparticles (>100 nm) are typically applied in a diffusive scattering layer, which is an effective collector of solar intensity within the device. When a SL is present in a TiO_2 stack, the photocurrent significantly improves, but a reduction in transparency is evident.[178] In 2008, a pioneering work by Ito *et al.*,[53] authors manage the TiO_2 thickness to meet an optimum between max PCE and BFF reporting a considerable BFF of 91%. The new architecture is based on a mesoporous TiO_2 layer sensitized with a high stable Ru dye (Z907Na) in combination with an ionic-liquid (IL) electrolyte and SiO_2 layer between the electrodes to prevent unwanted back currents. Their device showed a maximum of PCE ~ 6.54% for incident light hitting front or rear surface. Further structure detailed are in Table 2.

Recently, with the use of an organic yellowish dye, Y123, Professor Lee's group[38] aimed to optimize device's parameters such as TiO_2 and platinum thickness and electrolyte composition to develop a BFDSC device.

Concerning the scaffold study, they found 6 μm of main TiO_2 layer (ML) and 4 μm of SL as optimal in terms of efficiency for Y123 dye. The exploitation of a scattering layer is not always suitable for a bifacial device; therefore, they opted for 8 μm of main layer to attain satisfactory results (from the front and rear side) reaching a BFF of 83%.[38]

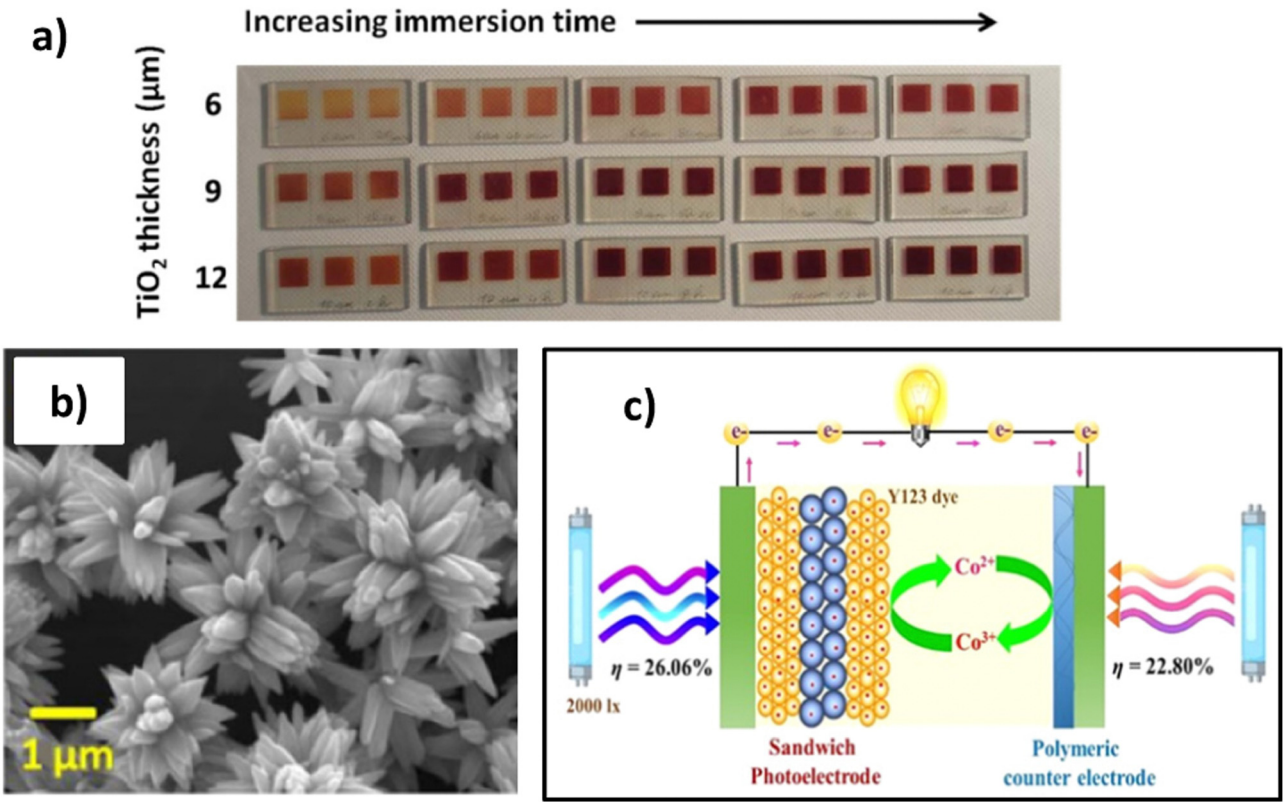

Fig. 8 (A) Comparison of fabricated WE with N719 dye considering the TiO_2 thickness and the immersion time. Reproduced and adapted from ref. 177. (B) SEM image of ZnO micro-flowers applied as SL from ref. 179 under Creative Commons BY-4.0 license (c) sandwich photoelectrode structure realized by ML–SL–ML from ref. 134 Copyright © 2022 American Chemical Society.

However, TiO_2 as semiconductor can be always considered an appropriate material for a BFDSC and the only issue concerns the SL application. As previously reported,[38] a thick SL is not suitable for a BFDSC.

Recently, through a surface engineering of the semiconductor layer, ZnO micro-flowers were added with the aim to scatter the light without harming the AVT[179] (Fig. 8b). The negative shift of the TiO_2-ZF conduction band leads to minor transport time and to mitigate recombination effect. The total BFF reached the 70% value proving the transparency of the ZnO layer. This may be a promising frontier for further application. Moreover, a newly developed sandwich photoelectrode (ML 4 μm-SL 3.5 μm-ML 4 μm) has been utilized for reaching a BFF of 93% under 200 lux with a max PCE of 24.16. This new structure is constructed by introducing an additional ML behind the SL of the traditional DSSC structure (ML/SL), creating a sandwich (ML/SL/ML) architecture of the TiO_2 film (Fig. 8c). Results demonstrate rear illuminated light can be harvested more efficiently by this photoelectrode because the light is first absorbed by the final ML before the SL effect.[134,180]

However, the choice of dye significantly impacts light transmittance, while bifaciality remains unaffected.

3.5 The dye

In this recent work, a Ru complex dark dye, C106, obtained a BFF of 93% when measured in a white background.[144] Dye's choice, as previously discussed, doesn't affect the bifaciality feature while the application in BIPV as façades or indoor smart device may become crucial. The aim is to briefly discuss the three categories of dyes widely used in DSSC while a detailed description can be found here.[49,56]

A sustainable dye for DSSC should possess the following features:

- absorbance properties in the visible spectra and near the IR region;
- a high molar extinction coefficient to harvest the light;
- the LUMO and HOMO level of the dye must match respectively with the conduction band of the semiconductor and with the energy level of the redox mediator;
- a robust bond between the dye and the semiconductor surface facilitates electron transfer.

Indeed, in order to efficiently inject the electron, the LUMO level of the excited dye should be 0.2–0.3 eV above the conduction band of TiO_2 while the HOMO level must lay below the energy level of the redox electrolyte in order to have an efficient dye regeneration.

Anchoring the adsorbing dye molecules onto the surface of semiconducting metal oxide nanoparticles, which collectively form the working electrode of a DSSC, is paramount for initiating an electrical current by injecting electrons from the dye into the conduction band of the metal oxide. Conventionally, carboxylic acid and cyanoacrylic acid groups have been the

mainstay anchors in DSSC research. However, the recent surge in DSSC exploration has ushered in a plethora of novel anchor groups. The molecular structures and optoelectronic properties of a broad variety of DSSC anchors including pyridine, phosphonic acid, tetracyanate, perylene dicarboxylic acid anhydride, 2-hydroxybenzonitrile, 8-hydroxyquinoline, pyridine-*N*-oxide, 3-hydroxy-*N*-methylpyridinuim, catechol, hydroxamate, sulfonic acid, acetylacetanate, boronic acid, nitro, tetrazole, rhodanine, and salicylic acid substituents have been widely discussed in this review.[181] A strategic selection of anchors can bestow upon the solar cell customized performance attributes, including enhanced stability and optimized conversion efficiency.

The dye structure has an important role in their overall performance. A good blocking behavior is crucial for successful use in combination with the novel redox mediators or hole conductors. Steric groups can slow down the electron transfer between TiO_2 and oxidized redox mediator or hole conductor.[173] Co-sensitization is a proven strategy for enhancing the performance of DSSCs. Selecting appropriate dyes with complementary absorption spectra enables the capture of a broader range of sunlight, resulting in strong and panchromatic light absorption. By employing a combination of dyes, co-sensitization can effectively expand the light harvesting window of DSSCs, leading to improved PCE and overall device performance. Moreover, co-sensitization has the beneficial effect of decreasing dye aggregation.[182,183] Dye aggregation is a molecular phenomenon that plays an essential rule in the DSSC photovoltaic performances. The molecular interactions between dye molecules are governed by the chemical structure of the dye, including its polarity and the types of substituents it possesses.[184] The assumption of a uniformly spaced dye monolayer at the dye$\cdots$$TiO_2$ interface may not hold if dye clustering occurs laterally, disrupting the monolayer structure. Additionally, dye aggregation in the longitudinal direction would invalidate the assumption of homogeneous dye distribution. A dye molecule that binds to another dye rather than the TiO_2 surface would render itself non-photovoltaic since it cannot interact with the TiO_2 surface for electron injection and also obstructs electrolyte ions from reaching and regenerating the cognate dye on the TiO_2 surface. Furthermore, a dye molecule that binds too close to another dye molecule on the TiO_2 surface may experience dye$\cdots$dye interactions that could positively or negatively impact their charge characteristics. The molecular factors that cause dye aggregation, and ways by which dye aggregation can be suppressed are deeply discussed in this review.[184] An interesting approach is to use dyes with different binding groups that do not compete for the same binding sites on TiO_2. Shibayama *et al.* successfully combined the black dye (with carboxylic acid binding groups) with an organic dye possessing a pyridine binding group.[185] They demonstrated that the dyes adsorbed to different binding sites.

Ru-based dyes. The firstly studied category of dye is the inorganic Ru-based. Ru-based dyes possess an octahedral structure that tolerates extension of specific ligands in controlled manner therefore photophysical, photochemical and electrochemical properties can be modified. Moreover, they show a good solubility in several solvents. N719,[113,177] N3,[35,104] C106,[144] Z907[89] are some dyes of this category. Carboxylate polypyridyl Ru dyes, phosphonate Ru dyes, and polynuclear bipyridyl Ru dyes are three subclasses of this dye class. The distinction between the first two subclasses lies in the absorption groups, while the latter subclass differs from the first two due to the number of metal centres in the structure.

Organic dyes. After 10 years from DSSC invention, research was devoted to proving the development of a new kind of metal-free organic dyes. Metal free organic dyes showed several promising features such as facile synthesis and tunable absorption energy levels, low cost and stability under elevated temperature and prolonged illumination. D35,[156,157] Y123,[38,134] MS5,[14] XY1[132] are some dyes of this category. Many successful organic dyes have a donor–pi–acceptor (DpA) structure, which leads to electron density movement toward the acceptor part upon photoexcitation. Typically, the binding group is incorporated in the acceptor part, as in the case of cyanoacrylic acid.[173]

Natural dyes. Nature provides a diverse array of pigments for various purposes, including chlorophyll-*a*, the primary photosynthetic pigment in plants, chlorophyll-*c*,[186] found exclusively in seagrasses to capture light underwater, antioxidants[187] molecules in flowers and fruits for protection, and pigments to attract pollinators. The natural environment is full of resource that researchers tried to untangle and exploit in the favourable PV field of DSSC. Natural based dye showed PCE far away from the reference ones but the priceless values to obtain a natural dye application is still worth of investigation. Natural dyes are indeed environmentally friendly, abundant, economic and safe. The precise extraction of Chl-*c* pigment by column chromatography leads to one of the highest PCE for natural dyes, 4%, indeed, Chl-*c* in comparison to Chl-*a* has proper ligands (–COOH) to anchor in the TiO_2 surface.[188] Recently, a new PCE record of 8% has been reached with a dye's cocktail with pigments from *P. pterocarpum* and *A. amentacea* plants.[189]

NIR dyes. NIR dye is an intriguing material for applications involving semi-transparent materials. The development of efficient colourless NIR-DSSC relies on the design of specific transparent materials with tailored properties.

There are three classes of possible NIR sensitizers: polymethines, phthalocyanines and porphyrins. The NIR dyes and their performances are described in detail in this review[56] while, in this section, we will mention the main characteristic of each class and the best obtained performances.

Polymethines are a class of dyes initially investigated for silver halide photography and as probes for biological systems[190,191] when integrated with other high band gap semiconductor materials. They possess a high molar extinction coefficient and are extremely versatile: the central heart, the length of the numerous conjugated chains and the nature of the side groups are easily modifiable. The latter concludes that shifting the transition level from s0 to s1, therefore from the visible to the NIR region, is possible. Self-aggregation is a negative aspect of this class of dye that is limiting both the efficiency and the transparency; this can be solved with the addition of a disaggregating agent, chenodeoxycholic acid (CDCA) or with the introduction of a lateral bulky unit or alkaline chains.[184] VG10 is a molecular engineered

near-IR squaraine sensitizers, containing the novel benzoindolenine moiety functionalized with COOH as an efficient attaching group. This blue dye shows panchromatic light harvesting in the range between 400 to 800 nm and it detects the record PCE of 6.2% that is an outstanding value for this class of dye considering the easy and efficient low-cost synthesis process.[192] Recently, a polymethine cyanine structure (VG20-Cx) has been proposed[18] to render DSSCs fully transparent and colorless. The selective NIR-DSSC can display 3.1% PCE and a value approaching the 78% AVT reaching a CRI of 92.1.

Phthalocyanines are 2D tetrapyrrole macroheterocycles with 18 delocalized p-electrons. Their optical and electronic properties can be tailored through structural engineering, enabling absorption extending into the NIR region. They possess a high molar extinction coefficient, chemical and thermal stability.[193,194] These also show a tendency to aggregate and poor solubility. Currently, the highest PCE is 6.4% given by PcS20.[195]

Porphyrins (Pors) are tetrapyrrolic macroheterocycle containing 18 delocalized p-electrons, synthetic analogues of Pcs. Pors have a high molar extinction coefficient and absorb in the visible spectrum but with appropriate structural engineering modifications, many porphyrins can extend the absorption spectrum up to the NIR region. Chemical and thermal stability are shown, and aggregation is lower if compared to PCs. The highest reported PCE for this class of dyes is 13%,[85] one of the highest detected for DSSCs. The latest result was possible thanks to the introduction of the proquinoidal benzo thia-diazole (BTD) unit directly connected to one *meso* position, and a donor amine N-linked to the macrocycle on the other *meso* side. This led to the creation of the SM315 dye, with the push and pull porphyrin structure. By extending the ability to absorb light from the limit of 600 to the limit of 800 nm SM315 reaches high IPCE values across the whole visible wavelength range.

Photocromic dyes. Photochromic dyes have recently emerged as a game-changer in the design of versatile multifunctional DSSCs.[196] While photochromic dyes have long been explored for their optical response to light in applications like data storage,[197] actuators,[198] sensing,[199] optical lenses,[200] and bio-imaging,[201] their potential in photovoltaics has only recently been investigated. A photochromic dye with a donor-π-conjugated-bridge-acceptor structure where the π-conjugated bridge is substituted by a diphenyl-naphthopyran photochromic unit has been reported with a successful application in DSSC.[196]

These DSSCs exhibit a reversible colour change and self-adjustable light transmittance upon irradiation, achieving a PCE of up to 4.17%.

By employing the well-established donor-π-conjugated-bridge-acceptor architecture for the dyes, where the π-conjugated bridge is substituted with a photochromic moiety, researchers have successfully developed DSSCs that can alter their colour and dynamically adjust their light transmittance upon exposure to sunlight (Fig. 9a). Exploring this concept, Fauvel *et al.*[202] proposed that the replacement of the diphenyl-amine group with modified carbazole units allows for the tuning of the dye's optical properties to better match the photopic response of the human eye. The incorporation of carbazole units enables the lowering of the HOMO energy level of the dyes, thereby expanding the range of compatible redox systems beyond tri-iodide/iodide-based electrolytes. Some of the dyes show a maximum PCE of about 3% in opaque cells and 2.3% in transparent devices while an outstanding AVT above 50% and a CRI of 95 have been obtained (Fig. 9b).

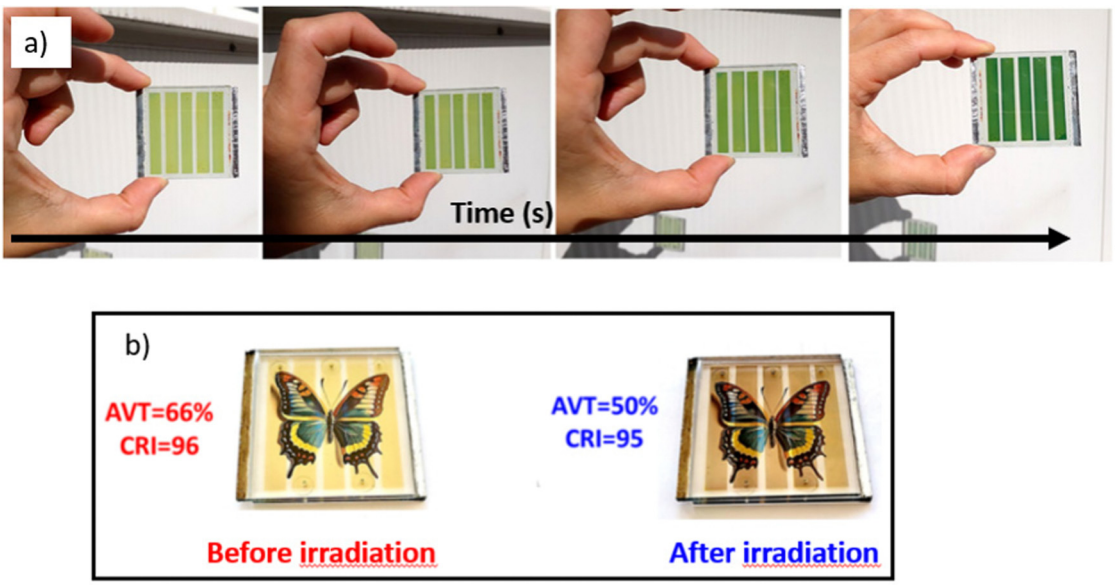

Fig. 9 Colour change of a semi-transparent NPI-based mini-module under natural light. Evolution of the colour of an NPI-based solar semi-transparent mini-module when exposed to natural light at 20 °C. Interval times between pictures (from left to right) of 30, 30 and 240 s cumulatively (modified image from ref. 196). (b) Picture of a colored butterfly taken through the mini-module (total area: 23 cm^2) in the non-activated state (top) and activated state (bottom). It is reported the obtained AVT and CRI values with the use of a photocromic dye (modified image from ref. 202).

4. Application

In the following sections, we discuss the applications of BFDSC, with a focus on BIPV, agrivoltaic and IoT.

4.1 BIPV

In Europe, electricity usage in buildings will surge at a rate five times faster than the growth of natural gas consumption by 2050 due to the implementation of short-term policies aimed at curtailing the import of natural gas from Russia.[203] From the last BIPV market analysis, the global building-integrated photovoltaics market was valued at USD 19 billion in 2022 and is projected to reach a staggering USD 143.99 billion by 2032.[204] While PV modules integrated into building envelopes can serve as multifunctional components, fulfilling roles like heat insulation, noise reduction, privacy enhancement, and weather protection, BIPV systems are primarily installed to generate electricity on-site, with minimal impact on the building's standard functionalities.[205] BIPV windows are required to provide natural light while controlling solar heat in one system. Accordingly, PV devices must have a minimum transparency of 25–38%[61] to be installed as tiles, modules, and solar glazing products.

BIPV windows can be developed in two types: spacing non-transparent solar cell to achieve transparency or the use of transparent devices as window.[206] Among PV technologies, c-Si has poor building integration in respect to the transparency requirement. The mutual distance between the cells can be settled to mimic semi-transparency but the pattern produces shades not comfortable for the internal living;[61,207,208] c-Si can guarantee daylighting by distributing the cells but affecting the natural viewing.[209] Besides, tilt angle and low irradiation levels complicate their integration in architectural glazing. In the last years, the new PV technologies like hydrogenated a-Si,[210] CIGS, organic[211] and perovskite solar cells have been considered as good candidates for BIPVs applications. Currently, BIPV systems are considered to have a lifespan of 25–30 years.

BFDSCs, as discussed before, have peculiar and promising features for BIPV applications. The transition between small laboratory scale and industry (such as BIPV application) implies the development of modules and panels. Most of the manufacturing steps for modules, such as the deposition of semiconductors and catalyzer, can be adopted from already developed techniques and methods in other industrial sectors.[212] However, only the electrolyte injection and sealing have to be optimized for this purpose. From laboratories cell (<1 cm^2) to modules the layout optimization is crucial. Dye sensitized solar modules (DSSMs) are made with a number of interconnected cells stripes on the same substrate which can be either connected in parallel (currents of the cells are summed) or series (voltages of the cells are summed). In this book chapter,[213] a detailed explanation of parallel connection, series monolithic, series W-type connection and series Z-type connection DSSMs is present. Despite the type of connection used, a good sealing is decisive for guarantee a life span of more than 5 years.

From the beginning of the century, some works evaluated DSSC glazing performance in real outdoor condition. Lee *et al.*[206] tested DSSM, by a Korean company, applied to a full-scale mock-up facility to verify the power performance of transparent DSSC BIPV glazing over a 2 year period (Fig. 10). Four and two DSSC BIPV windows were installed on the vertical south wall and on the 30° sloped roof, respectively. Over the two-year study period, the average daily power yield for the vertical DSSC BIPV window varied between 1.75 and 3.93 kWh per kWp per day, with an average of 2.53 kWh per kWp per day. In contrast, the average daily power yield for the 30-degree sloped DSSC BIPV window ranged from 2.16 to 5.34 kWh per kWp per day, averaging 3.60 kWh per kWp per day. However, DSSM demonstrates lower power efficiency compared to a-Si, c-Si, or CIGS, necessitating enhanced installation for equivalent power generation.

Kim *et al.*[214] realized a large-area Z-type transparent DSSM of 900 cm^2 for producing DSSC-based BIPV windows. Authors utilized a thin layer of TiO_2 (4–5 μm), Z907 dye, a standard iodine-based electrolyte and, as counter electrode, a Pt layer. The module reached 3.19% of PCE but no AVT value is reported.

Godfroy *et al.*,[215] with the aim to realize semi-transparent DSSC devices, focus on the synthesis and structure–properties relationships of benzothiadiazole-based organic dyes. Authors selected the YKP-88 dye for its superior performance and stability in laboratory testing and compared it against the reference N719 dye in a W-type series-connected module of 14.08 cm^2 active area. In order to achieve an acceptable degree of semi-transparency in the visible spectrum, the thickness of the titania electrode was maintained at 7–8 μm without the use of a scattering layer. While YKP-88 dye exhibited a higher PCE of 8.7% compared to N719 dye's 6.3%, it was N719 dye that demonstrated a higher AVT of 34% compared to YKP-88's 26%.

Fig. 10 DSSC BIPV mock-up. Reproduced from ref. 206. Copyright Clearance Center's RightsLink®.

In the last decade, first installation prototypes on buildings are reported. In 2014, Solaronix installed 300 m^2 of W-connected modules (35 × 50 cm^2 size for each) on Swiss Tech Convention Center façade at EPFL campus (Fig. 11a).[170]

Established in Italy, the dyepower consortium made significant strides in 2015, achieving a PCE of 5.6% on a Z-connected 600 cm^2 device fabricated within their pilot line facility.[216] These devices demonstrated remarkable resilience, successfully passing the stringent UV preconditioning test, humidity freeze test, and damp heat test outlined in the IEC 61646 Standard. Additionally, a comprehensive assessment of the environmental footprint of semi-transparent DSSCs, was conducted demonstrating their potential as a sustainable energy solution.[217] H. Glass realized a huge DSSC installations on Science Tower in Austria (Fig. 11b) consisting of 896 W-connected red DSSC devices of 0.6 m^2 area each (in total approx. 500 m^2) while Dongjin Semichem realized a DSSC installation at the Solar Pavillon at Roskilde University in Denmark, consisting of 196 W-connected red DSSC panels of area 900 cm^2 each (in total approx. 180 m^2).[170]

Recently, Vesce *et al.*[218] demonstrated a reliable, reproducible and industrially compatible method to fabricate under ambient air conditions large-area DSSM (400 cm^2) and dye sensitized solar panel (DSSP) (0.2 m^2) containing an organic inhouse made dye. The finest module efficiency was more than 5%, AVT is 35.7% (higher than any previous reported semi-transparent DSSM), LUE is above 1.8% and the modules are stable in temperature (ISOS-D-2 test) and under light soaking (ISOS-L-1 test)[219] for more than 1000 h.

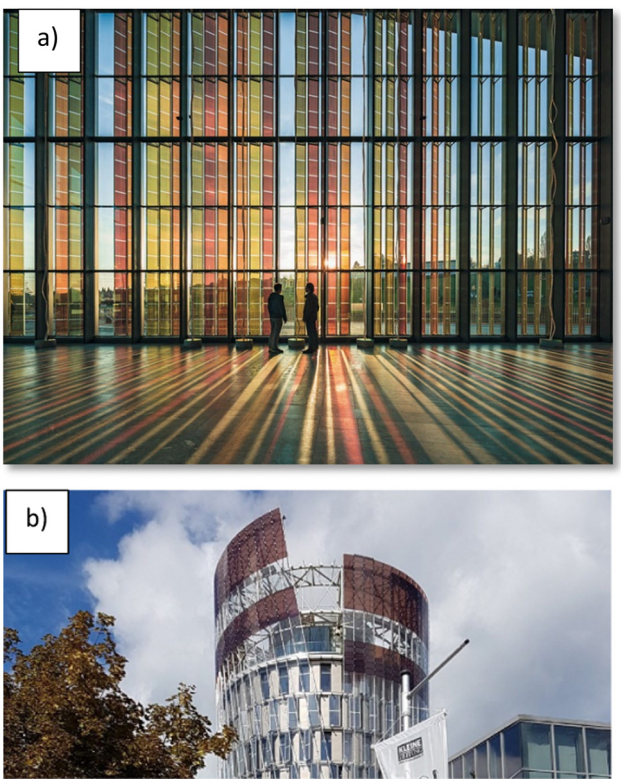

Fig. 11 (a) DSSC installation by Solaronix at center façade at EPFL campus. https://www.epfl.ch/labs/lpi/index-html/photo-gallery-and-industrial-applications/. (b) DSSC installations on Science Tower in Austria by H. Glass. Reproduced with permission from H.Glass S.A., copyright 2023.

Interestingly, Roy *et al.*[220] characterized and analyzed the color and semi-transparent properties of a N719-based DSSC using CRI and CCT values after two years of ambient exposure. They tested three different TiO_2 thicknesses: 3.5, 6, and 10 μm. The study on the DSSC glazing after ambient exposure revealed a decrease in AVT over two years, while there was an improvement in color properties (CRI and CCT). This suggests that both CCT and CRI are spectrally dependent parameters. The authors concluded that the thinnest TiO_2 layer, which experienced a 30% increase in CRI and only a 11.4% decrease in AVT, is the most suitable for DSSC integration in warmer seasons and hot climates.

4.2 Agrivoltaic

With the current energy and environmental crisis, soil preservation is of utmost importance. Indiscriminate deforestation to make room for photovoltaic installations is not the optimal choice in a world desperately in need of oxygen, which only plants can provide. The coined terminology Agrivoltaic expresses the struggle to combine the intended land for crops production with the supply of clean energy through panels. In just eight years, the global installed agrivoltaic capacity has rapidly reached 2900 MW in 2020 starting from 5 MW in 2012.[221]

Commercial greenhouses interior conditions, as lighting, heating, cooling and ventilation for maximum yield require a significant energy consumption leading to unsuitable cultivated products. Several facilities such as fans, window-opening motors, artificial lighting, irrigation and automation equipment need electricity power. PV panels can support an electricity demand in greenhouses.

Generally, a greenhouse is made of transparent plastic or glass, therefore the PV integration on the roof or façades may compete with plants for lights, resulting in negative effects on crop growth.

The so-called photosynthetically active region (PAR) of plants is between 400 and 750 nm but not all the radiation is efficiently converted for the entire PAR wavelengths. The most common photosynthetic pigments are chlorophyll-*a* and chlorophyll-*b*, which absorb light mainly in two regions of the visible spectrum with two high peaks around 425–475 nm and 625–750 nm.

Commercially available silicon-based solar modules were tested concluding that the covered area of the greenhouse roofs should not exceed the 20–30% of the total roof area.[222] Si-based modules are opaque and inhibit plant growth and productivity through excessive shading. Recently, Alinejad *et al.*[223] investigated on PV application in a rose greenhouse assessing different parameters such as temperature, relative humidity, natural gas consumption, electricity consumption, and carbon dioxide (CO_2) emission reduction. They identified an optimum PV coverage of 19.2% on the roof, resulting in no significant change in the illumination level on the plant canopy. Moreover, they demonstrated an annual reduction of natural gas consumption, electricity demand, and CO_2 emission by 3.57%,

45.5%, and 30.56 kg m^{-2} respectively. In earlier research, Ureña-Sánchez[224] tested two sides of a greenhouse with 10% roof coverage and compared different parameters especially the crop growth, to a conventional side of the greenhouse. Due to 9.8% radiation blocking caused by the solar panel, a small reduction in the transmitted light through the polythene cover was detected but this did not affect marketable production. While the largest tomatoes were obtained under conventional greenhouse conditions, notable distinctions in mean fruit mass and diameter were observed for fruits grown under the PV panel-covered greenhouse. However, these smaller fruits did not influence the final price. Similarly, Kavga *et al.*[225] tested a roof coverage of 12.4% to compare the growth of lettuce (*Lactuca sativa* L.) and rocket (*Eruca sativa* Mill.) under polycrystalline silicon (pc-Si) panel shading *versus* an unshaded control. PV installations caused a favorable temperature reduction of 2.2 and 2.9 °C when temperatures reached peak levels during the spring and summer seasons, consequently resulting in energy and money savings for greenhouse temperature control. For plant growth, the PV presence reduced the PAR by 7.2% and 10.5% for lattice and rocket respectively. The most crucial commercial crop attribute (plant and stem fresh weight and the number of mature leaves) was unaffected under the PV greenhouse for lettuce, whose ability to adapt to varying solar radiation environments is well documented. However, all rocket salad growth characteristics appeared diminished under PV conditions compared to the unshaded control.

OPV shows interesting properties such as transparency and flexibility, enabling use in transparent façades or roofs. Zisisa *et al.*[226] conducted an experimental study integrating semi-transparent OPVs based on a blend of regular poly(3-hexylthiophene) (P3HT) and phenyl-C61-butyric acid methyl ester (PCBM) on the rooftop of a Mediterranean greenhouse, covering 22%. The optical transmittance of the manufactured OPVs is around 18–20% in the PAR region. They cleverly tested pepper plants, which thrive in partial shade rather than direct sunlight. By absorbing ultraviolet radiation, the OPV materials favoured the shaded plants, enabling them to build longer central stems and produce more fruit, yielding increased mass of horticultural products. Ultimately, the cultivated plants under OPV shading showed better performance.

Several research groups are focusing on DSSC application in greenhouse environments, but there are few real-life tests. A prominent research direction involves manipulating absorbed light through spectral engineering to mitigate transmittance. In a pioneering work, Ru-based JJ-7 and JJ-9 sensitizers were proposed as efficient DSSC sensitizers for greenhouses. JJ-7 and JJ-9 dyes show a transmittance of 62.0% and 61.0% at 660 nm, and 18.0% and 15.0% at 440 nm, respectively, when deposited on 5 μm-thick TiO_2 films.[227]

Recently, researchers have aimed to develop metal-free organic dyes for economic and environmental reasons. Dessi *et al.* proposed D–A–π–A dyes for greenhouse application. First, the organic thiazolo dye TTZ8–12, with a push–pull D–π–A structure, improved light absorption in the green visible range while maintaining ~25–40% transmittance in the blue (425–475 nm) and 83% transmittance in the red (625 nm), achieving ~6% efficiency in small-area devices with 5 μm[228] TiO_2. Efficiency then reached 8% by adding an extra acceptor between the donor and π spacer.[229]

Another spectral engineering approach was contemplated Chalkias *et al.*[230] proposing new low-cost triphenylamine dyes and a highly transparent I_2-free redox mediator as an alternative to the yellowish I_2 electrolyte. TPA dyes mainly absorb in the blue, providing high red transparency. A key contribution was using an I_2^- free electrolyte that maintained device efficiency while improving current density by avoiding competition with the dye for blue light absorption. They reported a maximum 6.1% efficiency with the semi-transparent combination (TPA-1 and I_2-free electrolyte) and crop growth factor G of almost 35%, claiming the best combined agrivoltaic performance known at the time.

The crop growth factor G (eqn (10)) was conceived by Emmot's group[231] to assess the impact of transparent solar cells on plant growth:

$$G = \left(\int T(x,\lambda)\mathrm{bs}(\lambda)a(\lambda)\mathrm{d}\lambda\right) \Big/ \left(\left(\int \mathrm{bs}(\lambda)a(\lambda)\mathrm{d}\lambda\right)\right) \qquad (10)$$

where $T(x,\lambda)$ is the total transmission of the full solar cell stack, influenced by the active layer thickness x; $\mathrm{bs}(\lambda)$ is the photon flux density and $a(\lambda)$ considers the plant action spectrum. This metric is not commonly employed but is highly recommended for direct and transparent comparisons of diverse technologies and performance levels of translucent PVs. Another pivotal step for DSSC commercialization and real-life greenhouse application is scaling up fabrication from lab scale (<1 cm^2) to market scale (>10 cm^2). Maintaining high efficiency over large area is challenging given complex resistance phenomena. Moreover, high stability of device components and structure is required for real-world use. On this purpose, Barichello *et al.*[17] developed 2 m^2 of PV panels for aquaponic greenhouses. The robust Z-type DSSC module design remained stable for 1000 hours at high temperature (85 °C) and under illumination accordingly with stability test protocols: ISOS-D-2 and ISOS-L-1.[219] The purpose is DSSM application inside an Aquaponic greenhouse, above the crop to filter light (Fig. 12a and b). Using a commercial D35 orange dye and 5 μm semiconductor, researchers achieved 4% efficiency over 221 cm^2 active area with 35% of AVT for the complete device.[17] Finally, inkjet-printed Z-type DSSC modules were tested as a novel glass façade in a hydroponic greenhouse[232] prototype. The growth of tomatoes was compared in a smart greenhouse and a standard greenhouse without DSSCs. Modules were fabricated with a D719 dye and 3 μm TiO_2 for transparency. Encouraging results were achieved: pesticide use was reduced due to UV blocking, which diminished insect and fungal infestations. No significant differences in tomato growth were observed between the greenhouses; however, the smart greenhouse demonstrated a 25% reduction in energy costs.

Roslan's group constructed a portable dye-sensitized solar cell mini green house (PDMG) with commercial DSSC panels by Solaronix (Fig. 12c), comparing growth of Misai Kucing, an anti-inflammatory/anti-gout tea plant, to a standard greenhouse. DSSC

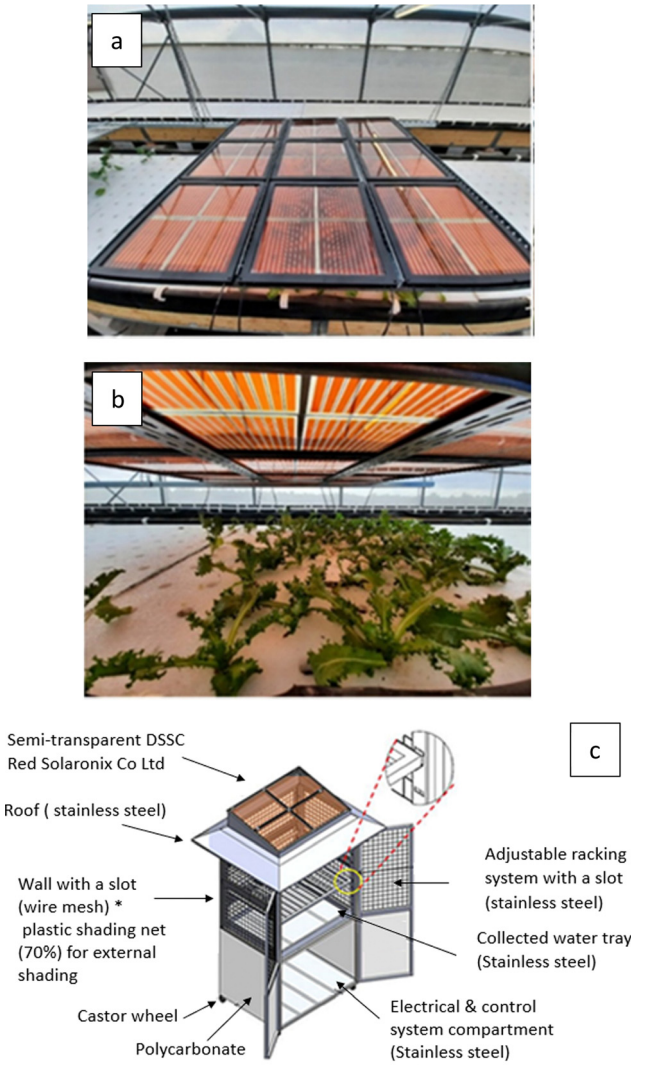

Fig. 12 (a) and (b) DSSM application in an Aquaponic greenhouse.[17] (c) The detailed construction drawings of PDMG prototype. Reproduced with permission ref. 233 Elsevier.

shading beneficially lowered heat and increased mid-day humidity. Misai Kucing grew equally well in the PDMG and control.[233]

4.3 Internet of things

The field of photovoltaics provides opportunity to make our buildings ''smart'' and our portable devices ''independent''. Moreover, effective energy sources can be developed for ambient indoor use.[77] To address this, ambient light photovoltaic cells have been developed to power autonomous IoT devices[9] capable of machine learning, enabling on-device artificial intelligence[234] implementation. IoT is a promising DSSC application area, though bifaciality is not mandatory.

The Internet of Things consists of connected physical objects and sites with digital identities that communicate to provide automation services. It is estimated 75 billion IoT devices will be part of daily life in 2025, assisting in.[9,235] This extends beyond current internet-connected devices like smartphones, desktops, tablets and laptops to unsupported appliances like air conditioners, coffee makers, and washing machines, plus environmental sensors. The cloud infrastructure is the IoT platform where devices communicate; wireless networking technologies include Wi-Fi, Bluetooth, LPWAN, cellular, and Ethernet. Most IoT devices require low, continuous power. Indoor PV technologies, especially DSSCs with high indoor performance, are a perfect match to supply this market. Lux refers to indoor light intensity based on the human eye response spectrum. DSSCs efficiently operate over a wide range from dim 50 lux to bright 1000 lux. Freitag *et al.* showed under 1000 lux DSSCs exceed conventional Si and GaAs PV thin films with remarkable 28.9% efficiency.[234] Cao *et al.* improved the PCE to 32% under 1000 lux. Using a dye cocktail composed of Y123 and XY1b, along with a Cu(II)/Cu(I) redox-based electrolyte, the device benefits from the use of PEDOT as the counter electrode. This choice reduces the diffusion path of the redox mediator to only the mesoporous TiO_2 film, thereby attenuating the Warburg resistance and boosting the photovoltaic performance. The authors claim promising applications in the IoT domain.[166] Sensing fading of natural dyes *via* IoT and refilling to restore efficiency was suggested. Butein and isobutrin from Butea monosperma were extracted as sensitizers. When the natural dye faded, it was refilled, restoring (even improving) initial performance. The authors proposed IoT sensing of dye fading beyond a critical value, triggering refill from a reservoir.[236]

Researchers have developed a prototype of a fully self-powered intelligent IoT node that can infer information based on a pre-trained artificial neural network (Fig. 13). The node, which is based on an ATmega328P microcontroller, is powered by five 3.2 cm^2 XY1:L1-sensitized solar cells (total 16 cm^2) illuminated with 1000 lux fluorescent light. DSSCs utilizing XY1 and L1 dyes maintain an impressive photovoltage of over 910 mV under 1000 lux of fluorescent illumination, translating into remarkable conversion efficiencies of 34.0%, 32.7%, and 31.4% at 1000, 500, and 200 lux, respectively. The cells generate enough energy to power the node's microcontroller, sensors, and wireless communication circuitry.[9]

Established companies such as RICOH and EXEGER have introduced DSSCs to the market, using them in a variety of IoT applications, including wearable electronics and smart sensors.

Ricoh[237] launched solid-state DSSC-powered devices supporting the IoT era, eliminating battery replacement and waste while generating clean, sustainable energy.

Applications include sensors for temperature, humidity, illumination, pressure, and optical sensing or remote controllers moreover a DSSC-integrated desk that can recharge a detachable mobile battery under the desktop. Exeger,[238] a Swedish company, upgraded through a superior design capability, the best of existing DSSC advancing in the flexibility and the PCE. Powerfoyle™ is thin (1.3 mm), flexible, durable and can look like steel, leather or carbon fiber. They spread this PV DSSC based material to a wider range of consumers electronics and IoT devices.

5. Bifacial enabling technologies

Next-generation solar cells adhere to the trend of integrating multiple energy device types into single, consolidated systems.

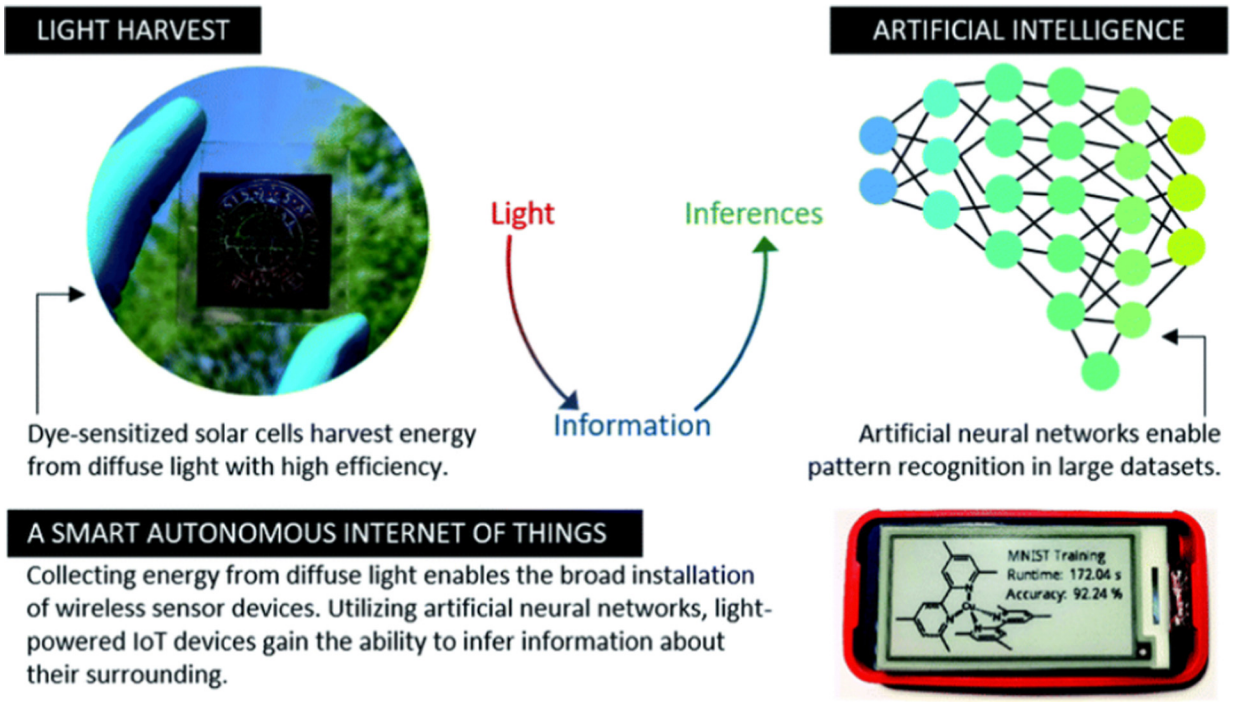

Fig. 13 Fully autonomous IoT devices powered by harvested ambient light directly convert photons into computational information. Reproduced with permission of ref. 9 (Licensed Under a Creative Commons Attribution 3.0 Unposter Licence).

Single-junction (SJ) PV cells, however, exhibit significant energy losses due to the thermalization of high-energy photons and the inability to capture transmitted low-energy photons. This phenomenon leads to the Shockley–Queisser (S–Q) limit, which represents the theoretical maximum efficiency. For single-junction silicon solar cells, which are commonly fabricated using silicon with a bandgap of 1.1 eV, the Shockley–Queisser (S–Q) limit is approximately 32%. Last record PCE of single junction crystalline silicon solar cell reached the 26%[16] due to internal parasitic effect and light reflection. Tandem technology appears a promising strategy to overcome the S–Q limit. The purpose of a tandem device is extending, by integrating more PV cells, the light absorption range, limiting the loss of photons. Tandem solar cells can be divided in two categories: 4-terminal (4-T) tandems mechanically stack two different devices, while 2-terminal (2-T) monolithic structures directly fabricate the top cell on the bottom (Fig. 14). Conventional series-connected 2-T tandems offer advantages such as fewer fabrication steps, resulting in reduced manufacturing costs and energy consumption, and fewer parasitic light effects due to fewer layers. However, paying attention to the choice of the material and the chosen processes is mandatory. For example, the manufacturing processes of the top cell must not deteriorate the bottom one with high temperature or pressure. In contrast, 4-T structures avoid these limitations but suffer optical losses from interlayer materials.

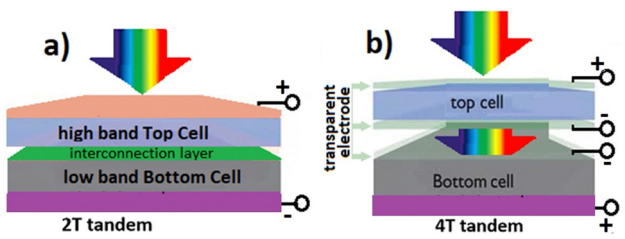

Fig. 14 Schematic example of (a) 2T tandem and (b) 4T tandem.

In 2T tandem solar cells, two sub-cells (top and bottom) are connected in series. Each sub-cell selectively absorbs a specific portion of the solar spectrum, maximizing energy conversion efficiency. The top sub-cell, featuring a wider bandgap, effectively captures and converts high-energy photons associated with shorter wavelengths, such as ultraviolet and visible light. This allows lower-energy photons, characterized by longer wavelengths like infrared radiation, to pass through and reach the bottom sub cell. The bottom sub-cell, equipped with a narrower bandgap, efficiently absorbs and converts these lower-energy photons. However, the series connection means current through both cells must be equal, which can limit efficiency if the currents are mismatched.

In 4T tandem solar cell, top and bottom cells operate independently, each with separate terminals, eliminating the current-matching requirement and allowing maximum power point operation. As in 2T cells, the top cell has a larger bandgap, converting high-energy photons, while allowing lower energy photons to reach the bottom cell with a lower bandgap. Both 2T and 4T designs employ a wider range of the solar spectrum, resulting in enhanced efficiency compared to single-junction cells. The selection of materials is influenced by factors such as material compatibility, fabrication complexity, and the balance between efficiency and

cost. Solar cells are typically connected in series to achieve higher voltage output. Photocurrent matching is crucial to minimize performance losses and ensure optimal efficiency.

At present, the world record power conversion efficiency (PCE) for a multi-junction solar cell stands above 39%.[16,239] Since the advent of DSSCs, integration with materials like Si, GaAs, and perovskite has targeted energy harvesting, conversion and storage.[240,241] As semi-transparent cells with tunable light filtering *via* dye selection, DSSCs are strong tandem candidates. Here we discuss results based on materials used.

5.1 Tandem DSSC (T-DSSC)

In early work,[242] a T-DSSC achieved 1.45 V and over 10% efficiency. N719 was utilized as the top sensitizer over NKX2677 due to its high molar extinction coefficient, ensuring sufficient light reaches the bottom cell. Black dye absorbed 600–800 nm in the bottom cell. Thickness optimization involved employing a thinner 6.5 μm TiO_2 layer for the top sub-cell and a 34 μm layer for the bottom sub-cell. Subsequently, the Sewaga group utilized a Ru(II) DX1 sensitizer with strong absorption in the 320 nm UV and 500–900 nm ranges as the bottom dye in combination with N719 as the top dye, achieving an impressive 11.4% efficiency. Barawal *et al.*[243] developed a TCO-less T-DSSC, with photons crossing just one TCO substrate before the bottom electrode, using a flexible metal mesh to replace one TCO. To achieve current matching, TiO_2 layers with thicknesses of 1 and 16 μm were employed in conjunction with D131 and N719 dyes. Thinner TiO_2 improves top cell transparency. Eom *et al.*[244] synthesized SGT-136 and SGT-137 D–π–A sensitizers to improve SGT-130's π-bridge. A parallel-connected tandem device employing an SGT-137 top cell and an SGT-021 bottom cell achieved a remarkable current density of 22.06 mA cm^{-2} and an efficiency of 14.64%, representing one of the highest PCE values reported for T-DSSCs. Recently, a T-DSSC exceeded 33%[245] dim-light efficiency using the Y123 dye in both cells with a $Co^{2+/3+}$ electrolyte, which avoids iodine light absorption limiting photon transmission.

In the last year, Mounika *et al.*[246] demonstrated the integration of an LG6 dye sensitizer for near-infrared light utilization and an N719 dye sensitizer for effective visible light capture in the bifacial tandem cell design. The bifacial tandem DSSC–DSSC was fabricated by sandwiching two photoelectrodes (PE) (N719 dye-anchored PE and LG6 dye-anchored PE) between one common counter electrode (Fig. 15). The T-DSSC exhibits a high PCE of 12.76% with a current density of 27.61 mA cm^{-2}.

In a similar vein, Gianola *et al.*[247] introduced the Hole Tandem Bifacial configuration (HTB-DSSC), a two-compartment cell design that incorporates a bifacial semi-transparent shared counter electrode (Pt-based) between two identical semi-transparent photoanodes. Using common N719 dye and I-based electrolyte, the HTB-DSSC achieved a PCE of 13.19% under front illumination. This value further enhanced to 14.96% by integrating a reflecting mirror on the cell's backside to harness the albedo effect.

5.2 Tandem DSSC and thin film PV

In 2002, a model-based study[248] suggested optimal tandem cell bandgaps of 1.1 and 1.7 eV for bottom and top cells. Early work interpreted this by applying 1.04–1.67 eV bandgap CIGS thin film cells as bottom cells and N719-based DSSCs as top cells,

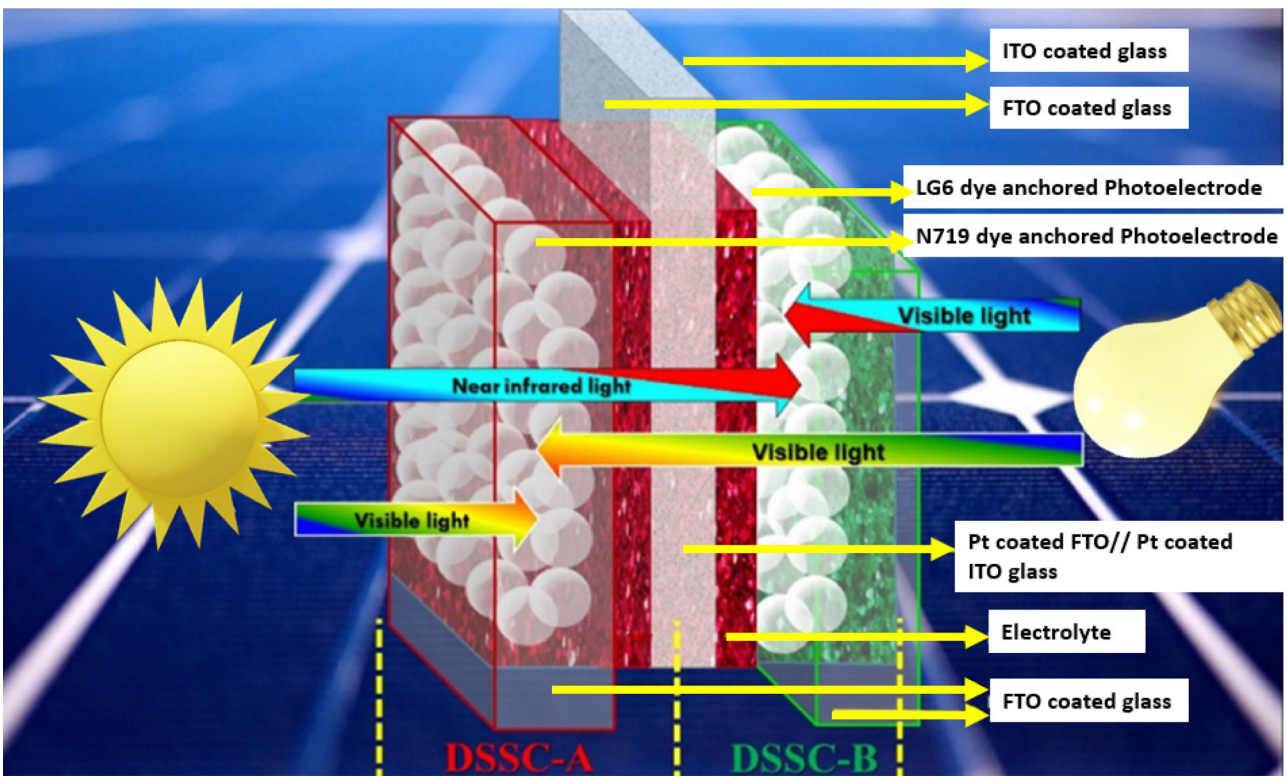

Fig. 15 Bifacial tandem DSSC–DSSC device structure modified from ref. 246.

with N719's HOMO–LUMO gap matching the model. Liska *et al.*[249] reached 15% efficiency and 1.45 V of V_{OC}, while Park *et al.*[250] later obtained similar V_{OC} but slightly lower efficiency. Both devices utilized ~12 μm TiO_2 in the top DSSC, resulting in a lack of transparency in the materials. A DSSC employing 4 μm TiO_2 film sensitized with light red Y123 dye was rendered semi-transparent by employing a cobalt electrolyte, offering enhanced transparency and reduced corrosivity compared to iodine-based electrolytes. PEDOT:PSS replaced platinum as a more transparent CE. This Y123-based DSSC combined with a CIGS bottom cell showed high stability over 1000 hours under ambient conditions.[251] Based on electrochemical impedance spectroscopy and photoelectrochemical cell measurement, the enhanced stability of the tandem cell is attributed to minimal corrosion by the cobalt-based polypyridine complex redox couple. In an early study,[252] stacked multijunction tandem solar cells were fabricated by mechanically assembling DSSCs as the top cell and a $GaAs/Al_XGa_{(1-X)}As$ graded solar cell (GGC) as the bottom cell. These cells were proposed for water-splitting applications, leveraging the remarkable open circuit voltage of 1.85. Three organic dyes, namely D131, D102, and D205, each with distinct absorption spectra, were employed in the DSSCs to ensure a balanced photocurrent density between the DSSC and the GGC. The open-circuit photovoltages for the GGC and the DSC with D131 were measured at 1.11 V and 0.76 V, respectively. This resulted in a combined V_{OC} of 1.85 V and a photovoltaic conversion efficiency of 7.63% for the tandem cell. Finally, successful solar-to-hydrogen conversion is achieved through the utilization of a T-DSSC/Si device.[253] An advanced DSSC/Si monolithic tandem cell is introduced, employing PEDOT:FTS as an interfacial catalytic layer. This layer, characterized by enhanced transparency and reduced charge-transfer resistance compared to traditional Pt as discussed before, plays a crucial role. Additionally, the precise adjustment of dye adsorption on TiO_2 nanoparticle surfaces ensures accurate current matching between the two sub-cells.

Through these strategic approaches, the DSSC/Si tandem cell demonstrates a significantly superior PCE of 18.1%, outperforming stand-alone SJ devices of DSSCs (≈11.4%) or Si (≈12.3%) cells. Moreover, the 2-T DSSC/Si solar cells exhibit a notable V_{OC} value of 1.36 V. These tandem solar cells, externally connected to a Pt electro-catalyst, serve as water splitting cells. Solar-to-hydrogen conversion is successfully achieved at 0.65 V *vs.* Pt bias.

This study[240] presents the successful fabrication of high-performance four-terminal solution-processed tandem solar cells, employing DSSCs as top-cells and lead sulfide (PbS) colloidal quantum dot solar cells (CQDSCs) as bottom-cells. To optimize light transmission, the TiO_2 scattering layer in the DSSCs was eliminated. Additionally, the impact of quantum dot size on PbS bottom-cell performance was investigated. The combination of the XL dye mixture and 890 nm PbS QDs yielded a remarkable PCE of over 12%, demonstrating a significant advancement compared to individual DSSC or CQDSC sub-cells.

5.3 Tandem DSSC and perovskite solar cells

In regard to the latest PSC, several record efficiencies for perovskite/silicon tandem cells reflect the race to surpass the most commercially available silicon-based devices. The most recent PCE record for a T-PSC/Silicon tandem cell reached 33.9% in 2023.[16] Despite their exceptional light absorption capabilities in the visible spectrum (400–800 nm), perovskites like $MaPbI_3$ and $FaPbI_3$ do not effectively capture NIR radiation, which contributes to about 45% of the sun's energy up to 1700 nm. By mixing lead with tin, researchers were able to move the perovskite photo-response until region spectrum where human cone are not sensitive, 1060 nm.[254,255] Unlucky, the mixed Pb/Sn compounds do not follow a linear trend in term of performance that resulted lower in comparison with remarkable results of reference perovskite. Recently, a tandem solar cell perovskite/DSSC has been proposed. A double cation perovskite ($(FAPbI_3)_{0.85}(MAPbBr_3)_{0.15}$), exhibiting a broad absorption spectrum in the visible range, was employed as the top sub-cell. Two dyes, thioindigo and N719, both absorbing in the visible range similar to perovskite, were tested in the bottom sub-cell of a DSSC. With both dyes, the photocurrent was constrained by the low current of the DSSC, resulting in a low PCE of 10.54% for the PSC/DSSC tandem device. However, a more effective approach would involve optimizing critical parameters such as the bandgaps of the absorbing materials. Considering that standard and efficient PSCs absorb within the visible range, a suitable compromise would be to employ a NIR-absorbing dye in the DSSC. Recently, a NIR-selective DSSC has been presented for the first time. The NIR-selective DSSC is colourless and transparent and impressive high AVT and CRI values of 76% and 92 have been demonstrated respectively.[18] Despite the modest PCE of 3.1%, which is not competitive with those present in the literature, the considerable high AVT and CRI values worth of investigation in terms of aesthetic and integration opportunities such as in tandem device and BIPV. The NIR selective sensitizer, VG20-Cx, is based on a cyanine structure and by molecular engineering, has been developed with its strong and sharp S0–S1 transition in the near-infrared region (λ = 832 nm) and a minimized S0–S*n* contribution in the far blue where the human retina is poorly sensitive. Opening rooms for the progress of efficient colourless NIR-DSSC request the design of specific transparent materials with tailored properties. Although a wide variety of NIR dyes have been synthesized for DSSCs to achieve selective NIR-DSSCs, the dye needs to exhibit almost zero absorption in the entire spectral region covered by human cones. Polymethine, phthalocyanines, and porphyrins[56] appear a promising class of dye due to the energetic levels that can ensure an efficient injection while having a bandgap sufficiently narrow to selectively absorb the NIR region.

6 Future prospects and concluding thoughts

Bifacial dye-sensitized solar cells (BFDSCs) have emerged as frontrunners in third-generation photovoltaic technologies. Their unparalleled adaptability, compared to traditional solar cells, pave the way for diverse applications, as highlighted in Sections 4.1–4.3. The purpose of this review was to consolidate all the information from the literature concerning the

characteristics of engineered materials, synthesized dyes, and different structures to enhance bifaciality and transparency. Several times, it has been emphasized how the catalyst plays a crucial role in ensuring the bifaciality of the BFDSC. Although expensive platinum remains one of the most efficient catalysts and, with optimized thickness, maintains good transparency, the PEDOT polymer emerges as an ideal competitor. The thickness of titania affects the cell's transparency, as does the choice of dyes. The application of NIR dyes will find future applications in tandem solar cells, thanks to the DSSC's ability to tune light absorption. However, the most notable feature of DSSC is the aesthetic appeal provided by its colors and semi-transparency. The second part of the review is dedicated to exploring adaptability in residential contexts, such as building façades. The challenge of applying DSSC in BIPV arises from the technology's current low efficiency. A viable application can be niche items like lamps or power sources for small devices or IoT. Furthermore, the integration of DSSCs into wearable electronics holds immense promise for the future of personal electronics. By harnessing the power of ambient light, DSSCs can provide a sustainable and renewable energy source for a wide range of wearable devices, from smartwatches and fitness trackers to smart clothing and healthcare monitoring systems.

In the realm of agrivoltaic, even though the same concern of low efficiency persists, making it challenging for massive energy production, DSSCs can serve as shading inside greenhouses for crops that aren't significantly affected by filtered light. This could help lower internal temperatures. Additionally, in these contexts, DSSCs could power IoT devices such as humidity and temperature sensors.

List of abbreviations

2T	Two terminals
4T	Four terminals
a-Si	Amorphous silicon
AVT	Average visible transmittance
BFDSCs	Bifacial DSSCs
BFF	Bifaciality factor
BFSCs	Bifacial solar cells
BIPV	Building-integrated photovoltaics
CB	Conduction band
CCT	Correlated color temperature
CdS	Cadmium selenide
CdTe	Cadmium telluride
CE	Counter electrode
CIGS	Copper indium gallium selenide
CQDs	Carbon quantum dots
CRI	Color rendering index
c-Si	Cristalline silicon
CV	Cyclic voltammetry
DSSCs	Dye-sensitized solar cells
DSSMs	Dye sensitized solar modules
EIS	Electrochemical impedance spectroscopy
FF	Fill factor
FoM	Figure of merit
FTO	Fluorine-doped tin oxide
GaAs	Gallium arsenide
GGC	GaAs/AlXGa (1×)As graded solar cell
GNTs	Graphene nanotubes
GuSCN	Guanidinium thiocyanate
HOMO	Highest occupied molecular orbital
IBEs	Iodine-based electrolytes
IoT	Internet of things
IPCE	Incident photon to current efficiency
ITO	Indium-doped tin oxide
J_{SC}	Short circuit current density
LUE	Light utilization efficiency
LUMO	Lowest unoccupied molecular orbital
MB	Methylbenzimidazole
MISCN	1-Ethyl-3-methylimidazolium thiocyanate
ML	Main layer
m-SC	Monofacial solar cell
M–Se	Metal selenide
N/S-GF	Nitrogen/sulphur dual-doped graphene film
N-GF	Nitrogen doped graphene films
OPV	Organic photovoltaics
PANI	Polyaniline
PCE	Power conversion efficiency
Pc-Si	Polycrystalline silicon
PE	Photoelectrode
PEDOT	Poly(3,4-ethylenedioxythiophene)
PET	Polyethylene terephthalate
PMII	1-Propyl-3-methyl-imidazolium iodide
PPy	Polypyrrole
PSC	Perovskite solar cells
Pt	Platinum
PV	Photovoltaic
PVDF	Polyvinylidene fluoride
QSSE	Quasi solid state electrolyte
R_{CT}	Charge transfer resistance
R_S	Series resistance
SC	Solar cell
S-CQDs	Sulphur-doped carbon quantum dots
SEM	Scanning electron microscope
S-GF	Sulphur doped graphene films
SL	Scattering layer
SSA	Specific surface area
TBP	4-*tert*-Butyl-pyridine
TCE	Transparent conductive electrode
TCO	Transparent conductive oxide
t-DSSC	Tandem DSSC
TED	Transparency, efficiency, diffused light efficiency
TEM	Transmission electron microscopy
VN	Valeronitrile
V_{OC}	Open circuit voltage
WE	Working electrode

Conflicts of interest

There are no conflicts to declare.

Acknowledgements

The authors gratefully acknowledge the project Best4U "Tecnologia per celle solari bifacciali ad alta Efficienza a 4 terminali per utility scale". European project financed by Italy's Ministry of Education (Ministero dell'Istruzione, dell'Università e della Ricerca, or MIUR) and the European Community through the European Regional Development Fund.

Notes and references

1 A. Bartolotta and G. Calogero, in *Solar Cells and Light Management: Materials, Strategies and Sustainability*, ed. F. Enrichi and G. C. Righini, Elsevier, Amsterdam, Netherlands, 2020, ch. 4, pp. 107–161, ISBN: 9780081027622.
2 N. Armaroli and V. Balzani, *Energia oggi e domani. Prospettive, sfide, speranze*, Bononia University Press, 2004.
3 Key world energy statistics 2021, International Energy Agency, **https://www.iea.org/reports/key-world-energy-statistics-2021**, (Last access 29/11/2023).
4 H. Ritchie, M. Roser and P. Rosado, Energy, Our World in Data, 2020 – **https://ourworldindata.org/energy**, (Last access 3/12/2023).
5 IEA, Renewables 2022, Analysis and forecast to 2027, OECD Publishing, Paris, International Energy Agency, **https://www.iea.org/reports/renewables-2022**, (Last access 29/11/2023).
6 K. Yoshikawa, H. Kawasaki, W. Yoshida, T. Irie, K. Konishi, K. Nakano, T. Uto, D. Adachi, M. Kanematsu, H. Uzu and K. Yamamoto, *Nat. Energy*, 2017, **2**, 17032.
7 M. A. Green, K. Emery, Y. Hishikawa, W. Warta, E. D. Dunlop, D. H. Levi and A. W. Y. H. Baillie, *Prog. Photovoltaics*, 2017, **25**, 3–13.
8 W. Shockley and H. J. Queisser, *J. Appl. Phys.*, 1961, **32**, 510–519.
9 H. Michaels, M. Rinderle, R. Freitag, I. Benesperi, T. Edvinsson, R. Socher, A. Gagliardi and M. Freitag, *Chem. Sci.*, 2020, **11**, 2895–2906.
10 P. Selvaraj, H. Baig, T. K. Mallick, J. Siviter, A. Montecucco, W. Li, M. Paul, T. Sweet, M. Gao, A. R. Knox and S. Sundaram, *Sol. Energy Mater. Sol. Cells*, 2018, **175**, 29–34.
11 W. Liu, L. Liu, C. Guan, F. Zhang, M. Li, H. Lv, P. Yao and J. Inghenoff, *Sol. Energy*, 2018, **162**, 84–94.
12 B. O'Regan and M. Grätzel, *Nature*, 1991, **353**, 737–740.
13 K. Kakiage, Y. Aoyama, T. Yano, K. Oya, J.-I. Fujisawa and M. Hanaya, *Chem. Commun.*, 2015, **51**, 15894–15897.
14 D. Zhang, M. Stojanovic, Y. Ren, Y. Cao, F. T. Eickemeyer, E. Socie, N. Vlachopoulos, J.-E. Moser, S. M. Zakeeruddin, A. Hagfeldt and M. Grätzel, *Nat. Commun.*, 2021, **12**, 1777.
15 W. Qarony, M. I. Hossain, M. K. Hossain, M. J. Uddin, A. Haque, A. R. Saad and Y. H. Tsang, *Results Phys.*, 2017, **7**, 4287–4293.
16 National Renewable Energy Laboratory (NREL) website: **https://www.nrel.gov/pv/assets/pdfs/best-research-cell-efficiencies.pdf**, (Last access 29/11/2023).
17 J. Barichello, L. Vesce, P. Mariani, E. Leonardi, R. Braglia, A. Di Carlo, A. Canini and A. Reale, *Energies*, 2021, **14**, 6393.
18 W. Naim, V. Novelli, I. Nikolinakos, N. Barbero, I. Dzeba, F. Grifoni, Y. Ren, T. Alnasser, A. Velardo, R. Borrelli, S. Haacke, S. M. Zakeeruddin, M. Graetzel, C. Barolo and F. Sauvage, *JACS Au*, 2021, **1**, 409–426.
19 M. D. Akhtaruzzamana, M. D. Shahiduzzamand, V. Selvanathana, K. Sopiana, M. I. Hossaine, N. Aminf and A. K. Mahmud Hasana, *Appl. Mater. Today*, 2021, **25**, 101204.
20 Y. H. Sim, M. J. Yun, S. I. Cha, S. H. Seo and D. Y. Lee, *ACS Omega*, 2018, **3**, 698–705.
21 J. M. Miranda-Munoz, S. Carretero-Palacios, A. Jiménez-Solano, Y. Li, G. Lozano and H. Mìguez, *J. Mater. Chem. A*, 2016, **4**, 1953–1961.
22 J. Chantana, Y. Kawano, T. Nishimura, A. Mavlonov and T. Minemoto, *Opt. Mater.*, 2021, **113**, 110819.
23 A. Kolay, P. Ghosal and M. Deepa, *ACS Sustainable Chem. Eng.*, 2020, **8**, 8593–8603.
24 M. Hiroshi, *US Pat.*, 3,278, 811, 1966.
25 A. Luque, A. Cuevas and J. M. Ruiz, *Sol. Cells*, 1980, **2**, 155–166.
26 A. Cuevas, A. Luque, J. Eguren and J. Del Alamo, *Sol. Energy*, 1982, **19**, 419–420.
27 R. Guerrero-Lemus, R. Vega, T. Kim, A. Kimm and L. E. Shephard, *Renewable Sustainable Energy Rev.*, 2016, **60**, 1533–1549.
28 R. Kopecek, 2nd Bifi PV Workshop, Chambery, France, 2014.
29 G. Romijn, 3rd Bifi PV Workshop, Miyazaki, Japan, 2016.
30 H. Fang, 4th Bifi PV Workshop, Denver, USA, 2018.
31 B. L. Smith, M. Woodhouse, K. A. W. Horowitz, T. J. Silverman, J. Zuboy and R. M. Margolis, National Renewable Energy Laboratory (NREL), NREL/TP-7A40-78173 2021, **https://www.nrel.gov/docs/fy22osti/78173.pdf**.
32 M. T. Patel, M. R. Khan, X. Sun and M. A. Alam, *Appl. Energy*, 2019, **247**, 467–479.
33 International Technology Roadmap for Photovoltaic-Results 2021 including maturity report 2022, Thirteenth edition, November 2022.
34 J. M. Gaby, G. J. Janssen, K. E. J. Tool, E. J. Kossen, B. B. Van Aken, A. J. Carr and I. G. Romijn, *Energy Procedia*, 2017, **124**, 76–83.
35 Q. Tai, B. Chen, F. Guo, X. Xu, H. Hu, B. Shebo and X.-Z. Zhao, *ACS Nano*, 2011, **5**, 3795.
36 Y. Duan, Q. Tang, J. Liu, B. He and L. Yu, *Angew. Chem.*, 2014, **53**, 14569–14574.
37 J. M. Miranda-Munoz, S. Carretero-Palacios, A. Jiménez-Solano, Y. Li, G. Lozano and H. Mıguez, *J. Mater. Chem. A*, 2016, **4**, 1953–1961.
38 S. Venkatesan, W.-H. Lin, H. Teng and Y.-L. Lee, *ACS Appl. Mater. Interfaces*, 2019, **11**, 42780–42789.
39 N. Roslan, M. E. Yàacob, M. A. M. Radzi, Y. Hashimoto, D. Jamaludin and G. Chen, *Renewable Sustainable Energy Rev.*, 2018, **92**, 171–186.
40 S. Pal, A. Reinders and R. Saive, *IEEE J. Photovolt.*, 2020, **10**(6), 1803–1815.

41 J. Balenzategui and F. Chenlo, *Sol. Energy Mater. Sol. Cells*, 2005, **86**(1), 53–83.
42 J. Barichello, D. Di Girolamo, E. Nonni, B. Paci, A. Generosi, M. Kim, A. Levtchenko, S. Cacovich, A. Di Carlo and F. Matteocci, *Sol. RRL*, 2023, **7**, 2200739.
43 L. Duan, D. Walter, N. Chang, J. Bullock, D. Kang, S. Pheng Phang, K. Weber, T. White, D. Macdonald, K. Catchpole and H. Shen, *Nat. Rev. Mater.*, 2023, **8**, 261–281.
44 I. Burgués-Ceballos, L. Lucera, P. Tiwana, K. Ocytko, L. W. Tan, S. Kowalski, J. Snow, A. Pron, H. Bürckstümmer, N. Blouin and G. Morse, *Joule*, 2021, **5**, 2261–2272.
45 J. J. Bezerra Galdino, O. de Castro Vilela, N. Fraidenraich and L. A. Gómez-Malagón, *Sol. Energy Mater. Sol. Cells*, 2023, **257**, 112359.
46 N. Gao, L. Huang, T. Li, J. Song, H. Hu, Y. Liu and S. Ramakrishna, *J. Appl. Polym. Sci.*, 2020, **137**, 48443.
47 D. Devadiga, M. Selvakumar, P. Shetty and M. S. Santhosh, *J. Electron. Mater.*, 2021, **50**, 6.
48 J. L. Gray, The Physics of the solar cell, in *Handbook of photovoltaic Science of Engineering*, ed. A. Luque and S. Hegedus, John Wiley & Sons Ltd, 2003.
49 G. Calogero, A. Bartolotta, G. Di Marco, A. Di Carlo and F. Bonaccorso, *Chem. Soc. Rev.*, 2015, **44**, 3244–3294.
50 K. Kalyasundaran and M. Grätzel, *Coord. Chem. Rev.*, 1998, **117**, 347–414.
51 M. Grätzel, *Prog. Photovoltaics*, 2006, **14**, 429–442.
52 M. K. Nazeeruddin, P. Pechy, P. Liska, T. Renouard, S. M. Zakeeruddin, R. Humphry-Baker, P. Comte, L. Cevey, E. Costa, V. Shklover, L. Spiccia, G. B. Deacon, C. A. Bignozzi and M. Grätzel, *J. Am. Chem. Soc.*, 2001, **123**, 1613–1624.
53 S. Ito, S. M. Zakeeruddin, P. Comte, P. Liska, D. Kuang and M. Gratzel, *Nat. Photonics*, 2008, **2**, 693–698.
54 W. Kubo, S. Kambe, S. Nakade, T. Kitamura, K. Hanabusa, Y. Wada and S. Yanagida, *J. Phys. Chem. B*, 2003, **107**, 4374–4381.
55 U. Würfel, J. Wagner and A. Hinsch, *J. Phys. Chem. B*, 2005, **109**, 20444–20448.
56 F. Grifoni, M. Bonomo, W. Naim, N. Barbero, T. Alnasser, I. Dzeba, M. Giordano, A. Tsaturyan, M. Urbani, T. Torres, C. Barolo and F. Sauvage, *Adv. Energy Mater.*, 2021, **11**, 2101598.
57 S. O. Abdellatif, S. Josten, A. S. G. Khalil, D. Erni and F. Marlow, *IEEE J. Photovoltaics*, 2020, **10**, 522–530.
58 W. Gu, T. Ma, S. Ahmed, Y. Zhang and J. Peng, *Energy Convers. Manage.*, 2020, **223**, 113283.
59 R. R. Lunt, *Appl. Phys. Lett.*, 2012, **101**, 043902.
60 Z. Hu, J. Wang, X. Ma, J. Gao, C. Xu, K. Yang, Z. Wang, J. Zhang and F. Zhang, *Nano Energy*, 2020, **78**, 105376.
61 P. Boyce, N. Eklund, S. Magnum, C. Saalfield and L. Tang, *Light. Res. Technol.*, 1995, **8**(2783), 145–152.
62 C. J. Traverse, R. Pandey, M. C. Barr and R. R. Lunt, *Nat. Energy*, 2017, **2**, 849–860.
63 M. R. Hunt and R. W. Pointer, *The Reproduction of Colour*, John Wiley & Sons Inc., Chichester, UK, 2011.
64 B. Commault, T. Duigou, V. Maneval, J. Gaume, F. Chabuel and E. Voroshazi, *Appl. Sci.*, 2021, **11**, 11598.
65 Jet Propulsion Laboratory, Ecostress Spectral Librabry, version 1.0, **https://speclib.jpl.nasa.gov/library**, (Last accessed 16th November 2023).
66 V. Carpenella, F. Ripanti, E. Stellino, C. Fasolato, A. Nucara, C. Petrillo, L. Malavasi and P. Postorin, *J. Phys. Chem. C*, 2023, **5**(127), 2440–2447.
67 M. P. Brennan, A. L. Abramase, R. W. Andrews and J. M. Pearce, *Sol. Energy Mater. Sol. Cells*, 2014, **124**, 111–116.
68 D.-K. Hwang, J. Eun Nam, H. Jeong Jo and S.-J. Sung, *J. Power Sources*, 2017, **361**, 87–95.
69 Q. Jiang, Z. Song, R. C. Bramante, P. F. Ndione, R. Tirawat, J. J. Berry, Y. Yan and K. Zhu., *Joule*, 2023, **7**(7), 1543–1555.
70 D. Ebner, M. Bauch and T. Dimopoulos, *Opt. Express*, 2017, **25**(8), A240–A252.
71 K. Kawajiri, K. Tahara and S. Uemiya, *Resour. Environ. Sustain.*, 2022, **7**, 100047.
72 Asia Nikkei, 2019, **https://asia.nikkei.com.**, (Last access 3/12/2023).
73 R. G. Gordon, *MRS Bull.*, 2000, **25**, 52–57.
74 F. Bonaccorso, *Int. J. Photoenergy*, 2010, 727134.
75 Z. Wu, Z. Chen, X. Du, J. M. Logan, J. Sippel, M. Nikolou, K. Kamaras, J. R. Reynolds, D. B. Tanner, A. F. Hebard and A. G. Rinzle, *Science*, 2004, **305**, 1273–1276.
76 S. Bae, H. Kim, Y. Lee, X. Xu, J.-S. Park, Y. Zheng, J. Balakrishnan, T. Lei, H. R. Kim, Y. I. Song, Y.-J. Kim,K., S. Kim, B. Özyilmaz, J.-H. Ahn, B. H. Hong and S. Iijima, *Nat. Nanotechnol.*, 2010, **4**, 574–578.
77 F. Bonaccorso, L. Colombo, G. Yu, M. Stoller, V. Tozzini, A. C. Ferrari, R. S. Ruoff and V. Pellegrini, *Science*, 2015, **347**, 1246501.
78 B. Ó. Regan and M. Grätzel, *Nature*, 1991, **353**, 737–740.
79 M. Dhonde, K. Sahu, M. Das, A. Yadav, P. Ghosh and V. V. S. Murty, *J. Electrochem. Soc.*, 2022, **169**, 066507.
80 S. Bellani, A. Bartolotta, A. Agresti, G. Calogero, G. Grancini, A. Di Carlo, E. Kymakis and F. Bonaccorso, *Chem. Soc. Rev.*, 2021, **50**, 11870–11965.
81 J. Wu, Z. Lan, J. Lin, M. Huang, Y. Huang, L. Fan, G. Luo, Y. Lin, Y. Xie and Y. Wei, *Chem. Soc. Rev.*, 2017, **46**, 5975.
82 Q. Tai and X.-Z. Zhao, *J. Mater. Chem.*, 2014, **2**, 13207–13218.
83 J. E. Trancik, S. C. Barton and J. Home, *Nano Lett.*, 2008, **8**, 982–987.
84 T. N. Murakami and M. Grätzel, *Inorg. Chim. Acta*, 2008, **361**, 572–580.
85 M. Vafaiee, M. Vossoughi, R. Mohammadpour and P. Sasanpour, *Sci. Rep.*, 2019, **9**, 2985.
86 S. Gullace, F. Nastasi, F. Puntoriero, S. Trusso and G. Calogero, *Appl. Surf. Sci.*, 2020, **506**, 144690.
87 Ç. Cetinkaya, E. Çokduygulular, B. Kınacı, F. Güzelçimen, Y. Özen, H. I. Efkere, I. Candan, S. Emik and S. Özçelik, *Sci. Rep.*, 2021, **11**, 13079.
88 H. Dong, Z. Wu, Y. Gao, A. El-Shafei, B. Jiao, Y. Dai and X. Hou, *Org. Electron.*, 2014, **15**, 1641–1649.
89 N. Mustaffa, M. Y. A. Rahman and A. A. Umar, *Ionics*, 2018, **24**, 3665–3671.
90 F. Navarro Pardo, D. Benetti, H. G. Zhao, V. M. Castaño, A. Vomiero and F. Rosei, *J. Power Sources*, 2016, **335**, 138–145.

91 U. A. Kamarulzaman, M. Y. A. Rahman, M. S. Su'ait and A. A. Umar, *Optik*, 2023, **276**, 170658.
92 R. G. Charles, P. Douglas, J. A. Baker, M. J. Carnie, J. O. Douglas, D. J. Penney and T. M. Watson, *J. Cleaner Prod.*, 2018, **202**, 1167–1178.
93 C. Zhao, Y. Shi, Z. Zhong and T. Ma, *Chin. J. Catal.*, 2014, **35**, 219–226.
94 S. Thomas, T. G. Deepak, G. S. Anjusree, T. A. Arun, S. V. Naira and A. S. Nair, *J. Mater. Chem.*, 2014, **2**, 4474–4490.
95 L. Y. Han, A. Islam, H. Chen, C. Malapaka, B. Chiranjeevi, S. F. Zhang, X. D. Yang and M. Yanagida, *Energy Environ. Sci.*, 2012, **5**, 6057.
96 I. K. Popoola, M. A. Gondal, J. M. AlGhamdi and T. F. Qahtan, *Sci. Rep.*, 2018, **8**, 12864.
97 I.-P. Liu, Y.-C. Hou, C.-W. Li and Y.-L. Lee, *J. Mater. Chem. A*, 2017, **5**, 240.
98 W. Hong, Y. Xu, G. Lu, C. Li and G. Shi, *Electrochem. Commun.*, 2008, **10**, 1555–1558.
99 Z. Yang, M. Liu, C. Zhang, W. W. Tjiu, T. Liu and H. Peng, *Angew. Chem., Int. Ed.*, 2013, **52**(14), 3996–3999.
100 Y. Jo, J. Y. Cheon, J. Yu, H. Y. Jeong, C.-H. Han, Y. Jun and S. H. Joo, *Chem. Commun.*, 2012, **48**, 8057–8059.
101 B. E. Hardin, H. J. Snaith and M. D. McGehee, *Nat. Photonics*, 2012, **6**, 162–169.
102 L. Kavan, Y. Saygili, F. Freitag, S. M. Zakeeruddin, A. Hagfeld and M. Grätzel, *Electrochim. Acta*, 2017, **227**, 194–202.
103 S. Mathew, A. Yella, P. Gao, R. H. Baker, B. F. E. Curchod, N. A. Astani, I. Tavernelli, U. Rothlisberger, M. K. Nazeeruddin and M. Grätzel, *Nat. Chem.*, 2014, **6**, 242–247.
104 C. Bu, Y. Liu, Z. Yu, S. You, N. Huang, L. Liang and X.-Z. Zhao, *ACS Appl. Mater. Interfaces*, 2013, **5**, 7432–7438.
105 X. Xu, W. Yang, Y. Li, Z. Tu, S. Wu, X. Ma, F. Yang, L. Zhang, S. Chen, A. Wang, H. Liu and P. Richard, *Chem. Eng. J.*, 2015, **267**, 289–296.
106 W. Yang, X. Xu, Z. Tu, Z. Li, B. You, Y. Li, S. I. Raj, F. Yang, L. Zhang, S. Chen and A. Wang, *Electrochim. Acta*, 2015, **173**, 715–720.
107 D. Yu, E. Nagelli, F. Du and L. Dai, *J. Phys. Chem. Lett.*, 2010, **1**, 2165–2173.
108 D. S. Su, J. Zhang, B. Frank, A. Thomas, X. Wang, J. Paraknowitsch and R. Schlögl, *ChemSusChem*, 2010, **3**, 169–180.
109 J. Ou, B. Hu, S. He, W. Wang and Y. Han, *Sol. Energy*, 2020, **201**, 693–700.
110 J. Ou, J. Xiang, J. Liu and L. Sun, *ACS Appl. Mater. Interfaces*, 2019, **11**, 14862–14870.
111 Z. Hu, K. Xia, J. Zhang, Z. Hu and Y. Zhu, *Electrochim. Acta*, 2015, **170**, 39–47.
112 Y. Duan, Q. Tang, J. Liu, B. He and L. Yu, *Angew. Chem. Int. Ed.*, 2014, **53**, 14569–14574.
113 M. Du, X. Li, H. Pang and Q. Xu, *EnergyChem*, 2023, **5**(2), 100083.
114 J. Duan, Y. Zhao, B. He and Q. Tang, *Electrochim. Acta*, 2018, **278**, 204–209.
115 H. Jung, V. S. Sapner, A. Adhikari, B. R. Sathe and R. Patel, *Front. Chem.*, 2022, **10**, 881495.
116 Y. Zhang, Y. Zhao, J. Duan and Q. Tang, *Electrochim. Acta*, 2018, **261**, 588–595.
117 T. Zhang, J. Bai, P. Yang, F. Li, X. Jin, Q. Zhang and Q. Li, *Sol. Energy*, 2018, **161**, 159–162.
118 K. Xiong, G. Li, C. Jin and S. Jin, *Mater. Lett.*, 2016, **164**, 609–612.
119 T. Liu, Y. Zhao, J. Duan, B. He, J. Zheng and Q. Tang, *Sol. Energy*, 2018, **170**, 762–768.
120 J. Xia, Q. Wang, Q. Xu, R. Yu, L. Chen, J. Jiao, S. Fan and H. Wu, *Appl. Surf. Sci.*, 2020, **530**, 147238.
121 C. Feng, G. Zhao, Y. Li, H. Cheng and Z. S. Wang, *J. Power Sources*, 2019, **426**, 16–22.
122 W. L. Lu, R. Jiang, X. Yin and L. Y. Wang, *Nano Res.*, 2019, **12**, 159–163.
123 C. Y. Chang, K. S. Anuratha, Y.-H. Lin, Y. Xiao, P. Hasin and J.-Y. Linet, *Sol. Energy*, 2020, **206**, 163–170.
124 K. Saranya, M. Rameez and A. Subramania, *Eur. Polym. J.*, 2015, **66**, 207–227.
125 S. S. B. Gunasekera, I. R. Perera and S. S. Gunathilaka, *Solar Energy: Systems, Challenges, and Opportunities*, 2020, ed. H. Tyagi, P. R. Chakraborty, S. Powar and A. Kumar Agarwal, pp. 345–371.
126 Q. Li, J. Wu, Q. Tang, Z. Lan, P. Li, J. Lin and L. Fan, *Electrochem. Commun.*, 2008, **10**, 1299–1302.
127 J. Wu, Y. Li, Q. Tang, G. Yue, J. Lin, M. Huang and L. Meng, *Sci. Rep.*, 2014, **4**, 4028.
128 Z. Li, B. Ye, X. Hu, X. Ma, X. Zhang and Y. Deng, *Electrochem. Commun.*, 2009, **11**, 1768–1771.
129 R. S. Moraes, E. Saito, D. M. G. Leite, M. Massi and A. S. da Silva Sobrinho, *Appl. Surf. Sci.*, 2016, **364**, 229–234.
130 L. Groenendaal, F. Jonas, D. Freitag, H. Pielartzik and J. Reynolds, *Adv. Mater.*, 2000, **12**, 481–494.
131 S. Xu, Y. Luo, G. Liu, G. Qiao, W. Zhong, Z. Xiao, Y. Luo and H. Ou, *Electrochim. Acta*, 2015, **156**, 20–28.
132 T. Xu, D. Kong, H. Tang, X. Qin, X. Li, A. Gurung, K. Kou, L. Chen, Q. Qiao and W. Huang, *ACS Omega*, 2020, **5**, 8687–8696.
133 S. Kang, J. Kim, J.-Y. Kim, M. J. Lee, J. Kang, Y. J. Son, J. Jeong, S. H. Park, M. J. Ko and Y.-E. Sung, *ACS Appl. Mater. Interfaces*, 2018, **10**, 8611–8620.
134 S. Venkatesan, W.-H. Lin, T.-H. Hsu, H. Teng and Y.-L. Lee, *ACS Sustainable Chem. Eng.*, 2022, **10**, 2473–2483.
135 S. S. Jeon, C. Kim, J. Ko and S. S. Im, *J. Phys. Chem. C*, 2011, **115**(44), 22035–22039.
136 S. S. Jeon, C. Kim, J. Kob and S. S. Im, *J. Mater. Chem.*, 2011, **21**, 8146.
137 J. Wu, Q. Lin, L. Fan, Z. Lan, P. Li, J. Lin and S. Hao, *J. Power Source*, 2008, **181**, 172–176.
138 C. Bu, Q. Tai, Y. Liu, S. Guo and X. Zhao, *J. Power Sources*, 2013, **221**, 78–83.
139 D.-Y. Wang, Y. T. Jiang, C.-C. Chen., K.-C. Ho and H.-L. Chou, *Angew. Chem., Int. Ed.*, 2013, **52**, 6694–6698.
140 X. Yao, B. He, L. Cui, J. Ti, H. Chen, Y. Duan and Q. Tang, *Catal. Commun.*, 2022, **163**, 106403.
141 J. Li, X. Li, T. Wang, P. He, F. Li, W. Chen and E. Wang, *ACS Appl. Energy Mater.*, 2019, **2**, 5824–5834.

142 P. Gu, D. Yang, X. Zhu, H. Sun, P. Wangyang, J. Li and H. Tian, *AIP Adv.*, 2017, **7**, 105219.
143 F. I. Chowdhury, M. Buraidah, A. Arof, B.-E. Mellander and I. Noor, *Sol. Energy*, 2020, **196**, 379–388.
144 J. Barichello, S. Gullace, A. Cusimano, G. Di Marco, F. Matteocci and G. Calogero, *Appl. Sci.*, 2022, **12**, 3159.
145 H. K. Kim, *ACS Omega*, 2023, **8**, 6139–6163.
146 Y.-F. Chiang, C.-H. Tsai, P. Chen and T.-F. Guo, *Sol. Energy*, 2012, **86**, 1967–1972.
147 A. F. Nogueira, C. Longo and M.-A. De Paoli, *Coord. Chem. Rev.*, 2004, **248**, 1455–1468.
148 A. Hagfeldt, G. Boschloo, L. Sun, L. Kloo and H. Pettersson, *Chem. Rev.*, 2010, **110**(11), 6595–6663.
149 K. Yoo, N. C. D. Nath, H. C. Kang, S. Muthu and J.-J. Lee, *ECS J. Solid State Sci. Technol.*, 2021, **10**, 025007.
150 S. H. Kang, M. J. Jeong, Y. K. Eom, I. T. Choi, S. M. Kwon, Y. Yoo, J. Kim, J. Kwon, J. H. Park and H. K. Kim, *Adv. Energy Mater.*, 2017, **7**(7), 1602117.
151 S. Hattori, Y. Wada, S. Yanagida and S. J. Fukuzumi, *J. Am. Chem. Soc.*, 2005, **127**(26), 9648–9654.
152 G. P. Kini, S. J. Jeon and D. K. Moon, *Adv. Funct. Mater.*, 2021, **31**, 2007931.
153 Q. Liu, L. G. Gerling, F. Bernal-Texca, J. Toudert, T. Li, X. Zhan and J. Martorell, *Adv. Energy Mater.*, 2020, **10**, 1904196.
154 H. Nusbaumer, J.-E. Moser, S. M. Zakeeruddin, M. K. Nazeeruddin and M. Gratzel, *J. Phys. Chem. B*, 2001, **105**, 10461.
155 S. A. Sapp, C. M. Elliot, C. Contado, S. Caramori and C. A. Bignozzi, *J. Am. Chem. Soc.*, 2002, **124**, 11215–11222.
156 S. M. Feldt, E. A. Gibson, E. Gabrielsson, L. Sun, G. Boschloo and A. Hagfeldt, *J. Am. Chem. Soc.*, 2010, **132**(46), 16714–16724.
157 D. P. Hagberg, X. Jiang, E. Gabrielsson, M. Linder, T. Marinado, T. Brinck, A. Hagfeldt and L. Sun, *J. Mater. Chem.*, 2009, **19**, 7232.
158 A. Yella, H.-W. Lee, H. N. Tsao, C. Yi, A. K. Chandiran, M. K. Nazeeruddin, E. W.-G. Diau, C.-Y. Yeh, S. M. Zakeeruddin and M. Grätzel, *Science*, 2011, **334**(6056), 629–634.
159 A. Yella, C.-L. Mai, S. M. Zakeeruddin, S.-N. Chang, C.-H. Hsieh, C.-Y. Yeh and M. Grätzel, *Angew. Chem., Int. Ed.*, 2014, **53**, 2973–2977.
160 K. Kakiage, Y. Aoyama, T. Yano, K. Oya, T. Kyomen and M. Hanaya, *Chem. Commun.*, 2015, **51**, 6315–6317.
161 V. P. S. Perera and K. Tennakone, *Sol. Energy Mater. Sol. Cells*, 2003, **79**, 249–255.
162 K. Tennakone, G. R. R. A. Kumara, A. R. Kumarasinghe, K. G. U. Wijayantha and P. M. Sirimanne, *Semicond. Sci. Technol.*, 1995, **10**, 1689–1693.
163 G. R. R. A. Kumara, A. Konno, G. K. R. Senadeera, P. V. V. Jayaweera, D. B. R. A. De Silva and K. Tennakone, *Sol. Energy Mater. Sol. Cells*, 2001, **69**, 195–199.
164 J. Cong, D. Kinschel, Q. Daniel, M. Safdari, E. Gabrielsson, H. Chen, P. H. Svensson, L. Sun and L. Kloo, *J. Mater. Chem. A*, 2016, **4**(38), 14550–14554.
165 S. C. Pradhan, A. Hagfeldt and S. Soman, *J. Mater. Chem. A*, 2018, **6**(44), 22204–22214.
166 Y. Cao, Y. Liu, S. M. Zakeeruddin, A. Hagfeldt and M. Grätzel, *Joule*, 2018, **2**(6), 1108–1117.
167 Y. Ren, N. Flores-Díaz, D. Zhang, Y. Cao, J. D. Decoppet, G. C. Fish, J. E. Moser, S. M. Zakeeruddin, P. Wang, A. Hagfeldt and M. Grätzel, *Adv. Funct. Mater.*, 2020, **30**(50), 2004804.
168 J. M. Ji, H. Zhou, Y. K. Eom, C. H. Kim and H. K. Kim, *Adv. Energy Mater.*, 2020, **10**(15), 2000124.
169 Y. Ren, D. Zhang, J. Suo, Y. Cao, F. T. Eickemeyer, N. Vlachopoulos, S. M. Zakeeruddin, A. Hagfeldt and M. Grätzel, *Nature*, 2023, **613**, 60.
170 A. B. Muñoz-García, I. Benesperi, G. Boschloo, J. J. Concepcion, J. H. Delcamp, E. A. Gibson, G. J. Meyer, M. Pavone, H. Pettersson, A. Hagfeldt and M. Freitag, *Chem. Soc. Rev.*, 2021, **50**, 12450.
171 J. Barichello, P. Mariani, F. Matteocci, L. Vesce, A. Reale, A. Di Carlo, M. Lanza, G. Di Marco, S. Polizzi and G. Calogero, *Nanomaterials*, 2022, **12**, 267.
172 C. Clavero, *Nat. Photonics*, 2014, **8**, 95–103.
173 G. Boschloo, *Front. Chem.*, 2014, **7**, 2296–2646.
174 A. Kay and M. Grätzel, *Chem. Mater.*, 2022, **14**, 2930–2935.
175 G. Kumara, K. Tennakone, V. P. S. Perera, A. Konno, S. Kaneko and M. Okuya, *J. Phys. D: Appl. Phys.*, 2001, **34**, 868–873.
176 Q. F. Zhang, C. S. Dandeneau, X. Y. Zhou and G. Z. Cao, *Adv. Mater.*, 2009, **21**, 4087–4108.
177 R. Tagliaferro, D. Colonna, T. M. Brown, A. Reale and A. Di Carlo, *Opt. Express*, 2013, **21**(3), 3235.
178 S. Hore, C. Vetter, R. Kern, H. Smitc and A. Hinsch, *Sol. Energy Mater. Sol. Cells*, 2006, **90**, 1176–1188.
179 S. Sasidharan, S. C. Pradhan, A. Jagadeesh, B. N. Nair, A. A. P. Mohamed, K. N. Narayanan Unni, S. Soman and U. N. S. Hareesh, *ACS Appl. Energy Mater.*, 2020, **3**, 12584–12595.
180 S. Venkatesan, Y.-S. Cho, I. P. Liu, H. Teng and Y.-L. Lee, *Adv. Opt. Mater.*, 2021, **9**, 2100936.
181 L. Zhang and J. M. Cole, *ACS Appl. Mater. Interfaces*, 2015, **7**, 3427–3455.
182 R. Y. Ogura, S. Nakane, M. Morooka, M. Orihashi, Y. Suzuki and K. Noda, *Appl. Phys. Lett.*, 2009, **94**, 073308.
183 Y. Hao, Y. Saygili, J. Y. Cong, A. Eriksson, W. X. Yang, J. B. Zhang, E. Polanski, K. Nonomura, S. M. Zakeeruddin, M. Grätzel, A. Hagfeldt and G. Boschloo, *ACS Appl. Mater. Interfaces*, 2016, **8**, 32797–32804.
184 L. Zhang and J. M. Cole, *J. Mater. Chem. A*, 2017, **5**, 19541–19559.
185 N. Shibayama, H. Ozawa, M. Abe, Y. Ooyama and H. Arakawa, *Chem. Commun.*, 2014, **50**, 6398–6401.
186 S. Armeli Minicante, E. Ambrosi, M. Back, J. Barichello, E. Cattaruzza, F. Gonella, E. Scantamburlo and E. Trave, *J. Phys. D: Appl. Phys.*, 2016, **49**, 295601.
187 G. Calogero, J. Barichello, I. Citro, P. Mariani, L. Vesce, A. Bartolotta, A. Di Carlo and G. Di Marco, *Dyes Pigm.*, 2018, **155**, 75–83.
188 X.-F. Wang, C. H. Zhan, T. Maoka, Y. Wada and Y. Koyama, *Chem. Phys. Lett.*, 2007, **447**, 79–85.
189 P. Sanjay, K. Deepa, J. Madhavan and S. Sentill, *Mater. Lett.*, 2018, **219**, 158–162.

190 C. Encinas, E. Otazo, L. Rivera, S. Miltsov and J. Alonso, *Tetrahedron Lett.*, 2002, **43**, 8391.
191 Z. Li, Z. Hui Jin, K. Kasatani and H. Okamoto, *Phys. B*, 2006, **382**, 229.
192 J. Park, N. Barbero, J. Yoon, E. Dell'Orto, S. Galliano, R. Borrelli, J.-H. Yum, D. Di Censo, M. Grätzel, M. K. Nazeeruddin, C. Barolo and G. Viscardi, *Phys. Chem. Chem. Phys.*, 2014, **16**, 24173.
193 M. Urbani, G. De La Torre, M. K. Nazeeruddin and T. Torres, *Chem. Soc. Rev.*, 2019, **48**, 2738.
194 C. C. Leznoff and A. B. P. Lever, *Phthalocyanines*, Wiley VCH, New York, 1997, pp. 1–4.
195 T. Ikeuchi, H. Nomoto, N. Masaki, M. J. Griffith, S. Mori and M. Kimura, *Chem. Commun.*, 2014, **50**, 1941.
196 Q. Huaulmé, V. M. Mwalukuku, D. Joly, J. Liotier, Y. Kervella, P. Maldivi, S. Narbey, F. Oswald, A. J. Riquelme, J. A. Anta and R. Demadrille, *Nat. Energy*, 2020, **5**, 468–477.
197 G. Berkovic, V. Krongauz and V. Weiss, *Chem. Rev.*, 2000, **100**, 1741–1754.
198 M. Irie, T. Fukaminato, K. Matsuda and S. Kobatake, *Chem. Rev.*, 2014, **114**, 12174–12277.
199 Y. Zhuge, D. Xu, C. Zheng and S. Pu, *Anal. Chim. Acta*, 2019, **1079**, 153–163.
200 R. A. Evans, T. L. Hanley, M. A. Skidmore, T. P. Davis, G. K. Such, L. H. Yee, G. E. Ball and D. A. Lewis, *Nat. Mater.*, 2005, **4**, 249–253.
201 D. Kim, K. Jeong, J. E. Kwon, H. Park, S. Lee, S. Kim and S. Y. Park, *Nat. Commun.*, 2019, **10**, 3089.
202 S. Fauvel, A. J. Riquelme, J. M. Andrés Castán, V. Mwatati Mwalukuku, Y. Kervella, V. Kumar Challuri, F. Sauvage, S. Narbey, P. Maldivi, C. Aumaître and R. Demadrille, *Chem. Sci.*, 2023, **14**, 8497.
203 International Energy Outlook 2023, **https://www.eia.gov/outlooks/ieo/** (Last access 3/12/2023).
204 Building Integrated Photovoltaic Market Size Report, 2030, **https://www.grandviewresearch.com/industry-analysis/building-integrated-photovoltaics-bipv-market**, (Last access 3/12/2023).
205 S. Barkaszi and J. Dunlop, *Sol. Energy*, 2001, 333–338.
206 H. M. Lee and J. H. Yoon, *Appl. Energy*, 2018, **225**, 1013.
207 T. Miyazaki, A. Akisawa and T. Kashiwagi, *Renewable Energy*, 2005, **30**, 281.
208 C. Hachem, A. Athienitis and P. Fazio, *Energy Procedia*, 2014, **57**, 1815.
209 A. Ghosh, S. Sundaram and T. K. Mallick, *Renewable Energy*, 2019, **131**, 730.
210 F. Martellotta, A. Cannavale and U. Ayr, *Energy Procedia*, 2017, **126**, 219.
211 S. Feroze, A. Distler, K. Forberich, I. Ahmed Channa, B. Doll, C. J. Brabec and H. J. Egelhaaf, *Sol. Energy*, 2023, **263**, 111894.
212 P. Mariani, L. Vesce and A. Di Carlo, *Semicond. Sci. Technol.*, 2015, **30**, 104003.
213 L. Vesce, A. Guidobaldi, P. Mariani and A. Di Carlo, in *Scaling-up of Dye Sensitized Solar Modules*, ed. M. L. Parisi and R. Basosi, World Scientific Reference of Hybrid Materials, 2019, ch. 3, vol. 2.
214 H. Kim, J. Jo, G. Lee, M. Shin and J. C. Lee, *Sol. Energy*, 2017, **155**, 585.
215 M. Godfroy, J. Liotier, V. M. Mwalukuku, D. Joly, Q. Huaulmé, L. Cabau, C. Aumaitre, Y. Kervella, S. Narbey, F. Oswald, E. Palomares, C. A. González Flores, G. Oskam and R. Demadrille, *Sustainable Energy Fuels*, 2021, **5**, 144.
216 D. Magistri, A. Lembo, V. Mirruzzo, G. Viscardi, P. Mariani, R. Manfredi, V. Liparoti, A. Lanuti, C. Bignozzi, T. M. Brown, L. Bonandini, E. Busatto, D. Colonna, A. Di Carlo, A. Giglielmotti, A. Guidobaldi, R. Boaretto, D. Prencipe, C. Barolo, R. Tagliaferro, S. Caramori, L. Vesce, G. Soscia, A. Smarra, R. Riccitelli and A. Reale, *HOPV15*, 2015.
217 M. L. Parisi, S. Maranghi, L. Vesce, A. Sinicropi, A. Di Carlo and R. Basosi, *Renewable Sustainable Energy Rev.*, 2020, **121**, 109703.
218 L. Vesce, P. Mariani, M. Calamante, A. Dessì, A. Mordini, L. Zani and A. Di Carlo, *Sol. RRL*, 2022, 2200403.
219 M. V. Khenkin, E. A. Katz, A. Abate, G. Bardizza, J. J. Berry, C. Brabec, F. Brunetti, V. Bulović, Q. Burlingame and A. Di Carlo, *et al.*, *Nat. Energy*, 2020, **5**, 35–49.
220 A. Roy, A. Ghosh, S. Bhandari, P. Selvaraj, S. Sundaram and T. K. Mallick, *J. Phys. Chem. C*, 2019, **123**, 23834–23837.
221 H. Dinesh and J. M. Pearce, *Renewable Sustainable Energy Rev.*, 2016, **54**, 299–308.
222 M. Kumar, D. Haillot and S. Gibout, *Sol. Energy*, 2022, **232**, 18–34.
223 T. Alinejad, M. Yaghoubi and A. Vadiee, *Renewable Energy*, 2020, **156**, 1–13.
224 R. U. Sánchez, Á. J. C. Ferre, J. P. Alonso and Á. C. Ortega, *Sci. Agric.*, 2012, **69**(4), 233–239.
225 A. Kavga, G. Trypanagnostopoulos, G. Zervoudakis and Y. Tripanagnostopoulos, *Not. Bot. Horti Agrobot. Cluj-Napoca*, 2018, **46**(1), 206–212.
226 C. Zisisa, E. M. Pechlivania, S. Tsimikli, E. Mekeridisb, A. Laskarakisa and S. Logothetidis, *Mater. Today: Proc*, 2019, **19**, 65–72.
227 J.-J. Kim, M. Kang, O. K. Kwak, Y.-J. Yoon, K. S. Min and M.-J. Chu, *Int. J. Photoenergy*, 2014, 1–7.
228 A. Dessì, M. Calamante, A. Sinicropi, M. L. Parisi, L. Vesce, P. Mariani, B. Taheri, M. Ciocca, A. Di Carlo, L. Zani, A. Mordini and G. Reginato, *Sustainable Energy Fuels*, 2020, **4**, 2309.
229 A. Dessì, D. A. Chalkias, S. Bilancia, A. Sinicropi, M. Calamante, A. Mordini, A. Karavioti, E. Stathatos, L. Zani and G. Reginato, *Sustainable Energy Fuels*, 2021, **5**, 1171.
230 D. A. Chalkias, C. Charalampopoulos, A. K. Andreopoulou, A. Karavioti and E. Stathatos, *J. Power Sources*, 2021, **496**, 229842.
231 C. J. M. Emmott, J. A. Röhr, M. Campoy-Quiles, T. Kirchartz, A. Urbina, N. Ekins-Daukes and J. Nelson, *Energy Environ. Sci.*, 2015, **8**, 1317.
232 A. Mourtzikou, D. Sygkridou, T. Georgakopoulos, G. Katsagounos and E. Stathatos, World Academy of Science, Engineering and Technology, *Int. J. Struct. Constr. Eng.*, 2020, **14**, 3.
233 N. Roslan, M. E. Ya'acob, D. Jamaludin, Y. Hashimoto, M. H. Othman, A. N. Iskandar, M. R. Ariffin, M. H. Ibrahim, J. Mailan and A. H. Jamaluddin, *Agronomy*, 2021, **11**, 631.

234 M. Freitag, J. Teuscher, Y. Saygili, X. Zhang, F. Giordano, P. Liska, J. Hua, S. M. Zakeeruddin, J.-E. Moser, M. Grätzel and A. Hagfeldt, *Nat. Photonics*, 2017, **11**, 372–378.
235 A. Aslam, U. Mehmood, M. H. Arshad, A. Ishfaq, J. Zaheer, A. Ul Haq Khan and M. Sufyan, *Sol. Energy*, 2020, **207**, 874–892.
236 M. Bradha, N. Balakrishnan, A. Suvitha, T. Arumanayagam, M. Rekha, P. Vivek, P. Ajay, V. Sangeetha and A. Steephen., *Environ. Dev. Sustain.*, 2022, **24**, 8807–8822.
237 RICOH, **https://industry.ricoh.com/en/dye-sensitized-solar-cell,** (Last access 3/12/2023).
238 EXEGER, **https://www.exeger.com/powerfoyle/applications**, (Last access 3/12/2023).
239 J. F. Geisz, R. M. France, K. L. Schulte, M. A. Steiner, A. G. Norman, H. L. Guthrey, M. R. Young, T. Song and T. Moriarty, *Nat. Energy*, 2020, **5**(4), 326–335.
240 L. Yuan, H. Michaels, R. Roy, M. Johansson, V. Öberg, A. Andruszkiewicz, X. Zhang, M. Freitag and E. M. J. Johansson, *ACS Appl. Energy Mater.*, 2020, **3**(4), 3157–3161.
241 Y. Z. Zheng, X. Tao, J. W. Zhang, X. S. Lai and N. Li, *J. Power Sources*, 2018, **376**, 26–32.
242 T. Yamaguchi, Y. Uchida, S. Agatsuma and H. Arakawa, *Sol. Energy Mater. Sol. Cells*, 2009, **93**, 733–736.
243 A. K. Baranwal, T. Shiki, Y. Ogomi, S. S. Pandey, T. Ma and S. Hayase, *RSC Adv.*, 2014, **4**, 47735.
244 Y. K. Eom, S. H. Kang, I. T. Choi, Y. Yoo, J. Kim and H. K. Kim, *J. Mater. Chem. A*, 2017, **5**, 2297.
245 S. Venkatesan, T.-H. Hsu, X.-W. Wong, H. Teng and Y.-L. Lee, *Chem. Eng.*, 2022, **446**(4), 137349.
246 P. Muni Mounika, M. Ambapuram, G. Maddala, S. Kalvapalli, M. K. Ganesha, A. K. Singh, N. Thota, M. Naga Rajesh, L. Giribabu, K. Venkateswarlu and R. Mitty, *ACS Appl. Electron. Mater.*, 2023, **5**, 5661–5667.
247 G. Gianola, R. Speranza, F. Bella and A. Lamberti, *Sol. Energy*, 2023, **265**, 112116.
248 T. J. Coutts, K. A. Emery and J. S. Ward, *Prog. Photovoltaics*, 2002, **10**, 195–203.
249 P. Liska, K. R. Thampi, M. Grätzel, D. Brémaud, D. Rudmann, H. M. Upadhyaya and A. N. Tiwari, *Appl. Phys. Lett.*, 2006, **88**, 203103.
250 W. S. Jeong, J. W. Lee, S. Jung, J. H. Yun and N.-G. Park, *Sol. Energy Mater. Sol. Cells*, 2011, **95**, 3419–3423.
251 S. Y. Chae, S. J. Park, O. S. Joo, Y. Jun, B. K. Min and Y. J. Hwang, *Sci. Rep.*, 2016, **6**, 30868.
252 S. Ito, I. M. Dharmadasa, G. J. Tolan, J. S. Roberts, G. Hill, H. Miura, J.-H. Yum, P. Pechy, P. Liska, P. Comte and M. Grätzel, *Sol. Energy*, 2011, **85**, 1220–1225.
253 J. Kwon, M. J. Im, C. U. Kim, S. H. Won, S. B. Kang, S. H. Kang, I. T. Choi, H. K. Kim, I. H. Kim, J. H. Park and K. J. Choi, *Energy Environ. Sci.*, 2016, **9**, 3794.
254 H. Feng, C. C. Stoumpos, R. P. H. Chang and M. G. Kanatzidis, *J. Am. Chem. Soc.*, 2014, **136**(22), 8094–8099.
255 R. K. Kothandaraman, Y. Jiang, T. Feurer, A. N. Tiwari and F. Fu, *Small Methods*, 2020, **4**, 2000395.